

Lukas Schweiger, BSc

**Ion dynamics in nanostructured $\text{Li}_{10}\text{GeP}_2\text{S}_{12}$
and $\text{Li}_{10}\text{GeP}_2\text{S}_{11.7}\text{O}_{0.3}$**

MASTER'S THESIS

to achieve the university degree of
Diplom-Ingenieur

Master's degree programme:
Advanced materials science

submitted to

Graz University of Technology

Supervisor

Univ.-Prof. Dr.rer.nat., Martin Wilkening
Institute for Chemistry and Technology of Materials

AFFIDAVIT

I declare that I have authored this thesis independently, that I have not used other than the declared sources/resources, and that I have explicitly indicated all material which has been quoted either literally or by content from the sources used. The text document uploaded to TUGRAZonline is identical to the present master's thesis.

Date, Signature

This master thesis was done in collaboration with
Thomas Lord Associate Professor of Materials Science and Engineering
Jennifer L. M. Rupp
Department of Materials Science and Engineering
Massachusetts Institute of Technology

Financial support for the making of this master thesis was granted by the

Austrian Marshall Plan Foundation
within the framework of the
Marshall Plan Scholarship Program

Acknowledgment

First, I would like to thank Professor Martin Wilkening for enabling this master thesis at the Institute of Chemistry and Technology of Materials. Professor Wilkening was very supportive for the whole duration of my work and his motivating words always spurred my ambition.

This master thesis was done in collaboration with Professor Jennifer Rupp from the Massachusetts Institute of Technology. I would like to pay my special regards to her for enabling this incredible opportunity. Although I was not able to finish my stay at MIT, the collaboration was maintained and both Professor Wilkening and Professor Rupp were very understanding and forthcoming in the organization of the continued cooperation.

Additionally, I would like to acknowledge the Austrian Marshall Plan Foundation for the financial support of my research stay at MIT.

I wish to show my gratitude to my colleagues from the institute who were all very helpful and supportive. I would particularly like to single out Katharina Hogrefe. The door of Katharina's office was always open whenever I ran into a trouble spot or had a question about my research or writing.

I must express my gratitude to my parents for enabling my studies and for the continued support and encouragement throughout my years of study. This accomplishment would not have been possible without them. Furthermore, I would also like to thank my brothers who have always been there for me.

I want to wholeheartedly appreciate the invaluable support and counsel of my dear girlfriend Sarah who had always open ears for my worries and problems.

In the end, I cannot forget to thank my friends for all the support and good times over the years of my studies.

Zusammenfassung

Ionenleitfähige Elektrolyte sind eine Schlüsselkomponente für zukünftige Festkörperbatterien und eines der zentralen Ziele der Materialforschung ist die Steigerung ihrer ionischen Leitfähigkeit. Einer der bisher besten Li^+ -Ionenleiter ist $\text{Li}_{10}\text{GeP}_2\text{S}_{12}$ mit einer herausragenden ionischen Leitfähigkeit von bis zu 12 mS cm^{-1} bei Raumtemperatur. In dieser Arbeit wurden $\text{Li}_{10}\text{GeP}_2\text{S}_{12}$ und die sauerstoffdotierte Variante $\text{Li}_{10}\text{GeP}_2\text{S}_{12-x}\text{O}_x$ ($x = 0.3$) synthetisiert, die Materialien strukturell charakterisiert und ihre Li-Ionendynamik untersucht. Während keine signifikanten Unterschiede in der Li^+ -Ionenleitfähigkeit von $\text{Li}_{10}\text{GeP}_2\text{S}_{12}$ und $\text{Li}_{10}\text{GeP}_2\text{S}_{11.7}\text{O}_{0.3}$ gefunden werden konnten, zeigte sich eine deutliche Änderung der Transporteigenschaften, wenn mikrokristallines $\text{Li}_{10}\text{GeP}_2\text{S}_{12}$ in einer Hochenergiekugelmühle in nanokristallines $\text{Li}_{10}\text{GeP}_2\text{S}_{12}$ umgewandelt wird. Wir beobachteten eine stetige Abnahme der Leitfähigkeit mit zunehmender Mahldauer. Rechnungen zur Ionendynamik in $\text{Li}_{10}\text{GeP}_2\text{S}_{12}$ von Dawson und Islam sagen voraus, dass mit einer deutlichen Verringerung der mittleren Kristallitgröße von $\text{Li}_{10}\text{GeP}_2\text{S}_{12}$ eine Erhöhung der Li^+ -Ionenleitfähigkeit zu erwarten sein soll. Im gegenwertigen Fall tritt jedoch eine Abnahme der Li^+ -Dynamik ein. Wir verfolgten die strukturellen und dynamischen Änderungen hinsichtlich des Kugelmahlens mittels Röntgendiffraktometrie, ^{31}P und ^6Li -MAS-NMR, Impedanzspektroskopie und ^7Li NMR Spin-Gitter-Relaxometrie. Die Bildung von amorphem $\text{Li}_{10}\text{GeP}_2\text{S}_{12}$ scheint für die verminderte Leitfähigkeit des nanostrukturierten Elektrolyten verantwortlich zu sein. Die sorgfältige Trennung von amorphen und kristallinen Leitfähigkeitsbeiträgen erlaubte uns die Untersuchung der Li^+ -Dynamik in den nanokristallinen Körnern, welche jedoch auch eine reduzierte Leitfähigkeit aufwiesen. Ein möglicher Grund könnte das Einbringen von Fehlstellen und Verzerrungen durch den Mahlprozess sein, die die Li^+ -Ionenwanderung behindern. NMR Spin-Gitter-Relaxometrie erlaubte die Untersuchung eines Sprungprozesses, der in kristallinem und amorphem $\text{Li}_{10}\text{GeP}_2\text{S}_{12}$ vorhanden ist und eine Aktivierungsenergie von $0.10(1) \text{ eV}$ in Ersterem, aber eine erhöhte Aktivierungsenergie von $0.14(1) \text{ eV}$ in Letzterem aufweist.

Abstract

Solid electrolytes are the key component for future all-solid-state batteries; maximizing their ionic conductivity is one of the main goals of materials research. $\text{Li}_{10}\text{GeP}_2\text{S}_{12}$ is one of the best Li-ion conductors so far with an ionic conductivity of 12 mS cm^{-1} at 298 K. Here, we synthesized micro- and nanocrystalline $\text{Li}_{10}\text{GeP}_2\text{S}_{12}$ as well as the oxygen-doped variant $\text{Li}_{10}\text{GeP}_2\text{S}_{12-x}\text{O}_x$ ($x = 0.3$), characterized the materials structurally and probed their Li-ion dynamic parameters. While no significant differences could be found between $\text{Li}_{10}\text{GeP}_2\text{S}_{12}$ and $\text{Li}_{10}\text{GeP}_2\text{S}_{11.7}\text{O}_{0.3}$, changes in ion conductivity of micro- and nanocrystalline $\text{Li}_{10}\text{GeP}_2\text{S}_{12}$ were probed by broadband impedance spectroscopy. Backed by predictions of a theoretical work by Dawson and Islam, we reduced the crystallite size of $\text{Li}_{10}\text{GeP}_2\text{S}_{12}$ by high-energy ball milling to further enhance Li-ion transport in $\text{Li}_{10}\text{GeP}_2\text{S}_{12}$. Despite the effort, the ionic conductivity turned out to decrease with increasing milling time. We followed both structural and dynamic changes introduced by ball milling by means of X-ray powder diffraction, ^{31}P and ^6Li MAS NMR, impedance spectroscopy and ^7Li NMR spin-lattice relaxation measurements. The formation of an amorphous phase seems to be responsible for the reduced performance of the nanostructured electrolyte. Careful separation of the amorphous and crystalline bulk contributions to the overall ionic conductivity allowed us to probe the dynamic response of the (nano)crystallites, which also revealed a lower conductivity than that of the non-treated microcrystalline counterpart. The introduction of defects and distortions impeding Li-ion migration seems to be a possible explanation for the decrease observed here. NMR spin-lattice relaxometry allowed us to probe a jump process that is seemingly present in both crystalline and amorphous $\text{Li}_{10}\text{GeP}_2\text{S}_{12}$ with an activation energy of $0.10(1) \text{ eV}$ in the former, but a higher activation energy of $0.14(1) \text{ eV}$ in the latter.

Contents

List of Symbols	9
Abbreviations	9
1 Introduction	10
1.1 Motivation	10
1.2 Solid-state batteries	11
1.2.1 Li-ion batteries – current state and limitations	11
1.2.2 All-solid-state batteries.....	12
1.2.3 Solid electrolytes	14
1.3 $\text{Li}_{10}\text{GeP}_2\text{S}_{12}$	16
1.3.1 Historically	16
1.3.2 Synthesis.....	18
1.3.3 Structure	23
1.3.4 Ionic conduction mechanism	28
1.4 Nanostructuring.....	32
1.5 Oxygen substitution and application in solid-state batteries	35
2 Methods	36
2.1 X-ray powder diffraction (XRD).....	36
2.2 Impedance and conductivity spectroscopy	41
2.3 Nuclear magnetic resonance (NMR) spectroscopy	48
2.3.1 Theory	48
2.3.2 ^7Li NMR Spin-lattice relaxation.....	50
2.3.3 Magic angle spinning (MAS) NMR	53
2.4 Raman spectroscopy.....	55
3 Experimental	56
3.1 Synthesis.....	56
3.2 X-ray powder diffraction.....	57
3.3 Impedance spectroscopy.....	58
3.4 Nuclear magnetic resonance.....	59
3.5 Raman.....	59
4.1 $\text{Li}_{10}\text{GeP}_2\text{S}_{12}$	60
4.1.1 Powder X-ray diffraction.....	60
4.1.2 MAS NMR	63
4.1.3 Ionic conductivity and ion dynamics.....	66
4.2 Oxygen substitution - $\text{Li}_{10}\text{GeP}_2\text{S}_{12-x}\text{O}_x$	77
4.3 Nanostructuring by ball milling.....	82
4.3.1 Structural characterization.....	82
4.3.2 Ionic conductivity and ion dynamics.....	87

6	Outlook.....	100
7	References.....	101
8	Appendix.....	107
8.1	Rietveld refinement.....	107
8.2	⁷ Li MAS NMR.....	108
8.3	Impedance and conductivity spectroscopy.....	108
8.4	⁷ Li NMR Spin-lattice relaxation.....	109

List of Symbols

Symbol	Physical quantity	Units
X – ray diffraction (XRD)		
2θ	scattering angle, incident beam \neq diffracted beam	$^\circ$
R_{wp}	weighted profile R-factor	unitless
R_{exp}	expected profile R-factor	unitless
χ^2 / GOF	goodness of fit	unitless
Impedance / conductivity spectroscopy (IS)		
ν	frequency	$\text{s}^{-1} = \text{Hz}$
σ (or σ')	conductivity (real part of the complex conductivity $\Re(\sigma^*)$)	S cm^{-1}
σ_{DC}	dc conductivity obtained from the plateau in conductivity spectra	S cm^{-1}
$\sigma_{20^\circ\text{C}}$	dc conductivity at 20 $^\circ\text{C}$ / room temperature	S cm^{-1}
M''	imaginary part of the electric modulus	arb. u.
E_a	activation energy	eV
E_a'	activation energy at elevated temperatures	eV
Z'	resistance, real part of the complex impedance $\Re(Z^*)$	Ω
Z''	reactance, imaginary part of the complex impedance $\Im(Z^*)$	Ω
R_i	resistance of resistor R_i in equivalent circuit	Ω
C_i	capacitance of constant phase element CPE_i in equivalent circuit	F
n_i	fractional exponent of constant phase element CPE_i , for ideal capacitor $n = 1$	unitless
C_s	capacitance directly calculated from the impedance data	F
$C_{b,gb}$	capacitance of the bulk or grain boundary contribution	F
$l_{b,gb}$	grain diameter, grain boundary thickness	$\text{m} = 10^{-10} \text{ \AA}$
D_σ	charge diffusion coefficient	$\text{m}^2 \text{ s}^{-1}$
Nuclear magnetic resonance (NMR)		
δ	chemical shift	ppm
T_1	spin-lattice relaxation time constant	s^{-1}
$T_{1\rho}$	spin-lock experiment, spin-lattice relaxation time constant	s^{-1}
τ_c	correlation time (equals residence time)	s
D_{uc}	uncorrelated diffusion coefficient	$\text{m}^2 \text{ s}^{-1}$

Abbreviations

Abbreviation	Meaning
arb. u.	arbitrary units
CPE	constant phase element (lumped circuit element)
fwhm	full width at half maximum
LGPS	$\text{Li}_{10}\text{GeP}_2\text{S}_{12}$
R	resistor (lumped circuit element)
rpm	rounds per minute

1 Introduction

1.1 Motivation

Li-ion batteries are regarded as one of the key technologies for many areas of today's life. Not only do they play an important role in most consumer electronics; their usage will become even more abundant with the continuing electrification of transportation and their introduction to large-scale grid storage. Consequently, Li-ion batteries also play an important role in the effort to reduce greenhouse gas emissions being responsible for climate change.

Therefore, improving Li-ion battery materials is a very important topic in current research activities. The focus over the last decade has been on the development of all-solid-state batteries, which should provide many advantages over conventional Li-ion batteries., like improved safety and possibly enhanced energy density.

One of the key features of the solid-state Li-ion battery technology is the solid electrolyte. Many different electrolyte materials are currently developed and investigated, there are however still significant technical and scientific challenges. Only few candidates are known, such as $\text{Li}_7\text{La}_3\text{Zr}_2\text{O}_{12}$ (LLZO) or $\text{Li}_{10}\text{GeP}_2\text{S}_{12}$ (LGPS), that seem very promising with regard to conductivity and electrochemical stability. In particular LGPS has a very high ionic conductivity, which would make it a perfect solid electrolyte, provided problems regarding chemical and electrochemical stability can be resolved.

Further improving the ionic conductivity will always be the goal of the field, and not only does enhanced conductivity directly benefit the application in batteries, but also by investigating and modifying the materials exciting new insights into the structure, chemistry, physics, and ion dynamics can be gained.

1.2 Solid-state batteries

1.2.1 Li-ion batteries – current state and limitations

Li-ion batteries can interconvert chemical and electrical energy via the reversible reactions at the electrodes, with the Li ions and electrons travelling over the internal electrolyte and the external circuit, respectively.¹ Traditionally, the anode is graphite and the cathode is a layered metal oxide such as LiCoO_2 or NMC ($\text{LiNi}_x\text{Mn}_y\text{Co}_z\text{O}_2$ with $x + y + z = 1$).¹ In between the electrodes a separator is placed that is impregnated with an organic, liquid electrolyte, see Figure 1.¹ Reaction between the electrodes and electrolyte leads to the formation of a so-called solid electrolyte interphase (SEI), an important factor since this layer passivates the electrodes and ensures the stability of the cell.^{2,3} Generally, the electrodes should have good electronic and ionic conductivity (i.e., be mixed conductors), while the electrolyte should have only good ionic conductivity and an electrical conductivity as low as possible.⁴

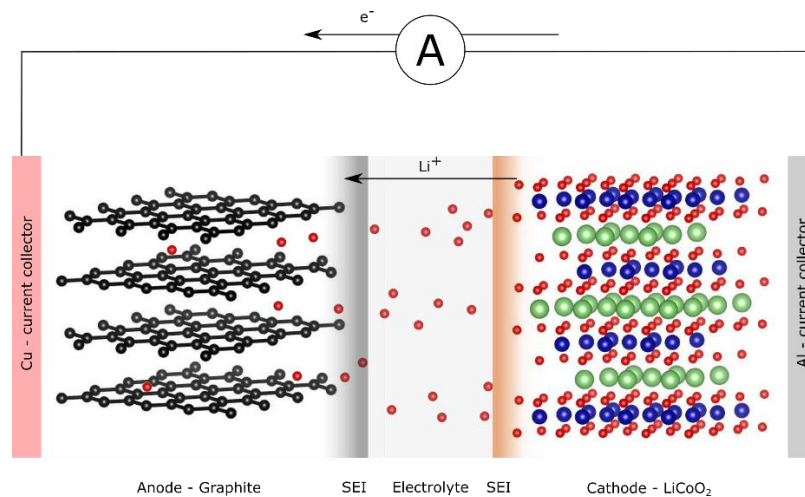


Figure 1: Illustration of the basic components and set-up of a conventional Li-ion cell. Inspired by Goodenough and Park⁵.

Li-ion batteries are the workhorses for energy storage in consumer electronics and provide good power and energy density, reliability and cyclability.^{5,6} Unfortunately, conventional Li-ion battery technology starts to approach its energy density limits.⁶ In essence there are three possibilities for improving the energy density of batteries: (1) maximizing the difference in chemical potential between the electrode materials, (2) using as lightweight materials as possible and (3) minimize degradation and consumption of electrolyte and electrode.⁷ Another disadvantage of the current technology is the use of organic electrolytes, which are flammable.² Under certain conditions an uncontrolled temperature increase can occur, called thermal runaway, which can, in combination with the combustible electrolyte, lead to catastrophic failure of the cell like fire and/or explosion.⁸ Although for many applications the problem of flammability has been overcome, there is an increased safety concern with regard to larger cells for electric vehicles or stationary grid storage.⁹ For batteries to become also competitive in transportation and large-scale grid storage new strategies will be necessary and new ways of improving performance are sought after.⁵

1.2.2 All-solid-state batteries

One concept to overcome these limitations is the replacement of the liquid, organic electrolyte employed nowadays with a solid electrolyte. This has the potential of not only increasing the energy density but also improving the safety of the system. Since such cells do not contain any liquid component anymore, the resulting battery is called an all-solid-state battery.⁶

The most apparent advantage of using a solid electrolyte is the improved safety since it completely avoids the flammable organic liquid electrolyte.¹⁰ The higher temperature stability of the solid electrolyte is even more beneficial because electrolytes show an enhanced conductivity at higher temperatures.⁶ The second major reason for using solid electrolytes is the possibility to improve the energy density. Only replacing the liquid electrolyte by a solid one will however not change the volumetric energy density and even downgrade gravimetric energy density, since solid electrolytes have a higher density than organic liquid ones.⁶ An increase in energy density is only achieved by using electrode materials that cannot be used with liquid electrolytes, like Li metal anodes or high-voltage cathode materials.⁶ Organic liquid electrolytes decompose at voltages above 5 V, preventing the use of high-voltage cathodes in conventional Li-ion batteries.⁵ Li metal anodes have a high reactivity toward the organic electrolyte, increasing the probability of thermal runaway during cycling¹¹ or the formation of dendrites due to non-uniform plating and stripping of Li-metal⁵. Both chemistries, the Li metal anode and the high-voltage cathode, might become a viable option when using a solid electrolyte, thereby increasing the energy density. Solid electrolytes allow for better power density too, i.e., higher current densities and faster charging, as no severe bulk polarization can occur.⁶ In liquid electrolytes both cations and (counter)anions are mobile, leading to bulk polarization during battery operation, while in solid electrolytes polarization effects are absent because there is only one mobile species, the Li-ion, in the otherwise immobile solid electrolyte lattice.⁶ Another benefit is that solid electrolytes allow for different cell architectures, allowing bipolar stacking⁸, miniaturization⁷ of cells, and generally a much simplified packaging, largely reducing dead weight¹⁰.

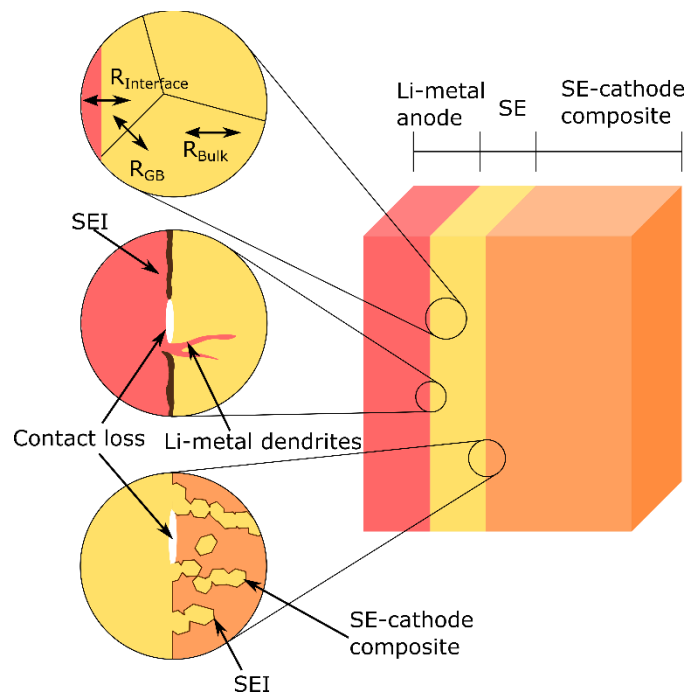


Figure 2: Illustration of an all-solid-state cell and the various elements responsible for internal resistance and defects. Inspired by Janek and Zeier⁶.

Although solid electrolytes and all-solid-state batteries hold the promise of being superior to conventional Li-ion batteries, there are still many problems that need to be overcome. The general structure and several problem areas of all-solid-state batteries are depicted in Figure 2.

The total resistance of the solid electrolyte should be as low as possible since the internal resistance of the electrolyte reduces the output voltage obtained during discharging and increases the voltage required for charging.⁵ This is due to the relation $\eta = I \cdot R_{\text{int}}$, with η being the polarization during discharging and overvoltage during charging, respectively.⁵ Fortunately, solid electrolytes with bulk conductivities rivaling that of current liquid electrolytes have already been demonstrated, examples are LLZO¹² and LGPS¹³. The most critical aspect of an all-solid-state battery is the interface of the electrolyte and the electrode. It is more difficult to achieve and maintain good physical contact between two solid materials which results in high internal resistance and diminished rate capabilities of all-solid-state batteries.^{14,15} The charging and discharging process is accompanied by a change in volume of the electrodes which can result in a loss of contact at the interface with cycling, increasing the internal resistance of the cell.^{5,6} Also, loss of contact can lead to an inhomogeneous current distribution at the anode and continued cycling might lead to the formation of dendrites, penetrating even the rigid solid electrolyte and possibly inducing an internal short-circuit.¹⁶

Most solid electrolytes are not thermodynamically stable against the Li metal anode or certain cathode chemistries.¹⁷ Therefore, similar to liquid electrolytes, also for solid electrolytes the formation of a stable and passivating SEI is required.^{6,17}

1.2.3 Solid electrolytes

For the realization of all-solid-state batteries the solid electrolyte is of central importance and great research effort is directed toward finding and improving potential candidates. There are certain general requirements which materials must have to be suitable for the application as a solid electrolyte in Li-ion batteries:¹⁸

- Ease of fabrication into a mechanically stable membrane enabling thin and large area electrolytes, thereby reducing the internal resistance R_{int} .
- Sufficiently high ionic conductivity $\sigma_{\text{int}} > 10^{-2} \text{ S cm}^{-1}$ at the operating temperature (equivalent to reducing R_{int}).
- A transport number close to unity. This requires the electronic conductivity to be as low as possible (minimization of losses) and the Li-ion to be the only mobile ionic species (minimization of polarization effect in the electrolyte).
- Low resistance for ion transfer across the electrode/electrolyte interface.
- Chemical and electrochemical stability either due to thermodynamic stability or by the formation of a passivating and Li⁺-permeable SEI.¹⁹
- The mobile ion of the electrolyte must be the working ion of the cell.
- Material and fabrication cost should be as low as possible. Used elements and corresponding raw materials should be abundant and easily available.
- Suitable mechanical properties with not too high (contact loss at interface and brittleness) and too low elastic modulus (cannot impede Li dendrite formation²⁰).²¹

Although all these criteria are important for solid electrolytes, the improvement of the ionic conductivity is the central theme for solid-state ionics. On the microscopic scale this means reduction of the bulk, grain boundary and interfacial resistance, see Figure 2. On the atomic scale the following structural criteria for ionic conductors must be fulfilled to achieve high (bulk) conductivities²²:

- Mobile ions (Li ions) of suitable size with a conduction pathway through the crystal structure. Suitable polyhedra connections.
- Disorder in the mobile (Li-)ion sublattice. Partial occupation of the sites of the sublattice.
- Highly polarizable mobile and immobile sublattices.

Currently, there are two major material groups that come into consideration for the use as solid electrolytes in batteries: inorganic solids and organic polymers.⁶ A combination of both is also possible.

Polymer electrolytes have good processibility and flexibility, while still maintaining the advantages of solid electrolytes, including dimensional stability, safety and the ability to prevent lithium dendrite formation.²³ A general disadvantage is the comparable low conductivity of polymer electrolytes, requiring them to be operated at elevated temperatures above 80 °C.⁶ One way to improve the properties of polymer electrolytes is by employing composite polymer electrolytes with highly conductive ceramic filler.²⁴

The second group are inorganic solids, including crystalline, glassy, and glass-ceramic materials. The two major materials in this group are oxides and sulfides. Advantages of such inorganic materials are their comparable high mechanical strength (although this can be strongly material dependent) and wide electrochemical window, which would allow the use of high-voltage cathodes.⁹ Also, as already mentioned, ionic conductivities are high compared to polymer electrolytes.⁶ Originally, the rigid nature and mechanical strength of many inorganic solids was believed to arrest Li dendrite growth completely, but dendritic growth is still reported for inorganic solid electrolytes.^{15,25}

Oxides are chemically relative stable against Li metal and have good ionic conductivity.⁶ An intrinsic disadvantage is the inherent brittleness of many oxides, which can lead to mechanical failure, cracking and contact loss.⁶ Examples are perovskites-type, NASICON-type, LISICON-type and garnet-type solid electrolytes.¹⁰ One of the most promising materials is the garnet-type $\text{Li}_7\text{La}_3\text{Zr}_2\text{O}_{12}$ (LLZO). If doping LLZO with Al^{3+} the cubic modification with two orders of magnitude higher Li-ion conductivity than the standard tetragonal modification can be obtained.¹² Ionic conductivities of up to 1 mS cm^{-1} at $25 \text{ }^\circ\text{C}$ have been achieved with this material.²⁶ Also, garnets show good stability against Li metal anodes and an electrochemical stability window of up to 6 V.¹² Much research effort is put into the synthesis of highly conductive LLZO thin films with various techniques.²⁶

Sulfides are also very promising for the use as solid electrolytes. They show very high conductivities, with $\text{Li}_{10}\text{GeP}_2\text{S}_{12}$ showing a conductivity $>10^{-2} \text{ S cm}^{-1}$.¹³ The high ionic conductivity is attributed to multiple factors:

- The ionic radius of sulfur ($r = 1.84 \text{ \AA}$) is larger than oxygen ($r = 1.38 \text{ \AA}$).²⁷ This would increase the space available for the Li ions in the conduction pathways.
- Sulfur is more polarizable than oxygen. With increasing polarizability, the interaction between the cationic (mobile) and anionic (immobile) sublattice becomes weaker, thereby increasing the Li-ion mobility.²⁸ This leads on average to a higher conductivity for sulfides and iodides compared to oxides and fluorides.²⁹

Sulfides do have a relatively low elastic modulus and are consequently mechanically soft.³⁰ Additionally, the grain-boundary resistance of sulfides is small compared to oxides.³¹ These features of sulfides should allow for sulfide solid electrolytes to be cold-pressed, skipping the expensive sintering step needed for most other, especially oxidic, materials.³² This is especially interesting considering that a recently reported life-cycle assessment of solid-state batteries, using LLZO as an electrolyte, indicated that electricity consumption due to high temperature production steps plays a significant role.³³ Furthermore, the low elastic modulus would allow a good electrolyte-electrode contact, even with changes in volume of the electrodes during charging and discharging.²¹

However, sulfides are not stable at ambient atmosphere and react with moisture under the formation of toxic H_2S gas.³⁴ Also, currently they cannot be applied as thin films since the needed deposition techniques for sulfides are missing.¹⁰ Another disadvantage of sulfide electrolyte is the high vapor pressure of sulfide species.³⁵

1.3 $\text{Li}_{10}\text{GeP}_2\text{S}_{12}$

1.3.1 Historically

The thiophosphate superionic conductor $\text{Li}_{10}\text{GeP}_2\text{S}_{12}$ (LGPS) with a room temperature ionic conductivity of 12 mS cm^{-1} was first reported by Kamaya et al. in 2011.¹³ The room temperature ionic conductivity even rivaled that of conventional organic, liquid electrolytes.¹³ Since then, LGPS has been intensively researched with an ever-increasing number of publications, see Figure 3.

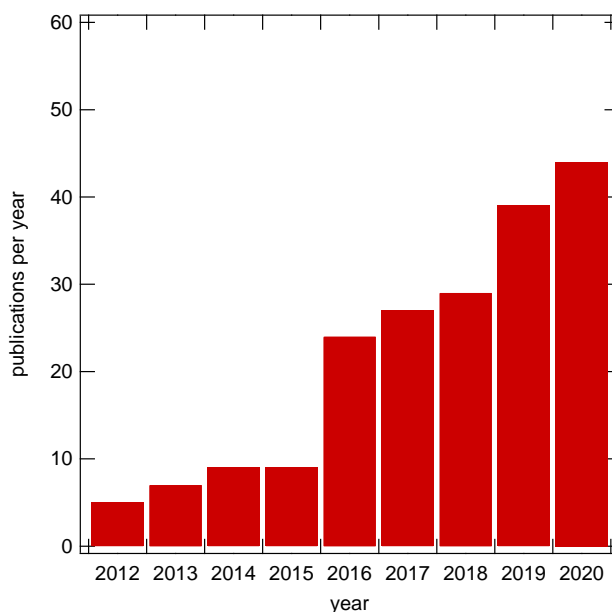


Figure 3: Publications per year according to webofknowledge.com (10.12.2020) with search for $\text{Li}_{10}\text{GeP}_2\text{S}_{12}$.

LGPS is a material originating from the thio-LISICON family of materials, which itself originated from the LISICON materials family, which are oxide Li-ion conductors. LISICON materials have a $\gamma\text{-Li}_3\text{PO}_4$ (related) crystal structure and prominent examples are solid solutions based on the phases $\gamma\text{-Li}_{2+2x}\text{Zn}_{1-x}\text{GeO}_4$ and $\gamma\text{-Li}_{3+x}(\text{P}_{1-x}\text{Si}_x)\text{O}_4$ in which, by aliovalent substitution, interstitial Li^+ is introduced, increasing the ionic conductivity.^{29,36}

These materials were the starting point when in 2000 Kanno et al. developed LISICON derived materials in which oxygen was replaced by sulfur, including materials like Li_4GeS_4 and $\text{Li}_2\text{ZnGeS}_4$. The development was carried by the assumption that substituting oxygen by the larger and more polarizable sulfur would increase the ionic conductivity of the electrolyte. Based on this notion, in the year 2000 Kanno et al. investigated the compositional space between $\text{Li}_2\text{S} - \text{GeS}_2$, $\text{Li}_2\text{S} - \text{GeS}_2 - \text{ZnS}$ and $\text{Li}_2\text{S} - \text{GeS}_2 - \text{Ga}_2\text{S}_3$ and discovered multiple new materials including Li_4GeS_4 , $\text{Li}_{4-2x}\text{Zn}_x\text{GeS}_4$ and $\text{Li}_{4+x+\delta}(\text{Ge}_{1-\delta-x})\text{Ga}_x\text{S}_4$. These phases showed promising ionic conductivities and had a structure similar to $\gamma\text{-Li}_3\text{PS}_4$ and consequently the novel material class was named thio-LISICON.³⁶

Similar to the oxidic LISICON materials, the enhanced ionic conductivity in the thio-LISICON materials can be attributed to the formation of solid solutions. As already mentioned in the above section, one design criterion for solid electrolytes is the introduction of disorder into the mobile Li-ion sublattice. One way of achieving this is aliovalent substitution (forming a solid solution), meaning the substitution of certain ions by ions of different charge. Due to the criterion of charge neutrality in ionic materials, this charge difference needs to be counterbalanced. This can happen by ionic or electronic means. Since for example materials like Li_4GeS_4 and Li_3PS_4 do not contain transition metals, which can change their oxidation state, an electronic balancing can be excluded. For instance, if Ge^{4+} is substituted by P^{5+} in the crystal structure, Li-vacancies V_i' with a net negative charge must be introduced.²²

Consequently, to further enhance the conductivity of sulfides and find new thio-LISICON materials, various sulfide solid electrolytes were combined, and the formed solid solutions investigated. Examples of thio-LISICON materials that were subsequently discovered are $\text{Li}_{4-x}\text{Si}_{1-x}\text{P}_x\text{S}_4$ ³⁷, $\text{Li}_{4-2x}\text{Zn}_x\text{Ge}_x\text{S}_4$ ³⁶, which can be regarded as vacancy doped systems, and $\text{Li}_{4+x}\text{Si}_{1-x}\text{Al}_x\text{S}_4$ ³⁷ and $\text{Li}_{4+x}\text{Ga}_{1-x}\text{Ge}_x\text{S}_4$,³⁶ which can be regarded as interstitial ion doped systems.³⁸

Two prominent sulfide compounds are Li_3PS_4 and Li_4GeS_4 . Both phases are structurally similar to $\gamma\text{-Li}_3\text{PO}_4$ and therefore sometimes attributed to the thio-LISICON family, but literature is inconsistent in this regard.^{22,36,39-41} Li_3PS_4 has a low temperature phase $\gamma\text{-Li}_3\text{PS}_4$ with a room temperature conductivity of $3 \times 10^{-7} \text{ S cm}^{-1}$, which converts at 195 °C to the high temperature phase $\beta\text{-Li}_3\text{PS}_4$ with an extrapolated room temperature conductivity of $9 \times 10^{-7} \text{ S cm}^{-1}$.⁴¹⁻⁴³ Although it is chemically the most stable sulfide compound against Li metal (contains no metal element), its poor ionic conductivity hinders application.^{41,42} Li_4GeS_4 has a $\gamma\text{-Li}_3\text{PO}_4$ structure and an ionic conductivity of $2.0 \times 10^{-7} \text{ S cm}^{-1}$ at 25 °C.³⁶

In the year 2000 Kanno and Murayama investigated the compositional space between Li_3PS_4 and Li_4GeS_4 , i.e., the solid solution $\text{Li}_{4-x}\text{Ge}_{1-x}\text{P}_x\text{S}_4$.²² The system $\text{Li}_{1-x}\text{Ge}_{1-x}\text{P}_x\text{S}_4$ showed a remarkably high ionic conductivity, even compared to the other thio-LISICON electrolytes, of $2.2 \times 10^{-3} \text{ S cm}^{-1}$.²² Interestingly, XRD analysis showed three regions of different superstructures were present, region I with $0 < x \leq 0.6$, region II with $0.6 < x \leq 0.8$ and region III with $0.8 < x \leq 1.0$.²² The conductivity was highest in region II. When comparing this with later published phase diagrams of the $\text{Li}_3\text{PS}_4\text{-Li}_4\text{GeS}_4$ system^{40,44}, region II roughly corresponds to the composition of the $\text{Li}_{10}\text{GeP}_2\text{S}_{12}$ phase. The synthesis was slightly different compared to the synthesis reported later for $\text{Li}_{10}\text{GeP}_2\text{S}_{12}$.²² During the following thorough investigation of the $\text{Li}_4\text{GeS}_4\text{-Li}_3\text{PS}_4$ phase diagram, the new crystalline superionic conductor $\text{Li}_{10}\text{GeP}_2\text{S}_{12}$ with its remarkably high ionic conductivity of 12 mS cm^{-1} was synthesized and reported in 2011.¹³

1.3.2 Synthesis

In 2011, Kanno et al. synthesized, characterized and reported the new phase $\text{Li}_{10}\text{GeP}_2\text{S}_{12}$ (LGPS) in the $\text{Li}_3\text{PS}_4\text{-Li}_4\text{GeS}_4$ system.¹³ LGPS was synthesized by means of a solid-state reaction. Stoichiometric quantities of Li_2S , GeS_2 and P_2S_5 were mixed and milled, the powder was followingly pressed into pellets, sealed in an evacuated quartz tube and heated at a temperature of $550\text{ }^\circ\text{C}$ for 8 h.¹³ Impedance measurements showed an extraordinary high ionic conductivity of 12 mS cm^{-1} .¹³ This broke the often cited important threshold of 10^{-2} S cm^{-1} required to compete with current organic, liquid electrolytes.¹⁸ The activation energy was calculated from the impedance results and was 24 kJ mol^{-1} (0.25 eV).¹³ Since then, many LGPS-related materials have been synthesized, different synthesis methods have been described and the structure and ionic dynamics of LGPS have been characterized with increasing precision. Synthesis methods include variations of the conventional solid-state synthesis route^{13,45,46}, methods for single crystal growth^{47,48} and (liquid phase) dissolution–precipitation routes⁴⁹.

Although other synthesis methods were reported in literature, the conventional solid-state reaction as described above is still the most common route and was also applied during this work. In a work by Tsukasaki et al. the mechanism of LGPS formation and crystallization was investigated by using in-situ TEM. After milling the obtained powder contained an amorphous LGPS precursor since in the XRD no new crystalline phase was observable (only reflexes of residual Li_2S starting material) and TEM electron diffraction also indicated an amorphous phase with no crystalline phase present. As the milled powder was annealed, crystallization occurred with $\beta\text{-Li}_3\text{PS}_4$ and Li_4GeS_4 forming in a temperature range of $260\text{ }^\circ\text{C}$ to $410\text{ }^\circ\text{C}$ and LGPS only forming at temperatures exceeding $450\text{ }^\circ\text{C}$. In DTA an exothermic peak at $508\text{ }^\circ\text{C}$ was attributed to the phase transition of Li_4GeS_4 and Li_3PS_4 to $\text{Li}_{10}\text{GeP}_2\text{S}_{12}$. This study also suggested that the grain growth following initial nucleation is sluggish. Simultaneously, as the material converted from the amorphous form to $\text{Li}_4\text{GeS}_4 / \text{Li}_3\text{PS}_4$ and then finally to LGPS, the ionic conductivity increased.⁵⁰

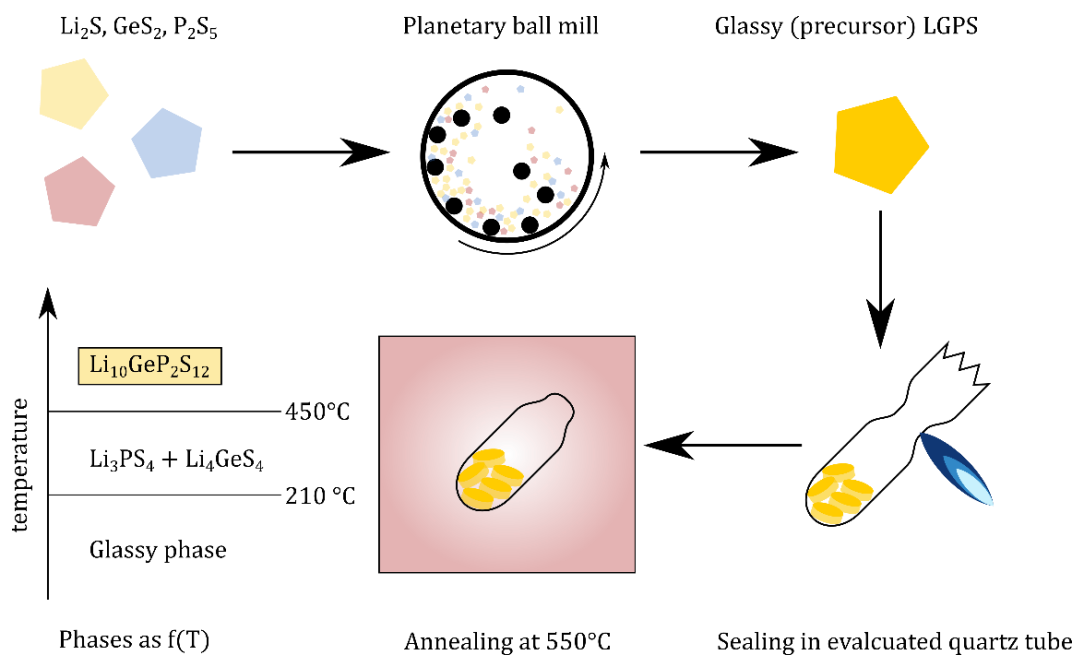


Figure 4: Illustration of the solid-state synthesis route. (bottom left) Phases presents as a function of temperature.

Theoretical work suggested that LGPS is thermodynamically not stable and decomposes to Li_4GeS_4 and Li_3PS_4 at 0 K.⁵¹ The possible importance of entropic effects was suggested due to the high mobility of the Li ions, which would of course be more pronounced at elevated temperatures.⁵¹ Later theoretical works considered such entropic effects and concluded that LGPS might be thermodynamically stable above 276 K.⁵² DTA results indicating the transformation of Li_4GeS_4 and Li_3PS_4 to LGPS at elevated temperatures ($>450^\circ\text{C}$) would indeed highlight the importance of entropic effects for the thermodynamic stability of LGPS.⁵⁰

As already mentioned, LGPS is a compound in the Li_3PS_4 - Li_4GeS_4 pseudo binary phase diagram. More detailed investigations into the Li_3PS_4 - Li_4GeS_4 system yielded the phase diagram depicted in Figure 5, revealing the compositional range in which LGPS is stable.⁴⁰ The phase diagram actually showed that there is some compositional tolerance for LGPS and that the exact composition $\text{Li}_{10}\text{GeP}_2\text{S}_{12}$ is at $x = 0.66$, the phosphorous rich border of the LGPS single-phase field:



Consequently, LGPS is a solid solution and different chemical composition are possible. For example, Ge-rich LGPS was synthesized by Kwon et al., having a chemical formula of $\text{Li}_{10+x}\text{Ge}_{1+x}\text{P}_{2-x}\text{S}_{12}$ and an ionic conductivity of 14.2 mS cm^{-1} for the sample with $x = 0.35$.⁵³

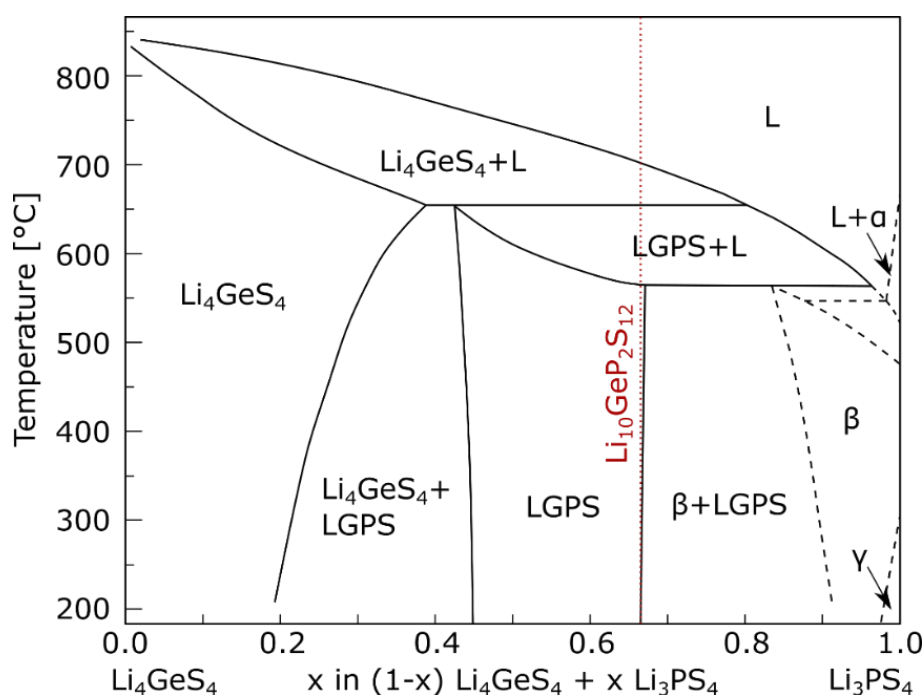


Figure 5: Phase diagram based on ref.⁴⁰, the red line indicates the composition $\text{Li}_{10}\text{GeP}_2\text{S}_{12}$.

Since the initial report about LGPS, many LGPS-related materials have been synthesized and different synthesis methods have been described for LGPS itself. Some of the reported materials, including the synthesis method and ionic conductivity obtained by impedance spectroscopy, are listed in Table 1. It should be noted that many different preparation techniques for the impedance measurements are reported in literature, including differences in pelletizing pressure and most notable if a heat treatment was applied to the pellet before impedance measurements or not. Sites in the LGPS crystal structure, cationic and anionic, can be occupied by various elements and there is a wide range of materials that were and can still be synthesized based on the LGPS structure.³⁸ Besides the strive for even higher ionic conductivity, two main goals of substitution are replacing the expensive Ge and the air and moisture sensitive S (formation of toxic H_2S).^{34,54}

Most of the LGPS-variants synthesized in literature are based on this possibility for substitution and the formation of solid solutions, see Figure 6. Some of the thio-LISICON solid solutions mentioned before, like $\text{Li}_{4-x}\text{Si}_{1-x}\text{P}_x\text{S}_4$ ³⁷, can also have crystal structures analogous to LGPS, like $\text{Li}_{11}\text{Si}_2\text{P}_2\text{S}_{12}$ ⁵⁵, and can therefore also be regarded as members of the LGPS family, although not containing any Ge.³⁸ Although such materials might have lower conductivity compared to LGPS, the substitution of Ge is an important step for reducing material cost, with one important example being $\text{Li}_{10}\text{SnP}_2\text{S}_{12}$.⁵⁶ Figure 6 illustrates the historical origin of LGPS and the relations between many of the subsequently reported LGPS-variants.³⁸

Theoretical calculations showed that cation (Si, Sn, P, Al) substitution should only have a minor influence on stability and performance, while anion (O, Se) substitution should have a much greater effect. These calculations also showed that sulfur seems to have an ideal size for the structural framework of LGPS. Oxygen reduced the performance drastically and selenium led to no significant change compared to sulfur. In the end, none of the substitutions yielded a significant increase in conductivity, indicating that LGPS could have reached already a critical threshold in terms of ionic conductivity.⁵⁴

Nonetheless, the potential for further improvement of the already high ionic conductivity by means of substitution was proven by the material $\text{Li}_{9.54}\text{Si}_{1.74}\text{P}_{1.44}\text{S}_{11.7}\text{Cl}_{0.3}$, reported to have a remarkably high ionic conductivity of 25 mS cm^{-1} , doubling the original conductivity of LGPS.⁵⁷ Still, many derivatives showed a similar conductivity to $\text{Li}_{10}\text{GeP}_2\text{S}_{12}$, see Table 1, indicating a threshold in the ionic conductivity of this structure class might have been reached. It is questionable if further groundbreaking enhancements in conductivity are possible.

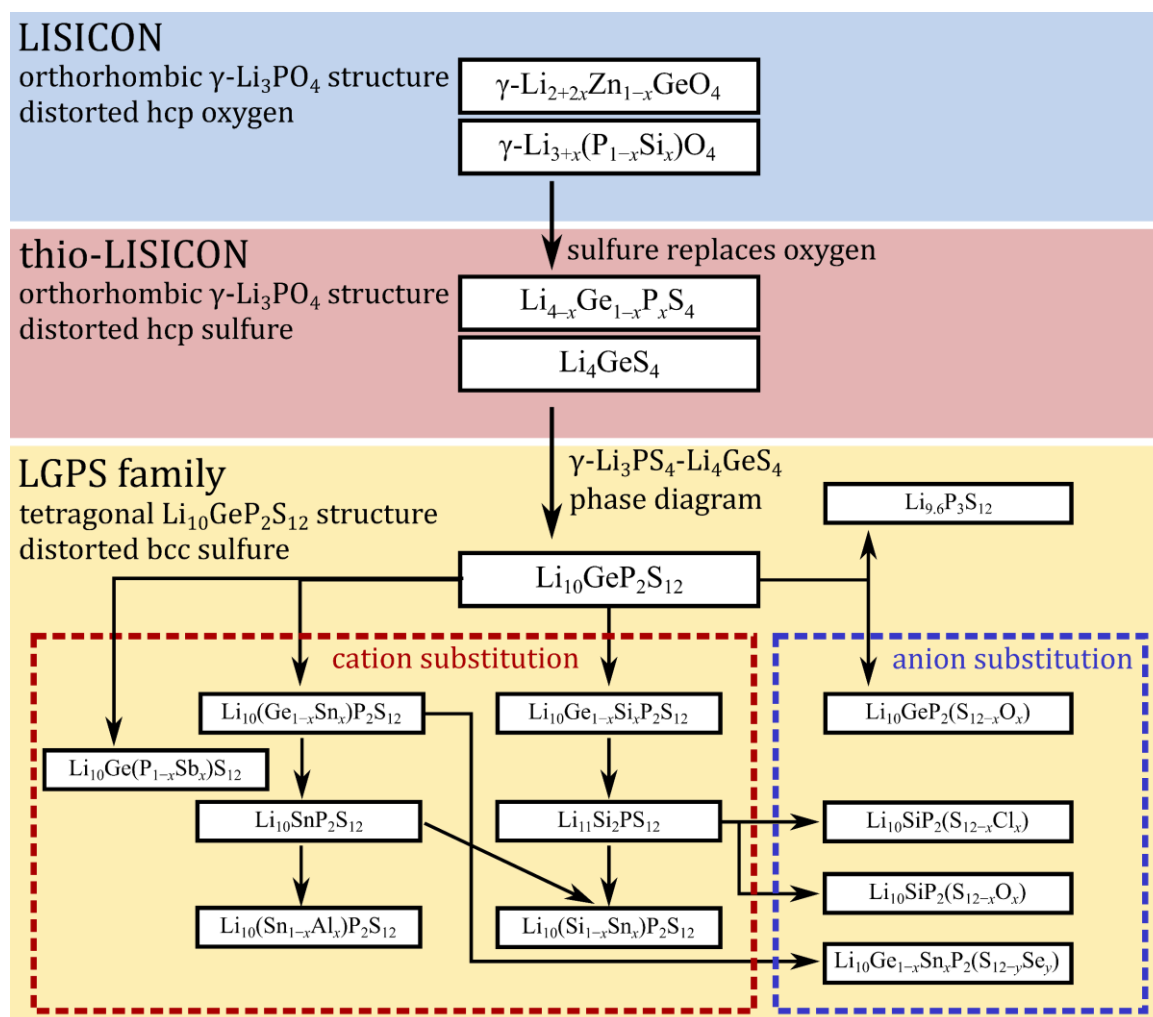


Figure 6: Historic origins of LGPS in the LISICON and thio-LISICON family and LGPS variants obtained by substituting either cations or anions. Inspired by Kato et al.³⁸.

A liquid-phase synthesis route was also reported in literature, see Table 1. However, this synthesis route is a dissolution-precipitation processes, using LGPS first synthesized by the conventional solid-state reaction as starting material.^{35,49} LGPS synthesized by the conventional solid-state route was partially dissolved in methanol, followed by drying and annealing.⁴⁹ LGPS showing an ionic conductivity of 1.7 mS cm^{-1} was obtained (no thin film).⁴⁹ The goal of such a dissolution-precipitation processes is to find a route for obtaining high quality thin films of LGPS, as many other competing solid electrolytes, for example LLZO, are readily used in thin film form. Deposition techniques normally applied for thin film production are not suited for sulfides.¹⁰ A suspension method in which the educts (Li_2S , GeS_2 and P_2S_5) themselves are dissolved and LGPS is directly precipitated is not reported in literature yet. Wang et al. reported that Li_2S and GeS_2 could be dissolved in anhydrous hydrazine, but P_2S_5 could not, probably due to its strong covalent bond character.⁵⁸ However, $\text{Li}_{4-x}\text{Ge}_{1-x}\text{P}_x\text{S}_4$ (thio-LISICON) synthesized by these educts could be completely dissolved at room temperature.⁵⁸

Table 1: LGPS and LGPS-variants including starting materials, synthesis procedure and ionic conductivity measured by impedance spectroscopy (measured at temperature T).

Composition	Starting materials	Preparation step / temperature / time	σ / mS cm ⁻¹ (T / K)
Li ₁₀ GeP ₂ S ₁₂ ¹³	Li ₂ S, P ₂ S ₅ , GeS ₂	Vibration milling, sealed in quartz tube, 550 °C for 8 h	12 (300)
Li ₁₀ GeP ₂ S ₁₂ ⁵⁹	Li ₂ S, P, Ge, S	Ball milling, sealed in quartz tube, 420 °C for 24 h	9 (298)
Li _{10.05} Ge _{1.05} P _{1.95} S ₁₂ ⁶⁰	Li ₂ S, P ₂ S ₅ , GeS ₂	Vibrating mill, tube furnace under argon flow, 550 °C for 8 h	6.85 (298)
Li ₁₀ GeP ₂ S ₁₂ ⁴⁹	Li ₂ S, P ₂ S ₅ , GeS ₂	Li ₁₀ GeP ₂ S ₁₂ synthesized by solid-state reaction, dissolved/dispersed in methanol, drying and subsequent annealing (550 °C for 8 h)	1.7 (298)
Li _{9.6} P ₃ S ₁₂ ⁵⁷	Li ₂ , P ₂ S ₅ , P	Ball milled, sealed in quartz tube, heated between 230 °C and 260 °C for 4 h	1.20 (298)
Li ₁₁ Si ₂ PS ₁₂ ⁵⁵	Li ₂ S, P, Si, S	Ball milling, sealed in quartz tube, 550 °C for 96 h, high-pressure treatment at 450 °C, 3 GPa < p < 5 GPa	4 (297)
Li ₁₀ SnP ₂ S ₁₂ ⁵⁶	Li ₂ S, P ₂ S ₅ , Li ₄ SnS ₄	Mixing and grounding with agate mortar, sealed in quartz tube, 600 °C for 48 h	4 (300)
Li _{9.54} Si _{1.74} P _{1.44} S _{11.7} Cl _{0.3} ⁵⁷	Li ₂ S, P ₂ S ₅ , GeS ₂ , SiS ₂ , LiCl	Ball milled, sealed in quartz tube, 475 °C for 8 h	25 (298)
Li ₁₀ GeP ₂ S _{12-x} O _x ⁴⁶	Li ₂ S, Li ₂ O, P ₂ S ₅ , GeS ₂	Ball milled, sealed in quartz tube, 550 °C for 24 h	10.3 for x = 0.3 (298) 8.43 for x = 0.6 (298)
Li ₁₀ SiP ₂ S _{12-x} O _x ⁶¹	Li ₂ S, P ₂ O ₅ , P ₂ S ₅ , SiO ₂ , SiS ₂	Ball milled, sealed in quartz tube, 550 °C for 48 h	3.1 for x = 0.7 (298)

1.3.3 Structure

While previous thio-LISICON materials were based on the already well-known crystal structure of γ - Li_3PO_4 , structural characterization of $\text{Li}_{10}\text{GeP}_2\text{S}_{12}$ revealed an entirely new structure type.^{13,38}

First reported by Kamaya et al. in 2011, the structure was evaluated by means of high-flux synchrotron XRD and powder neutron diffraction, yielding a tetragonal lattice with space group $P4_2/nmc$ (No. 137). The initially reported structural model contained two P sites, one shared in a 1:1 ratio by P and Ge (Wyckoff position: $4d$), and one solely occupied by P ($2b$). These sites were tetragonally coordinated by S. Additionally, three distinct Li sites were reported (Wyckoff positions: $16h$ (Li1), $4d$ (Li2), $8f$ (Li3)), each with an occupancy factor <1 . Two of the Li sites were tetragonally coordinated and one octahedrally. Three distinct sites were occupied by S.¹³

Consequently, this structural model was improved upon. Theoretical calculations indicated the presence of another Li site in the structure of LGPS.⁶² This site was then confirmed by neutron diffraction.⁴⁷

This structural model was confirmed by high quality single crystal diffraction data reported by Kuhn et al. in 2013. The basic structural model remained, but with the addition of the new Li site (Li4, Wyckoff position: $4c$). Lattice parameters were reported to be $c = 12.5830 \text{ \AA}$ and $a = 8.66402 \text{ \AA}$. The crystal structure based on this model is depicted in Figure 7, with the coordination polyhedra depicted for the P/Ge sites ($4d$, $2b$) and the octahedrally coordinated Li2 site ($4d$). This depiction was chosen since it is regularly used in literature and allows for an easier visualization of the crystal structure.⁴⁷

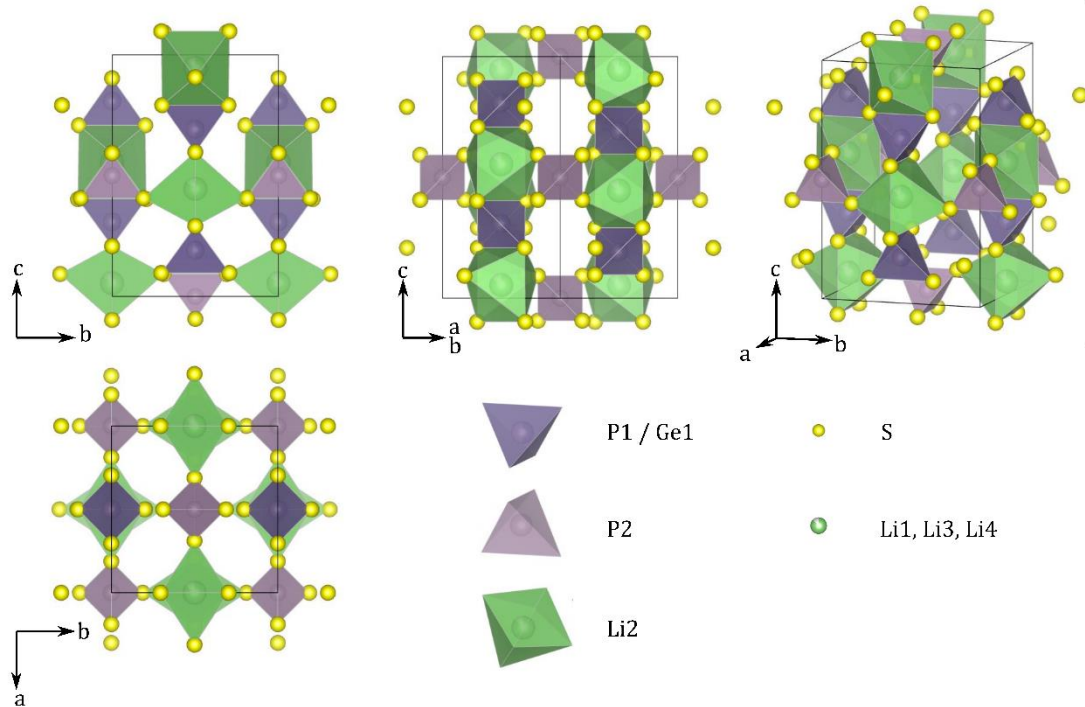


Figure 7: Common representation of the LGPS structure with $[(\text{P1,Ge1})\text{S}_4]$ - $[\text{Li2S}_6]$ chains in the $[001]$ (c) direction linked by $[\text{P2S}_4]$ units in the $[110]$ directions (ab plane). Based on crystallographic data reported by Kuhn et al.⁴⁷.

One way of explaining this new crystal structure in terms of the parental materials is by considering the tetrahedra arrangement in LGPS, γ - Li_3PS_4 , β - Li_3PS_4 and Li_4GeS_4 , all compounds that are present in the Li_3PS_4 - Li_4GeS_4 pseudo-binary phase diagram, see Figure 5. The compounds in the thio-LISICON family show different grades of ordering in the arrangement of the $[\text{PS}_4]^{3-}$ and $[\text{GeS}_4]^{4-}$ tetrahedral units. In γ - Li_3PS_4 the apices of the tetrahedra point all in the same crystallographic direction, while the degree of order is slightly lower in β - Li_3PS_4 and Li_4GeS_4 , in which the apices point in opposite directions, making a “zigzag” arrangement. Opposed to that, LGPS has very little ordering with regard to its tetrahedral units. A possible explanation could be that the tetrahedral arrangement is in a highly ordered state if all tetrahedral units have the same size. As Ge is introduced in γ - Li_3PS_4 , the highly ordered γ - Li_3PS_4 structure becomes increasingly distorted and unstable, transforming into β - Li_3PS_4 with a less ordered array of tetrahedra. Finally, if the content of Ge is increased further until a 1:1 ratio is obtained, the tetrahedra specifically rearrange in the LGPS structure.⁴⁰

The tetrahedral arrangements are illustrated in Figure 8, making the rather disordered tetrahedra arrangement of LGPS apparent. Consequently, it was suggested that introduction of disorder by different-sized tetrahedral building blocks might be essential for forming the LGPS structure.³⁸

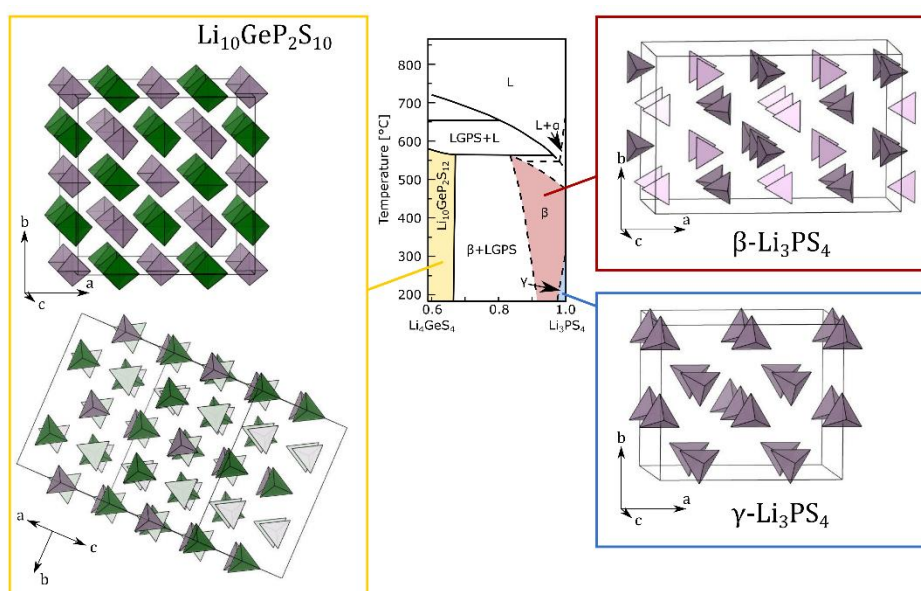


Figure 8: Illustration of the arrangement of the tetrahedral building blocks in the prominent thio-LISICON compounds γ - Li_3PS_4 and β - Li_3PS_4 and the new crystal structure of LGPS. Inspired by Hori et al..⁴⁰

The arrangement of the $[\text{PS}_4]^{3-}$ and $[(\text{P,Ge})\text{S}_4]^{3-}$ units is mostly well understood. However, some structural characteristics with regard to Li positions remain unresolved. For example, site splitting was reported for the Li2 site ($4d$ to $8f$)⁶³ and the Li3 site ($8f$ to $16h$)⁴⁸ and a conclusive structural model combining all these intricacies is missing in literature. Additionally, there is a certain spread of the occupancies of the Li sites as determined by diffraction studies.⁴⁸ For example, the values reported by Kwon et al.⁴⁵ set the occupancy of the Li2 site ($4d$) to 1, while Weber et al.⁶³ report a value of 0.54. While the former value indicated a relative minor contribution of the Li2 site to ionic transport, the later implied a higher degree of mobility. Nevertheless, the Li sites form multiple percolated migration pathways throughout the structure of LGPS and Figure 9 illustrates the various polyhedral chains according to the structural model of Kuhn et al..⁴⁷ The Li sites are situated in different chemical environments, with the Li1 and L3 site coordinated distorted tetrahedrally by sulfur, forming $[\text{LiS}_4]$ and $[\text{Li}_3\text{S}_4]$ units, and the Li2 and L4 sites being coordinated distorted octahedrally by sulfur, forming $[\text{Li}_2\text{S}_6]$ and $[\text{Li}_4\text{S}_6]$ units.

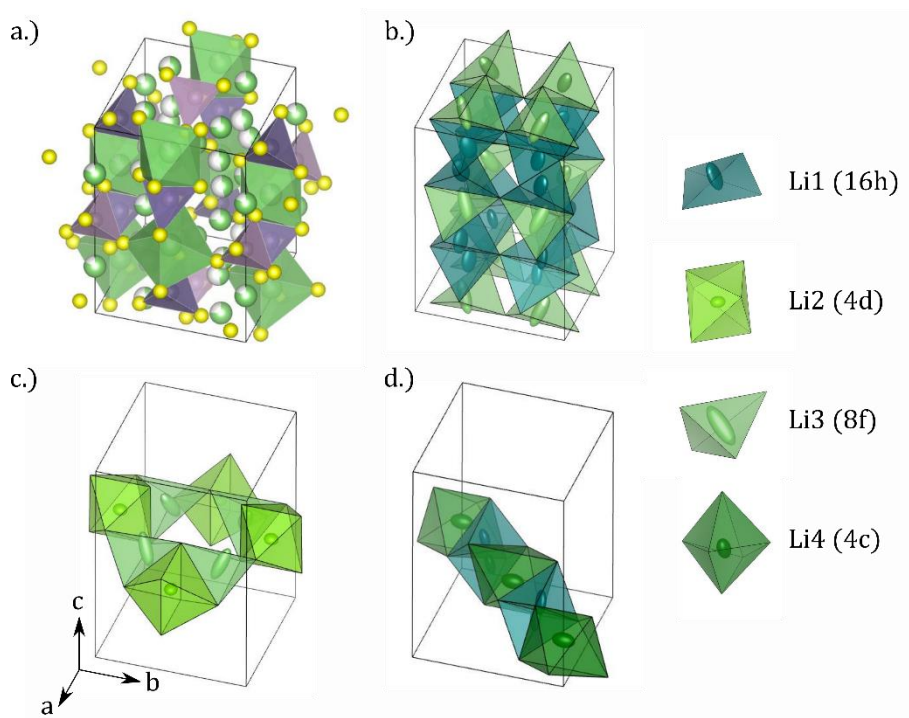


Figure 9: Li-sites and corresponding coordination polyhedra building up the transport pathways in the LGPS crystal structure. b.), c.) and d.) depict the Li-ion displacement ellipsoids. a.) The LGPS crystal structure as illustrated often in literature, b.) $[\text{Li1S}_4]\text{-}[\text{Li1S}_4]\text{-}[\text{Li3S}_4]$ chain in the (001) (c -)direction, c.) $[\text{Li2S}_6]\text{-}[\text{Li3S}_4]$ chain in the $\langle 110 \rangle$ direction (ab plane) and d.) $[\text{Li4S}_6]\text{-}[\text{Li1S}_4]\text{-}[\text{Li1S}_4]$ chain in the $\langle 110 \rangle$ direction (ab plane). Based on crystallographic data from Kuhn et al.⁴⁷. Inspired by Kato et al..³⁸

Some of these diffusion pathways might already be suspected from the crystal structure illustrated in Figure 7, namely the diffusion paths and channels along the $[100]$ and $[010]$ directions. All conduction pathways are illustrated in Figure 9 with a focus on the arrangement of the polyhedral units and in Figure 10 with a focus on the position and direction of the pathways in the overall crystal structure. Edge-sharing $[\text{Li1S}_4]$ and $[\text{Li3S}_4]$ distorted tetrahedral units constitute one-dimensional chains along the c direction, see Figure 9 b.). These channels are generally regarded as the most important Li-ion conduction pathways in LGPS. Evidence for the high mobility of the Li ions along this channel in c direction is the very large atomic displacement parameter of Li1 and Li3, including a strong anisotropic displacement in c direction, reported throughout literature.^{13,47,48} This indicated that the Li ions in this channel show strong thermal vibrations and are distributed relatively freely along the c direction, facilitating rapid Li-ion migration.³⁸

Li2 is located inside a distorted octahedron and is often depicted as part of the chain formed by it and the $[(\text{P1}/\text{Ge1})\text{S}_4]^{3-}$ units along the c direction. Additionally, together with the tetrahedrally coordinated Li3 sites it builds up edge-sharing chains along the $\langle 110 \rangle$ directions, that is the ab plane, see Figure 9 c.). It is currently not known if the Li2 site takes part in the conduction process. The occupancy parameter of the Li2 site during XRD and neutron diffraction measurements at different temperatures was reported to stay constant at 1, indicating that Li2 is part of the structural framework through which the mobile Li ions migrate.⁴⁵ However, as mentioned above, different values for the occupancy of the Li2 site were reported in literature. Another argument comes from NMR investigations with ^{31}P spin-lattice relaxometry studies in the rotation frame ($T_{1\rho}$) indicating atomic jumps between the Li4 and the Li1 sites, but excluding jumps between the Li2 and Li3 sites.⁶⁴ On the other hand, theoretical work indicated Li-ion migration over the Li2 site (some highlighted however the relative high activation barrier for Li2-Li3 jumps)^{51,52,62,65} and minimum entropy method analysis of neutron diffraction data resulted in negative nuclear density distribution maps implying diffusion along the $[\text{Li2S}_6]\text{-}[\text{Li3S}_4]$ chain⁶³.

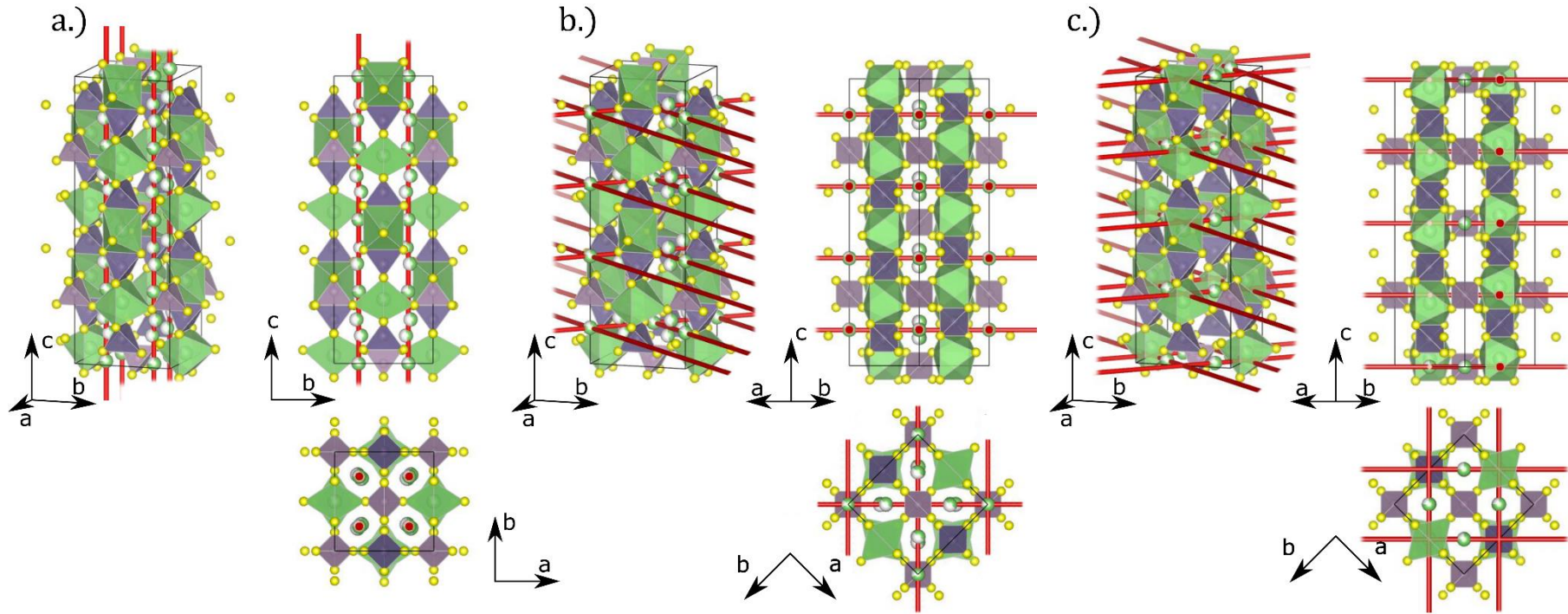


Figure 10: Conduction pathways along the $\langle 001 \rangle$ and $\langle 110 \rangle$ directions. Two-unit cells in the c direction are shown. a.) $[\text{Li}1\text{S}_4]\text{-}[\text{L}1\text{S}_4]\text{-}[\text{L}3\text{S}_4]$ conduction pathway along the $\langle 001 \rangle / c$ direction, b.) $[\text{Li}4\text{S}_6]\text{-}[\text{Li}1\text{S}_4]\text{-}[\text{L}1\text{S}_4]$ conduction path along the $\langle 110 \rangle$ directions/ ab plane, c.) $[\text{Li}2\text{S}_6]\text{-}[\text{L}3\text{S}_4]$ conduction path along the $\langle 110 \rangle$ directions/ ab plane.

Another channel associated with Li-ion transport is build up by the edge-sharing tetrahedral Li3, which is also part of the channel along the c direction, and the octahedral Li4 site, see Figure 9 d.). Such a channel would allow for Li-ion transport in the ab plane of the crystal structure. Atomic jump process along these sites were suggested by ^{31}P spin-lattice relaxometry data⁶⁴ and theoretical calculations^{51,62}.

In the end, although the structural model of LGPS has been continuously improved upon, the mentioned open questions about the Li sites and the Li-ion dynamics need to be addressed. The main difficulties are the weak X-ray scattering density of Li ions and the strong overlap of individual reflexes in the powder pattern. Both problems can be addresses by neutron powder diffraction on high-quality single crystals, which was however not reported in literature yet.³⁸

Another important factor for the extraordinary high ionic conductivity of LGPS is the arrangement of the anion, that is the sulfur, sublattice. LISICON materials have a γ - Li_3PO_4 or “ γ -tetrahedral structure” consisting of a distorted hexagonal close packed oxygen sublattice with the cations distributed over the tetrahedral and octahedral sites, forming a three dimensional conduction network.²⁹ Accordingly, the isostructural thio-LISICON materials like γ, β - Li_3PS_4 ⁴¹, Li_4GeS_4 ³⁹ and $\text{Li}_{4-x}\text{Ge}_{1-x}\text{P}_x\text{S}_4$ ²² all have a similar structure, comprised of a distorted hexagonal close packed sulfur sublattice.

Despite the structure of its parental phases, LGPS has a crystal structure with a bcc-like sulfur arrangement. Theoretical calculation of the activation energy for Li-ion jumps in hcp and bcc structures were performed, yielding that migration in bcc lattices takes place by jumps between tetrahedral sites with an activation energy of 0.15 eV. In the hcp lattice, these “tetrahedra-tetrahedra” jumps existed, but did not form a continuous conduction pathway throughout the structure. Consequently, “tetrahedra-octahedra-tetrahedra” jumps had to be performed for long-range migration, and these pathways were associated with activation energies of 0.40 eV. This difference in activation energy resulted in a difference in room temperature ionic conductivity of about three orders of magnitude. Consequently, one structural explanation for the high ionic conductivity of LGPS could be its underlying bcc sulfur sublattice, allowing a percolated network of tetrahedrally coordinated and energetically similar sites.⁶⁶

In the case of the specific structure of LGPS, this bcc-like arrangement can especially be found along the c direction, i.e., along the channel formed by the $[\text{Li}_1\text{S}_4]$ - $[\text{Li}_1\text{S}_4]$ - $[\text{Li}_3\text{S}_4]$ tetrahedral units often said to be responsible for rapid Li-ion migration.³⁸

1.3.4 Ionic conduction mechanism

Generally, the conduction mechanism of Li^+ in LGPS is anisotropic, with Li-ion migration happening readily along the Li1 and L3 sites in *c* direction, and comparably slow in the *ab* plane. As mentioned earlier, structurally, this was inferred from the large displacement parameter, including a strong anisotropic displacement along the *c* direction.^{13,47,48} Kanno et al. first stated that conduction along the *c* direction is the sole contributor to the high Li-ion conductivity observed.¹³ Although the assumption of rapid Li-ion migration in the channel along the *c* direction was backed by a theoretical work of Mo et al., molecular dynamics simulations showed also diffusion along two additional paths in the *ab* plane.⁵¹ The activation energies calculated for diffusion along the *c* direction and in the *ab* plane were 0.17 eV and 0.28 eV, respectively.⁵¹ Adams and Prasada Rao made similar calculations and obtained activation energies of 0.19 eV and 0.30 eV.⁶² Du et al. calculated activation barriers of 0.23 eV for Li1-Li3, 0.37 eV for Li1-Li4 and 0.56 eV for Li2-Li3.⁵² It should be noted that the first two works applied molecular dynamics and the latter the climbing image-nudged elastic band method.^{51,52,62}

Using ^7Li SAE NMR to probe the activation energy, Liang et al. were successful in obtaining activation energies of 0.16 eV and 0.26 eV, which were close to the calculated values by Mo et al.⁵¹ and therefore assigned to the *c* direction and *ab* plane migration, respectively. Additionally, ^7Li static dipolar line width measurements and T_1 as well as $T_{1\rho}$ spin-lattice relaxometry for both ^7Li and ^{31}P (probing both P sites independently by MAS conditions) yielded activation energies of 0.16, 0.18, 0.16 and 0.15 eV, all of which were attributed to jumps in the *c*-channel. Interestingly, when plotting the obtained jump rates in an Arrhenius fashion, an activation energy of 0.26 eV was obtained. This would be in line with the value expected for *ab* plane migration, was however attributed to the temperature dependence of the prefactor τ_∞ in $\tau = \tau_\infty \exp(E_a/k_bT)$, due to the change in vacancy concentration⁶² and distribution⁶⁷ as a function of temperature. Further analysis of the frequency dependency of the relaxation rates indicated 1D diffusion.⁶⁴

Another NMR study by Kuhn et al. obtained an Arrhenius plot using the jump rates and calculated an activation energy of 0.22 eV. Unlike Liang et al., this was interpreted as the migration process in the *ab* plane, since this value was close to the one obtained by PFG NMR (probing directly the self-diffusion coefficient).⁵⁹

External interpretation of these NMR results was also performed in a review by Kato et al., calculating the attempt frequencies of the supposed [001] (*c* direction) and [110] (*ab* plane) processes, obtaining 10^9 s^{-1} and 10^{12} - 10^{13} s^{-1} , respectively.^{38,59,64} The later value is in the range of the Debye frequency, as expected. The former value is very low, with a possible interpretation being that of soft-mode Li jumps in a shallow energy landscape being more liquid-like.³⁸ In the end however, although the characterization by NMR brought many insights, it is not completely conclusive yet and there are still many unresolved questions regarding the ion dynamics in LGPS.

As the activation energy for migration along the *c* direction was calculated to be much lower compared to *ab* plane diffusion^{51,52,62}, the remarkably high conductivity was often ascribed to this diffusion pathway, highlighting the anisotropic nature of the Li-ion migration process.¹³ This was also confirmed by impedance measurements on LGPS single crystals, yielding a conductivity of 28 mS cm^{-1} in the [001] direction, and 7 mS cm^{-1} in the [110] direction.⁴⁸ However, the difference in ionic conductivity between the [001] and the [110] direction was rather small when compared to the proposed large difference in activation energy.⁴⁸

The activation energy difference as calculated by Mo et al. would lead to a difference in conductivity at 300 K of two orders of magnitude according to $\sigma \sim \exp(-E_a/k_bT)$.⁵¹ Also the activation energies obtained from impedance measurements of single crystals were 0.4 eV and 0.3 eV for both the [001] and the [110] direction at low and high temperature, respectively.⁴⁸ Another study applied the PFG-NMR technique (probing directly the self-diffusion coefficient) and obtained an activation energy of 0.21 eV.⁵⁹ Both activation energies (0.21 eV⁵⁹ and 0.30 eV⁴⁸) are comparable high and are closer to the calculated value of ab plane Li-ion migration (0.28 eV⁵¹). Both impedance spectroscopy and PFG-NMR probe the macroscopic migration of Li ions. Consequently, a model was proposed by Iwasaki et al., stating that long-rang migration of Li ions in LGPS also necessitates leaving the channel in c direction, performing jumps in the ab plane.⁴⁸

This could be due to the unavoidable presence of defects, blocking the conduction path in c direction at some point in the crystal and provoking a side jump in order to pass.⁴⁸ If such conduction pathways are not present in the structure, no macroscopic ionic conduction would be possible.⁶⁸ The model proposed by Iwasaki et al. is illustrated in Figure 11.⁴⁸ Correspondingly, the high ionic conductivity of LGPS must be attributed to both c direction and ab plane migration processes working in tandem, and cannot be explained solely by mobile Li ions in the conduction pathways in c direction.³⁸

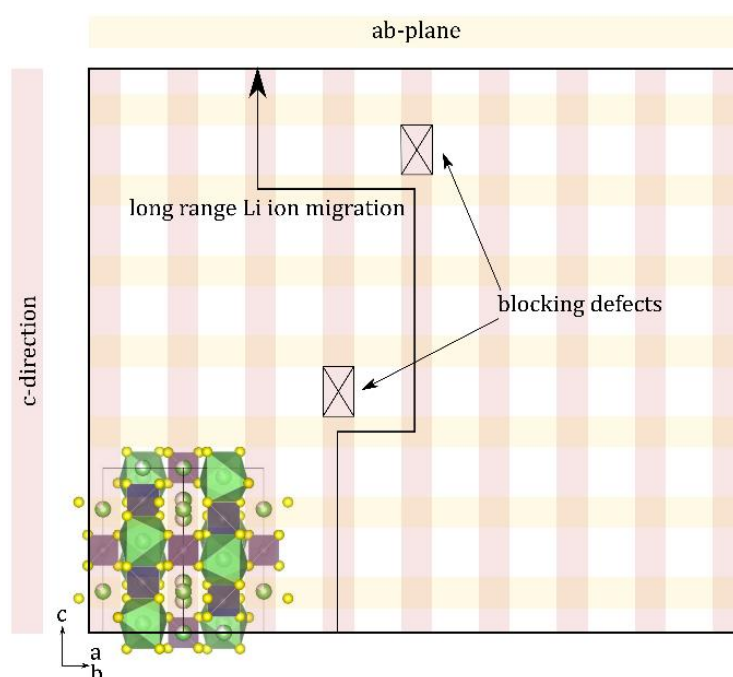


Figure 11: Model for long-range Li-ion migration as proposed by Iwasaki et al.. Figure is also inspired by Iwasaki et al..⁴⁸

Another phenomenon reported throughout literature is the change in activation energy at elevated temperatures. Although in the original paper by Kamaya et al. no change in slope in the Arrhenius plot was reported,¹³ later reexamination by Kato et al. indicated different activation energies at low and high temperatures.³⁸ Kwon et al. also found this behavior in $\text{Li}_{10+x}\text{Ge}_{1+x}\text{P}_{2-x}\text{S}_{12}$ and interpreted it as “diffuse phase transition”, a phenomenon often observed in materials with high ionic conductivity, but not yet understood completely.^{53,69} “Diffuse phase transitions” involve a substantial disordering of the mobile ion sublattice.⁶⁹ However, no DSC data of LGPS is available that could prove such preliminary explanations. No permanent change in activation energy was reported in literature, indicating that such a phase transition and/or change in Li-ion dynamics would be reversible.

On the other hand, investigations of Kuhn et al. allowed the separation of bulk and grain boundary contributions to the total ionic conductivity at lower temperatures, with an activation energy of 0.22 eV for the former and 0.30 eV for the later. At a temperature of about $-15\text{ }^{\circ}\text{C}$ the fit lines for the bulk and grain boundary contributions intersect, roughly at the same temperatures at which the activation energy (slope in the Arrhenius plot) changed. Therefore, the change in activation energy was interpreted as the grain boundaries becoming non-blocking at elevated temperatures.⁵⁹ This is contradicting the proposed mechanism of a “diffuse phase transition”.

Also, as mentioned previously, a recent paper performed impedance spectroscopy on LGPS single crystals. The ionic conductivity was probed in both the [001] and [110] direction. The Arrhenius plots for both crystallographic directions clearly showed a shift to lower activation energies at elevated temperatures ($-25\text{ }^{\circ}\text{C}$) from 0.40 eV to 0.30 eV. This suggested, since the measurements were made with high-quality single crystals, that the change in activation energy should not originate from the grain boundaries, but from the bulk.⁴⁸

The interpretation as blocking and non-blocking grain boundaries relied on a smaller activation energy of the bulk contribution to conduction. However, Bron et. al performed a detailed analysis of impedance data obtained from LGPS type materials and obtained an activation energy of about 0.30 eV for both the bulk and the grain boundaries.⁷⁰ It should be noted that generally the reported values for activation energies (mostly determined by impedance spectroscopy) spread considerable.

Additionally, theoretical calculations suggested a paddle-wheel mechanism could be active in $\text{Li}_{10}\text{GeP}_2\text{S}_{12}$.⁶² Such a mechanism is also often connected to an onset of rotational disorder in the solid and could also be a reason for the change in activation energy.⁷¹

Other possible explanations could simply be that a different step in the migration process becomes rate limiting.³⁸ Analysis of neutron diffraction data at different temperatures by Kwon et al. showed atomic distribution maps indicating one-dimensional diffusion pathways at low temperatures (100 K) and (quasi-)three-dimensional diffusion pathways at elevated temperatures (750 K).⁵³ Similar result were obtain by Weber et al. for room temperature neutron diffraction data.⁶³

In the end, no conclusive explanation can be given for the change in activation energy at elevated temperatures in LGPS. Table 2 lists literature data obtained from impedance measurements for LGPS and LGPS-related materials.

Table 2: Literature values for the conductivity and activation energies of LGPS and LGPS-variants. σ - ionic conductivity, E_a - activation energy. Yellow: Results from single crystal measurements. Blue: Results from first-principle calculations.

Reference	Material	Preparation	σ / mS cm ⁻¹ (T / K)	E_a / eV (T range / K)
Kamaya et al. ¹³	Li ₁₀ GeP ₂ S ₁₂	Pellet with $\varnothing=10$ mm, t=3-4 mm, Au electrodes, heated to 500 °C in vacuum	12.0 (300)	0.25 (163 – 383)
Kamaya et al. ¹³ as stated by Kato et al. ³⁸	-	-	-	0.31 (193 – 298)
				0.17 (322 – 673)
Hassoun et al. ⁷²	Li ₁₀ GeP ₂ S ₁₂	Pellet with $\varnothing=12$ mm, t=0.4-0.6 mm, Al electrodes	0.05 (294)	0.065 (298 – 383)
Kuhn et al. ⁵⁹	Li ₁₀ GeP ₂ S ₁₂	Annealed pellets with $\varnothing=12$ mm, t=1.5-3 mm), Au electrodes (sputtered)	9.0 (298)	0.30 (168 – 250, associated with g.b.) 0.22 (250 – 498, associated with bulk)
Kwon et al. ⁴⁵	Li _{10.35} Ge _{1.35} P _{1.65} S ₁₂	Pellet with $\varnothing=10$ mm, t=2-3 mm, 8 h @ 550 °C, Au electrodes	14.2 (300)	0.27 (193–373) 0.07 (573 – 673)
Sun et al. ⁴⁶	Li ₁₀ GeP ₂ S _{11.7} O _{0.3}	Pellet with $\varnothing=10$ mm, t=1-2 mm, sintered at 550 °C for 12h, Au electrodes	10.3 (298)	0.21 (298 – 398)
Bron et al. ⁷⁰	Li ₁₀ GeP ₂ S ₁₂	Pellet with $\varnothing=6$ mm, t=0.5 – 1.5 mm, pressed 45 min at 270 MPa, 24 h @ 500 °C, Au electrodes (sputtered), bulk	9 (298)	0.30 (133 – 213)
		Grain boundary	-	0.31 ((133 – 213)
Krauskopf et al. ⁷³	Li ₁₀ GeP ₂ S ₁₂	Pellet with $\varnothing=10$ mm, Au electrode (sputtered)	7.6 (298)	0.27 (233 – 333)
Dominik et al. ⁶³	Li ₁₀ GeP ₂ S ₁₂	Pellet with $\varnothing=10$ mm, Au electrodes (vapor deposition), sealed in pouch cell	5 (298)	0.35 (233-373)
Iwasaki et al. ⁴⁸	Li ₁₀ GeP ₂ S ₁₂ (single crystal)	Single crystal grown by self-flux method, Au electrodes (paste), measurement along [001] direction	27 (293)	0.39 (204 - 250) 0.29 (250 - 293)
Iwasaki et al. ⁴⁸	Li ₁₀ GeP ₂ S ₁₂ (single crystal)	Measurement along [110] direction	7 (293)	0.40 (208 - 250) 0.30 (250 - 293)
Mo et al. ⁵¹	Li ₁₀ GeP ₂ S ₁₂	First-principle calculations, c direction	40 (300)	0.17
		ab plane	0.9 (300)	0.28
Adams and Prasado Rao ⁶²	Li ₁₀ GeP ₂ S ₁₂	First-principle calculations, c direction	3.5 (300)	0.19
		ab plane	-	0.30

1.4 Nanostructuring

The focus of this work was to experimentally investigate the proposed improvement of the ionic conductivity by reducing the crystallite size down to the nanometer regime, i.e., by nanostructuring. This proposal is based on very recent calculations performed by Dawson and Islam, which indicated an increase of the ionic conductivity by a factor of three.⁷⁴

Generally, reducing the dimensions of materials down to the nanoscale can be applied to tailor mechanical, electronic, optical and magnetic material properties and nanotechnology has been a field of intense research since Feynman's well known talk "There's Plenty of Room at the Bottom".⁷⁵ In solid-state ionics nanostructuring can be applied to increase the ionic conductivity of certain materials.⁷⁶ This can have reasons different from material to material and nanostructuring will not always lead to an enhanced ionic conductivity.⁷⁶ Some of the explanations for altered ion-dynamics in nanostructured materials given below:

Grain boundaries are generally regarded as being detrimental to diffusion and are therefore regarded as barriers to Li-ion migration. However, while this is generally valid for grain boundaries perpendicular to the macroscopic ionic current flow, this does not need to be the case for grain boundaries parallel to the Li-ion migration direction. The reason is that these grain boundaries (parallel to migration direction) have characteristics that facilitate ionic transport, namely high defect densities and interconnected free volume. Additionally, space charge regions might also contribute to enhanced ionic conductivity. However, as grain boundaries parallel to the ionic flow represent only a very small area fraction of the whole solid electrolyte, this kind of conduction might be neglected. But when reducing the grain size down to the nanometer scale, the proportion of grain boundary area becomes higher, and ion migration along the grain boundaries can become significant and contribute to an improved conductivity. But in the end, also the number of grain boundaries perpendicular to the current flow becomes higher, and if ionic conductivity increases or diminishes depends on the relative effects of boundaries perpendicular and parallel to the current flow. This phenomenon is illustrated in Figure 12 a.).⁷⁷

Another explanation for increased conductivity of nanostructured materials demonstrating anisotropic, for example 1D, conduction (as does LGPS) is the reduced probability of highly conductive migration pathways being blocked by defects. As highlighted by Malik et al. for the case of the electrode material LiFePO_4 ⁶⁸ or Iwashita et al. for LGPS⁴⁸, defects might block the 1D diffusion pathways in the structure, and consequently other diffusion pathways must be used to circumvent such blocking defects. In an electrode material like LiFePO_4 this leads to a reduced capacity, for an electrolyte material like LGPS to a reduced conductivity (or increased activation energy). Malik et al. calculated, that if the crystallite size is reduced, the probability of channels having no defects is increased, assuming constant defect density. Translating this to LGPS, this would lead to rapid and long-range Li-ion migration along the c-channels without the need for evasive jumps in the less conductive ab plane. This would result in an increased macroscopic ionic conductivity. This concept is illustrated in Figure 12b.).⁶⁸

Another explanation, somewhat contradicting the previous points, for improved ionic conductivity is the introduced structural disorder, e.g., if the nanostructuring is performed by mechanical ball milling. This was for instance the case for $\text{Li}_6\text{PS}_5\text{I}$ that was ball milled.⁷⁸ In this material, regions with very high Li-ion mobility cannot directly contribute to macroscopic conductivity since energetically unfavorable jumps between these regions are necessary for long-range Li-ion migration.⁷⁸ The introduced disorder by ball milling allowed long-range Li-ion migration without such an unfavorable jump, thereby increasing the ionic conductivity by three orders of magnitude.⁷⁸ Although not directly applicable to LGPS, such disorder could reduce the anisotropy of ionic conduction in LGPS and could change the conduction mechanism from a 1D to a 3D mechanism, as proposed by Dawson and Islam.⁷⁴

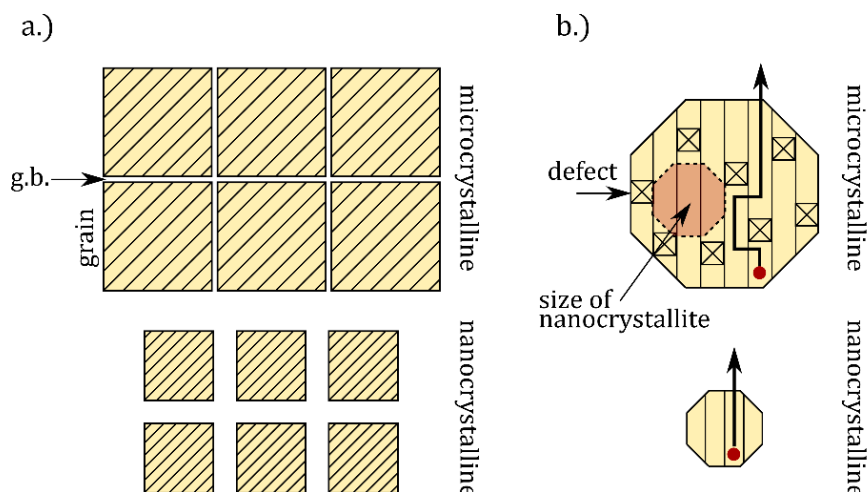


Figure 12: Illustration of a.) the increase in grain boundary area (volume) relative to the total material area (volume) as grain size is reduced to the nanoscale (current flow points into the plane), b.) reduced probability of defect in nanosized grains as opposed to microcrystalline grains.

As mentioned previously, if nanostructuring results in enhanced or impaired ionic conductivity is also a question whether the blocking or conducting (channel-like) character of grain boundaries prevails.⁷⁷ Compared to oxides, sulfides have relatively small grain boundary resistance.³¹ Consequently, sulfides should be good candidates for improved conductivity by nanostructuring.

Dawson and Islam performed large-scale molecular dynamics simulations for the bulk and for nanosized grain volumes of 10 nm³, 100 nm³ and 1000 nm³ for times <10 ns. The conductivities obtained at 300 K were 5.87 mS cm⁻¹, 5.65 mS cm⁻¹, 7.52 mS cm⁻¹ and 15.10 mS cm⁻¹ and the activation energies 0.21 eV, 0.21 eV, 0.24 eV and 0.24 eV, see also Table 3. The calculated values for the bulk are in good agreement with other calculated conductivities^{51,62}, but are underestimating the experimental values¹³. It is evident from the calculated values for the different crystallite sizes, that the biggest jump in conductivity occurs for the reduction of the grain volume from 100 nm³ to 10 nm³. Consequently, the effect of increased ionic conductivity might only become apparent if the average crystallite size is reduced drastically to 2-10 nm.⁷⁴

Table 3: Ionic conductivity σ and activation energy E_a as calculated by Dawson and Islam for different grain volumes. Grain diameters have been calculated from the volume assuming cubic grains. Values denoted with * have been read out from graphs using WebPlotDigitizer.⁷⁴

Grain volume	Grain diameter	σ / mS cm ⁻¹	E_a / eV
Bulk	-	5.87	0.21
1000 nm ³	10.0 nm	5.65 *	0.21
100 nm ³	4.6 nm	7.52 *	0.24
10 nm ³	2.2 nm	15.10	0.24

Dawson and Islam proposed three main points for explaining the enhanced conductivity of nanostructured LGPS in their model:⁷⁴

- Visualization of the Li-ion trajectories and quantifying the diffusion by plotting the mean square displacement in the a, b and c directions yielded anisotropic conduction for the bulk material. The trajectories were oriented mainly in c direction and the mean square displacement was about five times larger in c direction compared to the ab plane. For the nanostructured material however, the trajectories were more evenly distributed, and the mean square displacement curves were similar for all direction. This was interpreted as a more isotropic (3D) conduction in the nanocrystalline material compared to the anisotropic (1D) conduction in bulk LGPS.
- The local structure in nanocrystalline LGPS was visualized by means of the radial distribution functions. Clearly, the radial distribution functions showed an increased amount of disorder, especially the Ge-Ge and P-P functions.
- The ion coordination was calculated for Li-Li and Li-S and yielded that the coordination was on average lower in the nanocrystallites than in the bulk, meaning Li^+ is on average under-coordinated in the nanomaterial.

Such an undercoordination was also recently obtained in calculations performed on Na_3PS_4 and Na_3PO_4 , showing an under-coordination at the grain boundaries for the sulfide and an over-coordination for the oxide. Also, increased intergranular diffusion was observed for the sulfide. This was interpreted as one reason for the comparable low grain boundary resistance of sulfides opposed to oxides.³¹

This under-coordination at the grain boundaries, easier intergranular diffusion and generally the small grain boundary resistance would speak in favor of an increased conductivity by nanostructuring with regard to the previously described effects of grain boundaries perpendicular and parallel to the ionic current.⁷⁷

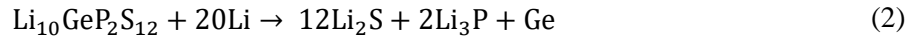
Also, the more isotropic conduction mechanism for the nanocrystalline material becomes noteworthy when considering reports in literature that the room temperature conductivity tends to increase if a more isotropic conduction behavior is observed at room temperature. The pathways available for ionic migration could be mapped in literature by visualization of the Li distribution by applying the maximum entropy method (MEM) to neutron diffraction data. $\text{Li}_{9.81}\text{Sn}_{0.81}\text{P}_{2.19}\text{S}_{12}$ ⁷⁹ had a room temperature conductivity of 5 mS cm^{-1} and no 3D network for Li-ion migration, indicating anisotropic conduction along the c direction. $\text{Li}_{10.35}(\text{Sn}_{0.27}\text{Si}_{1.08})\text{P}_{1.65}\text{S}_{12}$ ⁸⁰ and $\text{Li}_{9.54}\text{Si}_{1.74}\text{P}_{1.44}\text{S}_{11.7}\text{Cl}_{0.3}$ ⁵⁷ with higher conductivities of 11 mS cm^{-1} and 25 mS cm^{-1} showed such a 3D network. This indicated that a more isotropic conduction mechanism benefits higher macroscopic conductivity.³⁸

Notably, the biggest difficulty is the actual synthesis and obtaining nanocrystallites with such small dimension below 10 nm.⁷⁴ However, recently, the successful (solid-state) synthesis of nanostructured $\beta\text{-Li}_3\text{PS}_4$ (structural dimension $\approx 80\text{-}100 \text{ nm}$) was reported, with the nanostructured variant showing improved conductivity.⁴² Also, crystallization of nanocrystalline $\beta\text{-Li}_3\text{PS}_4$ and $\text{Li}_{3.25}\text{P}_{0.95}\text{S}_4$ (size $\approx 5\text{-}20 \text{ nm}$ in (supposed) glass and $30\text{-}60 \text{ nm}$ in glass-ceramic), the later having the LGPS crystal structure, at elevated temperatures in amorphous $\text{Li}_2\text{S}\cdot\text{P}_2\text{S}_5$ was reported.⁸¹ Additionally, as described previously, direct observation of the LGPS crystallization processes indicated a sluggish grain growth process, which should facilitate the synthesis of nanocrystalline materials.⁵⁰ An additional way would be a wet-chemical synthesis route, however, until now only the precipitation of amorphous phase from solutions was reported in literature.^{49,58}

1.5 Oxygen substitution and application in solid-state batteries

Originally, LGPS was attributed with a high electrochemical stability based on cyclic voltammetry with a Li/LGPS/Au cell and with a scan range of -0.5 V to 5 V.¹³ First-principle simulations soon showed that the stability window of LGPS should be much smaller and yielded decomposition at the low Li metal potential with the formation of Li_2S , Li_3P , and $\text{Li}_{15}\text{Ge}_4$.⁵¹ Also, at high potentials possibly encountered at the cathode, decomposition was predicted with the formation of P_2S_5 , S and GeS_2 .⁵¹ However, the possibility of the decomposition product forming a passivating SEI was highlighted.⁵¹ Later experimental investigations confirmed the increase in resistivity of the electrolyte due to the formation of a SEI at the electrode-electrolyte interface.⁸² Results also indicated that the reduction of Ge at low potentials promotes the decomposition of the solid electrolyte in contact with the Li metal.⁸² This is also clear in the view that metals can normally be reduced and oxidized easier compared to phosphorus and other non-metals.⁸²

The theoretical results mentioned were later confirmed experimentally. Using XPS to probe the electrode-electrolyte interface the chemical composition of the SEI was reported to be Li_2S , Li_3P and elemental Ge (or Ge-Li alloy, should be thermodynamically favored).⁸³ Followingly, the decomposition reaction of LGPS with metallic Li was proposed to be:⁸³



or



Important to note is that the metallic Ge (volume fraction ≈ 4 %) does not form a percolating network and the SEI can therefore still be electronically insulating and passivating.⁸³

Consequently, in order for commercial application of LGPS to become feasible, the stability against Li metal has to be improved. One approach is, see Synthesis section, to substitute cations and anions in the LGPS structural framework, as a wide range of properties, including enhanced electrochemical stability, should be accessible by doping. Followingly, one way of increasing the stability against metallic Li reported by Sun et al. is the substitution of sulfur in the LGPS structure by oxygen.⁴⁶ This enhanced electrochemical stability should be due to stronger bonding between Ge-O as compared to Ge-S.⁴⁶

First-principle band gap calculation indeed indicated a higher intrinsic redox stability for the completely oxygen substituted variant of LGPS ($\text{Li}_{10}\text{GeP}_2\text{O}_{12}$). However, calculations of phase equilibria of $\text{Li}_{10}\text{GeP}_2\text{O}_{12}$ open to lithium (relevant if the material is in contact with an electrode) yielded again decomposition to $\text{Li}_{15}\text{Ge}_4$, Li_2O and Li_3P at the Li metal anode and decomposition to GeP_2O_7 and O_2 at the cathode. Especially the evolution of O_2 at the cathode could be fatal, but such reaction was not yet reported experimentally in literature.⁵⁴

Followingly, oxygen-substituted LGPS, $\text{Li}_{10}\text{GeP}_2\text{S}_{12-x}\text{O}_x$, was synthesized and the formation of a solid-solution until $x = 0.9$ was confirmed. The cycling performance of a Li/LGPS/(LiNbO₃-coated)-LiCoO₂-LGPS-composite solid-state battery was evaluated and was significantly better for the oxygen-substituted LGPS variant. 8 % capacity remained after 10 cycles for the battery using $\text{Li}_{10}\text{GeP}_2\text{S}_{12}$ and 30 % for the battery using $\text{Li}_{10}\text{GeP}_2\text{S}_{11.4}\text{O}_{0.6}$. However, it must be noted that for both $\text{Li}_{10}\text{GeP}_2\text{S}_{12-x}\text{O}_x$ and conventional $\text{Li}_{10}\text{GeP}_2\text{S}_{12}$ the capacity fading is still high, indicating that decomposition at the electrode-electrolyte interface was not completely suppressed and must be further reduced.⁴⁶

2 Methods

2.1 X-ray powder diffraction (XRD)

There are many methods of materials characterization based on X-ray diffraction. Some examples are single crystal X-ray diffraction, small angle X-ray scattering and X-ray powder diffraction. The most common technique in solid-state chemistry is X-ray powder diffraction and can be used for easy and quick identification of phases, crystallite size analysis or the determination of crystal structures. The supreme method for solving crystal structures is single crystal X-ray diffraction and it is often this method that provides the basis for the interpretation of powder patterns.⁸⁴

The physical background for these techniques is the diffraction of X-rays at periodic structures, similar to the well-known double-slit experiment. However, the length scale of periodic structures in crystalline materials is of the order of 10^{-10} m, i.e., a few Å, and diffraction only occurs if the wavelength λ has the same magnitude as the length scale of the periodic structure.⁸⁴ Therefore, diffraction takes place if X-rays, which possess a sufficiently small wavelength in the range of 10^{-10} m, or otherwise also electrons or neutrons (De Broglie relation) with a high enough velocity, are used in diffraction experiments.⁸⁵

At the heart of diffraction lies that differences in path traveled by two waves translate into differences in phase, leading to destructive (if the phase difference is $n\lambda/2$, n being a positive integer number) or constructive (if the phase difference is 0 or $n\lambda$) interference. Diffraction is then the result of many scattering events at the atoms composing the crystal. Scattering is an elastic interaction and rays can be scattered in all possible directions. However, although rays are scattered in all directions, only in a few the path difference of the individual rays is 0 or a multiple of the wavelength. In these directions, constructive interference between the individual rays will occur and a diffracted beam (consisting of all the “correctly” scattered rays) of sizable intensity forms. Mathematically, this requirement can be described by Bragg’s law:⁸⁶

$$2 \cdot d_{hkl} \cdot \sin(\theta) = n \cdot \lambda \quad (4)$$

with λ being the wavelength, d_{hkl} the spacing between the lattice planes (hkl), n an integer number and θ the angle between the incident / diffracted beam and the sample surface. If Bragg’s law is fulfilled, the individual scattered rays interfere in a constructive way and constitute a diffracted beam of detectable intensity, as illustrated in Figure 13. Because of the geometric constraints the angle of incident θ equals the exit angle θ , like for reflection. However, it should be noted that diffraction and reflection are fundamentally different phenomena.⁸⁶

It should be mentioned that Bragg’s law is a necessary yet not sufficient condition for diffraction.⁸⁷ For a more complete and physically accurate model a solid-state physical approach including reciprocal space, atomic form factors and structure factors would be required. This is however not in the scope of this thesis and will not be discussed further.

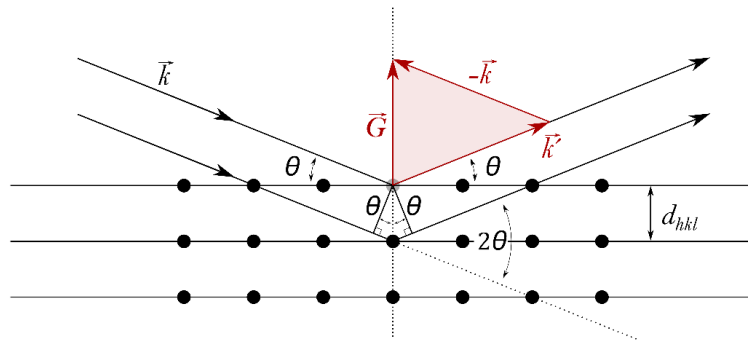


Figure 13: Illustration of the requirements for diffraction in real space by Bragg's law. The wavevector of the incoming and outgoing beam are denoted as \vec{k} and \vec{k}' , and the scattering vector as \vec{G} . θ is the angle between the incident beam / diffracted beam and the lattice plane. The scattering angle 2θ is the angle between the incident and the diffracted beam.

When applying X-ray diffraction for materials characterization there are multiple assumptions one must make regarding the used radiation, the sample, and the interaction mechanism:^{86,88,89}

- Sample consists of periodic, well-defined crystals.
- sufficient material
- coherent radiation
- monochromatic radiation
- parallel radiation
- elastic and coherent interaction mechanism
- only one scattering event per X-ray

The first two assumptions refer to the specimen under investigation. The first is obvious since periodicity is an essential prerequisite for diffraction. However, it should also be mentioned that samples with only short-range order, i.e., glassy materials, can give reasonable results too although the patterns of such materials do not contain distinct peaks but diffuse halos and bands.⁸⁸ Since the interaction of X-rays with matter is relatively weak, enough material needs to be present (criterion of “infinite thickness”) to ensure a large number of diffraction events and followingly signal intensity.⁸⁶

X-rays are produced in an X-ray tube. Electrons are accelerated by an electric field, hitting a target normally consisting of Cu. When the electrons interact with the target, a continuous spectrum of “white” radiation (called “Bremsstrahlung”) and, superimposed on it, target-characteristic radiation are emitted.⁸⁴ The characteristic radiation is nearly monochromatic and has a significantly higher intensity compared to the continuous spectrum and is therefore preferred for characterization.⁸⁶ After filtering out the “Bremsstrahlung” by using a material with atomic number $Z_{\text{target}} - 1$, nearly monochromatic radiation leaves the tube.⁸⁶ In the case of a Cu target a radiation doublet is emitted, consisting of $K_{\alpha 1}$ and $K_{\alpha 2}$ radiation.⁸⁸ Afterwards the X-rays are parallelized using a collimator and the divergency is minimized using slits.⁸⁸ A monochromatic source is necessary since only with radiation of defined λ discrete peaks at certain angles 2θ , fulfilling Bragg's law, are observable.⁸⁶ Similar considerations concerning the parallel nature of the incident beam can be done. Since the phenomenon of diffraction involves interference, a constant phase relation, i.e., coherency, is another logic prerequisite for a useful diffraction experiment.⁸⁶

The last two assumption apply to the scattering event itself. Elastic and coherent interactions are the inherent nature of scattering events during diffraction. That only one scattering event per X-ray takes place is a reasonable assumption since the interaction of X-rays with matter is relatively weak. If there would be multiple scattering events per ray, additional considerations exceeding the previous treatment would be necessary as is the case in the dynamic theory of X-ray diffraction.⁸⁹

For X-rays, the scattering occurs at the electrons. Therefore, atoms with higher atomic number Z interact stronger with X-rays, and X-ray diffraction is more sensitive to these elements. Followingly, light atoms like H or Li can hardly be observed by means of XRD and therefore neutron diffraction is used for such elements. Consequently, the electron density of a material is probed in X-ray diffraction experiments.⁸⁵

The most widely spread technique for material characterization using X-rays is X-ray powder diffraction. The general set-up of the apparatus is illustrated in Figure 14 a.). As mentioned previously, X-rays are generated in an X-ray tube. Through a slit and a collimator the radiation is guided to the sample. The sample is a powder in most cases, but polycrystalline bulk samples or thin films are also possible. If diffraction is performed with a single crystal sample, at any instance there is only a small probability for a set of lattice planes to be oriented in the correct way. Therefore, when performing single crystal X-ray diffraction, the sample needs to be rotated in all three dimension and the reflexes recorded in space. However, in a polycrystalline sample many crystallites are oriented randomly in all directions, so at every instance at least some crystallites will be oriented right if a set of lattice planes fulfilling Bragg's law exists, see inset Figure 14 a.). Therefore, a far simpler set-up can be used, only varying the scattering angle 2θ in one direction and recording the intensity of the diffracted beam as depicted in Figure 15. Another way of illustrating this would be that in transmission mode, instead of a single diffracted beam, a whole cone of diffracted beams would be generated with the semiapex angle of the cones corresponding to 2θ .⁸⁴

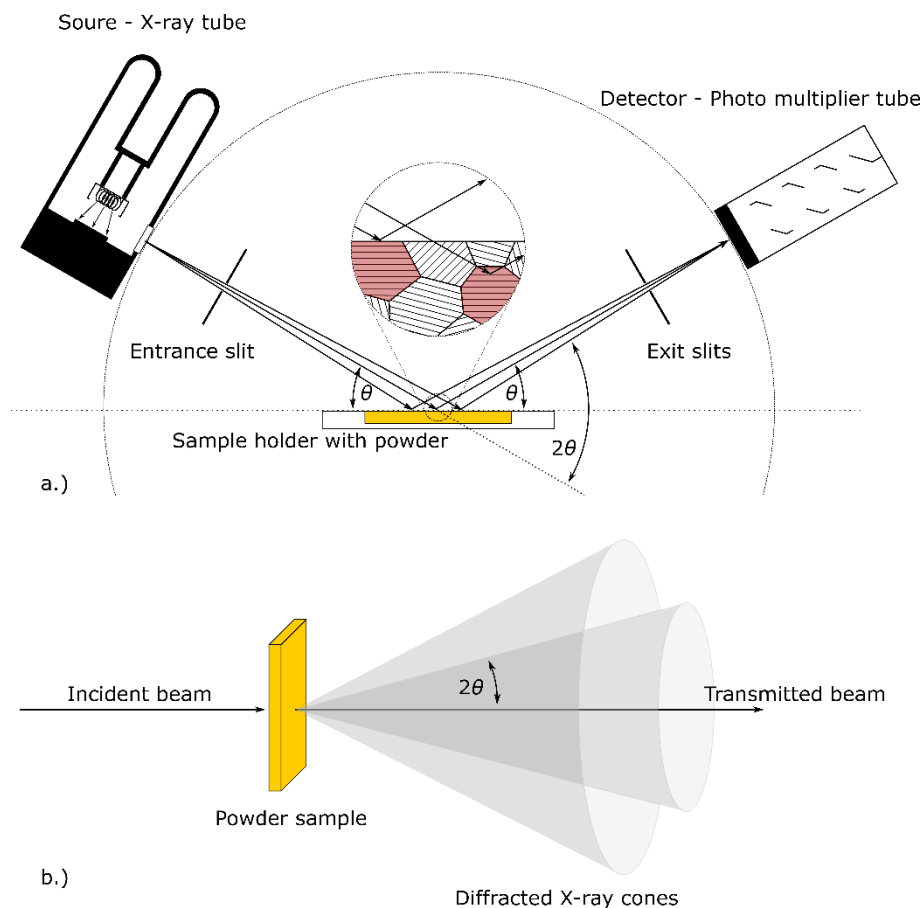


Figure 14: a.) Illustration of powder X-ray diffraction in the common Bragg-Brentano geometry. The inset (inspired by Birkholz⁹⁰) illustrates the polycrystalline nature of the sample with grains in red being oriented correctly for diffraction. b.) Illustration of powder X-ray diffraction in transmission mode (similar to Hull/Debye-Scherrer method). Inspired by Smart and Moore.⁸⁴

For X-ray powder diffraction the detector is a scintillator followed by a photomultiplier tube. During a scan, the incident angle is varied by θ and the scattering angle by 2θ , see Figure 13. Instruments achieve this either by tilting the sample by θ and the detector moves by 2θ or by moving both source and detector by θ clockwise and anti-clockwise, respectively. During this procedure, source (entrance slit), sample surface and detector (exit slit) are all located on a focusing circle. This means the rays that are diffracted at the sample become again focused on the detector (exit slit), maximizing the measured signal. This overall instrumentation set-up is the most common one and is called the Bragg–Brentano mode.⁸⁶

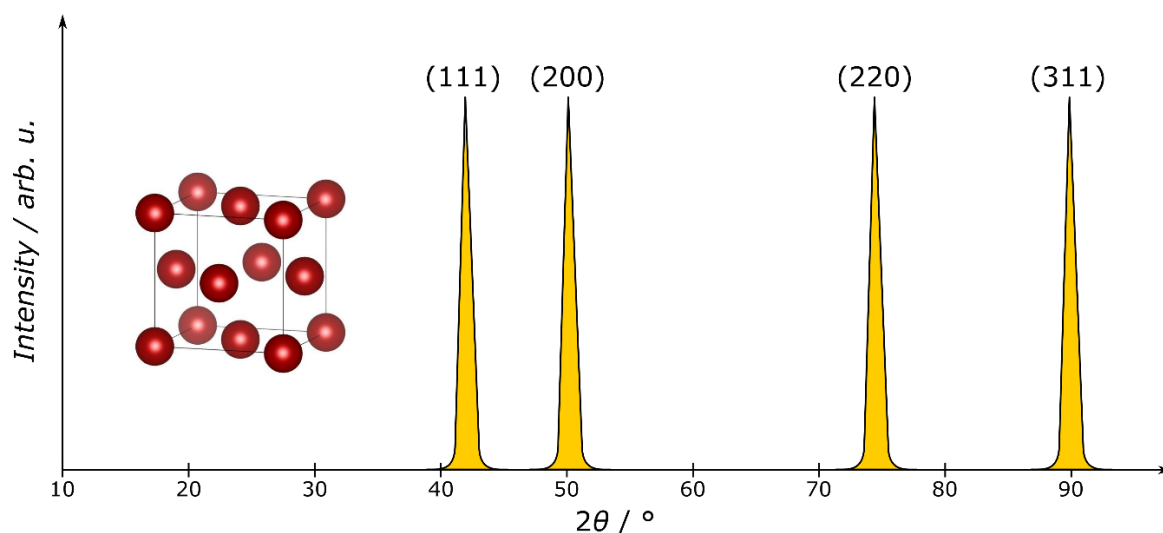


Figure 15: Illustration of the X-ray powder diffraction pattern of metallic Cu with an fcc crystal structure as seen in the inset at the left. Data for peak positions from Cullity.⁸⁶

The main way of interpreting powder diffraction data is by comparing the pattern with extensive databases and libraries. This allows a fast and easy phase identification of already solved phases. For solving an entirely new structure one normally needs to use single crystal X-ray diffraction. The reason for this is that for complex phases the number of lines increases, and peak overlap becomes a significant problem for indexing the pattern and determining intensities correctly.⁸⁴

Although, as mentioned previously, powder diffraction is not the method of choice for solving unknown crystal structures, there are some ways of structure determination using powder patterns. Generally, it is an easy task to calculate a diffraction pattern from a given crystal structure. This fact can be used for the analysis of diffraction data. One of the most widely employed methods for determining crystal structures from powder patterns is Rietveld refinement. In this method not only the individual peaks with their respective positions and intensities are calculated, but the overall line profile of the pattern is calculated and analyzed. Each peak is assigned a gaussian (or similar) shape and overlapping gaussians are simply added up. This allows the treatment of more complex patterns that contain many overlapping peaks. An already solved crystal structure acts as starting point of such a refinement. The obtained calculated pattern can then be altered. Commonly changed parameters are the background, the zero shift, peak-shape functions, profile parameters and lattice constants. More elaborated analysis might involve substitution of atoms and the shift of atomic positions. The calculated and observed powder patterns can be compared and checked for agreement. This process can then be repeated, manually or automatically, until a best-fit match is achieved.^{84,91}

The quality of the calculated pattern is assessed by using agreement indices: ⁹²

$$R_{\text{wp}}^2 = \frac{\sum_i w_i (y_{\text{C},i} - y_{\text{O},i})^2}{\sum_i w_i (y_{\text{O},i})^2} \quad (5)$$

$$R_{\text{exp}}^2 = \frac{N}{\sum_i w_i (y_{\text{O},i})^2} \quad (6)$$

$$\chi^2 = \left(\frac{R_{\text{wp}}}{R_{\text{exp}}} \right)^2 \quad (7)$$

The weighted profile R-factor R_{wp} indicates the agreement of the calculated and the experimental pattern, with $y_{\text{C},i}$ being the calculated intensity at point i , $y_{\text{O},i}$ the observed intensity and w_i the weighting factor equal to $1/\sigma_{\text{O},i}^2$ ($\sigma_{\text{O},i}$ being the standard uncertainty). R_{exp} indicates the best possible fit based on the noise in the data (patterns with worse signal-to-noise ratio have larger R_{exp}), with N being the number of data points. The goodness of fit χ^2 gives the ratio of these two. The goodness of fit should be as close as possible, but never be below, 1.⁹²

Another useful characteristic of powder X-ray diffraction is that the line width is related to the crystallite size in the sample, with reduced crystallite size leading to line broadening.⁸⁸

However, it is important to note that also instrumental factors unavoidably lead to line broadening, for example X-ray beams have finite width and are not perfectly parallel. Consequently, one must account for such instrumental factors with standards before using the line broadening as a quantitative measure of crystallite size. However, qualitative statements are also possible without proper calibration.⁸⁹

The line broadening is described by the Scherrer equation:⁹³

$$\tau = \frac{K \lambda}{\beta \cos(\theta)} \quad (8)$$

With K being the Scherrer constant (or shape factor), β is the line broadening (fwhm), τ the mean crystallite size and θ the angle between the incident / diffracted beam and the sample surface. This equation allows the determination of the size of sub-micrometer crystallites.⁹³

2.2 Impedance and conductivity spectroscopy

Impedance spectroscopy (IS) allows to probe the macroscopic response of a system to an applied electric field as a function of frequency. It is the most widespread technique for investigating the dynamics in ionic conductors. The biggest advantage of impedance spectroscopy is the broad frequency range that can be applied, typically ranging from mHz to MHz, but extendable to the nHz to THz regime.⁹⁴

In IS a sinusoidal (ac) voltage signal ($= V(t)$) with a defined amplitude and frequency is applied to the sample and the amplitude and phase shift of the resulting alternating current ($= I(t)$) are measured. All other quantities associated with IS are then calculated from the amplitude and phase shift. Mathematically, both stimulus and response can be written as:⁹⁴

$$V(t) = V_0 \cdot \sin(\omega t) \quad \text{and} \quad I(t) = I_0 \cdot \sin(\omega t - \delta) \quad (9)$$

With V_0 being the voltage amplitude, ω the angular frequency ($= 2\pi\nu$) of the applied voltage, t the time, I_0 the amplitude of the current response and δ the phase shift.⁹⁴ To facilitate calculations, voltage and current are more often written as:

$$V(t) = V_0 \cdot e^{i\omega t} \quad \text{and} \quad I(t) = I_0 \cdot e^{i(\omega t - \delta)} \quad (11)$$

The above equations describing stimulus and response are only valid if the prerequisites of linearity and causality are fulfilled for the measurement.⁹⁵

By introducing the concept of impedance, voltage and current can be connected. The impedance is derived by considering all possible, basic responses of an electrical circuit to an applied voltage. There are three such (pure) responses, each represented by a lumped circuit element: resistance (resistor), capacitance (capacitor) and inductance (inductor), see Table 4. Considering a circuit of all these elements in series, see Figure 16, and adding up the individual contributions yields the following differential equation:⁹⁶

$$V(t) = L \cdot \frac{d^2q}{dt^2} + R \cdot \frac{dq}{dt} + \frac{q}{C} \quad (13)$$

With q being charge, t time, L the inductance, R the resistance and C the capacitance. Solving this differential equation using equations 11 and 12 as voltage and current and using $I = dq/dt = i\omega q$ yields an expression connecting the applied voltage and the measured current response:⁹⁶

$$V(t) = \left(i\omega L + R + \frac{1}{i\omega C} \right) \cdot I(t) = Z \cdot I(t) \quad (14)$$

This equation resembles very much Ohm's law. The term in brackets is defined as the impedance and describes the current response when an ac voltage is applied to this particular circuit depicted in Figure 16. The impedances of the individual lumped circuit elements are summarized in Table 4.⁹⁶ These impedances, like resistances, can be summed up using the conventional rules of electrical engineering, giving the response of an arbitrary circuit composed of lumped circuit elements i :⁹⁶

$$\text{series: } Z_{\text{tot}} = \sum_i Z_i \quad \text{and} \quad \text{parallel: } \frac{1}{Z_{\text{tot}}} = \sum_i \frac{1}{Z_i} \quad (15)$$

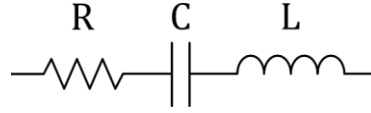
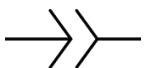


Figure 16: Resistor, capacitor, and inductor in series.

Table 4: Lumped circuit elements applied for equivalent circuits in impedance spectroscopy.

Lumped circuit element	Physical Phenomena	Equation	Impedance
Capacitor 	dielectric response	$V = \frac{q}{C}$	$Z = \frac{1}{i\omega C}$
Resistor 	resistivity of electrolyte	$V = R \cdot I = R \cdot \frac{dq}{dt}$	$Z = R$
Inductor 	passivation layer, corrosion	$V = L \cdot \frac{dI}{dt} = L \cdot \frac{d^2q}{dt^2}$	$Z = i\omega L$
Constant phase element 	dielectric response of non-Debye process	-	$Z = \frac{1}{(i\omega)^n C}$

Consequently, from the measured data at different frequencies the impedance can be calculated as:⁹⁴

$$Z(\omega) = \frac{V(t)}{I(t)} = \frac{V_0}{I_0} \cdot \frac{e^{i\omega t}}{e^{i\omega t - \delta}} = Z_0 \cdot e^{i\delta} = \frac{V(\omega)}{I(\omega)} \quad (16)$$

With Z_0 being the modulus of the impedance. It should be noted that in IS we normally work with the Fourier Transforms of the current and voltage signals, $V(\omega)$ and $I(\omega)$. The impedance is a complex quantity and can be separated into a real and imaginary part, with the real part of impedance giving the usual resistance (associated with energy loss) and the imaginary part, called reactance, giving the capacitive and inductive response (no associated energy loss) (Z^* is written instead of Z to highlight the complex character of the impedance):^{94,97}

$$Z^* = Z' + iZ'' = Z_0 \cos(\delta) + iZ_0 \sin(\delta) \quad (17)$$

The right term in equation 17 describes the impedance in polar coordinates, see Figure 17 b.), with:⁹⁴

$$Z_0 = \sqrt{Z'^2 + Z''^2} \quad (18)$$

$$\delta = \tan^{-1} \left(\frac{Z''}{Z'} \right) \quad (19)$$

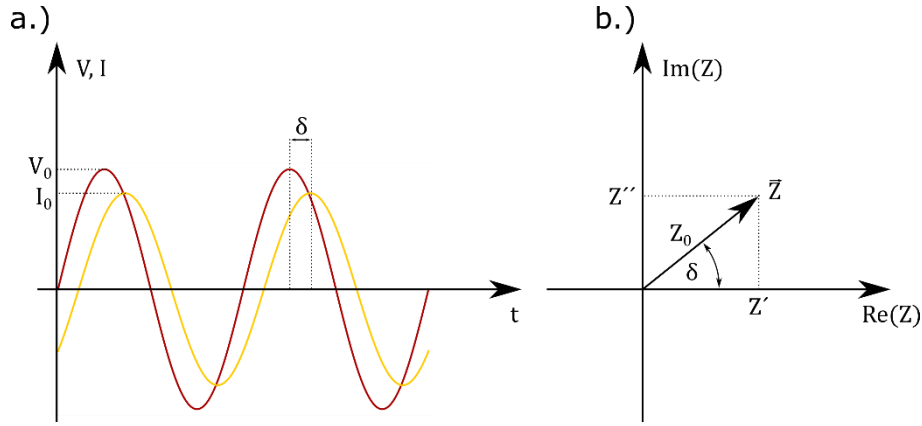


Figure 17: Illustration of a.) an applied sinusoidal voltage and current response and b.) the impedance plotted in the complex plane.

Besides the impedance Z^* , its modulus (Z_0) and phase angle (δ) there are many other representations that can describe the response of the sample. All these quantities are called immittance functions and it is straightforward to calculate any of them from the measured amplitude and phase shift. Different immittance functions are advantageous for bringing out certain characteristics of the response. Important immittance functions include the complex conductivity σ^* and the complex electric modulus M^* :⁹⁴

$$\sigma^* = \frac{1}{Z \cdot C_0} \quad (20)$$

$$M^* = i\omega C_0 Z \quad (21)$$

$$\text{with } C_0 = \varepsilon_0 \cdot \frac{A}{d} \quad (22)$$

With Z being the complex impedance, C_0 the capacitance of the empty measurement cell, ω the angular frequency, and ε_0 the vacuum permittivity. The real part of the complex conductivity σ' can be interpreted as the conventional (electronic and ionic) conductivity $\sigma = 1/\rho$ (with ρ being the resistivity) of the material and the imaginary part of the electric modulus M'' has the same physical interpretation as the imaginary part of the impedance Z'' (capacitive and inductive contributions) but with higher selectivity for processes of larger capacitance like bulk processes.⁹⁴ The most important part of impedance spectroscopy is obtaining these immittance functions as a function of frequency, allowing extensive information gain about the response and dynamics of the sample under investigation.

When considering a simple system, the response of a sample could look like in Figure 18, with the response changing significantly as the frequency is scanned. This behavior is often modelled by using a so-called equivalent circuit, see again Figure 18. Each element in the circuit represents a physical process and/or a distinct region of the sample. The impedance for the whole circuit is obtained by adding up the contributions of the individual elements using equation 15. The circuit in Figure 18 is very common and referred to as an RC-element. For this simple parallel circuit the impedance is:⁹⁴

$$Z' = \left(\frac{1}{R}\right) \left(\frac{1}{R^2} + (\omega C)^2\right)^{-1} \quad (23)$$

$$Z'' = (-\omega C) \left(\frac{1}{R^2} + (\omega C)^2\right)^{-1} \quad (24)$$

If Z' is plotted on the x-axis and $-Z''$ on the y-axis a so-called Nyquist plot is obtained, a very common way of representing impedance data. The ideal RC-circuit yields a semi-circle in the Nyquist plot as seen in Figure 18 a.). At low frequencies, the capacitor gets fully charged and blocking. Consequently, the current flows over the resistor R , which dominates the response of the system in this case. Therefore, the reactance Z'' and phase shift are zero (see equations 19 and 24) and Z' equals the resistance of the resistor R (see equation 23 and Figure 18 b.) and c.)). At intermediate frequencies, the RC-circuit shows a resonance-like behavior with a maximum in Z'' and a drastic change in Z' . The resonance-like behavior can be clearly seen in the Bode plot, see Figure 18 b.). At high frequencies, the capacitor becomes non-blocking and most current flows over the capacitor with no resistance impeding the current. As a result, the resistance is zero and the phase shift is 90° , typical for a pure capacitor.⁹⁴

The response discussed above and illustrated in Figure 18 corresponds to an ideal Debye behavior. In this case the equivalent circuit (and consequently the atomic process it models) exhibits a characteristic relaxation time constant τ and a maximum in Z'' if ω equals τ^{-1} (equivalent to a resonance condition).^{94,95}

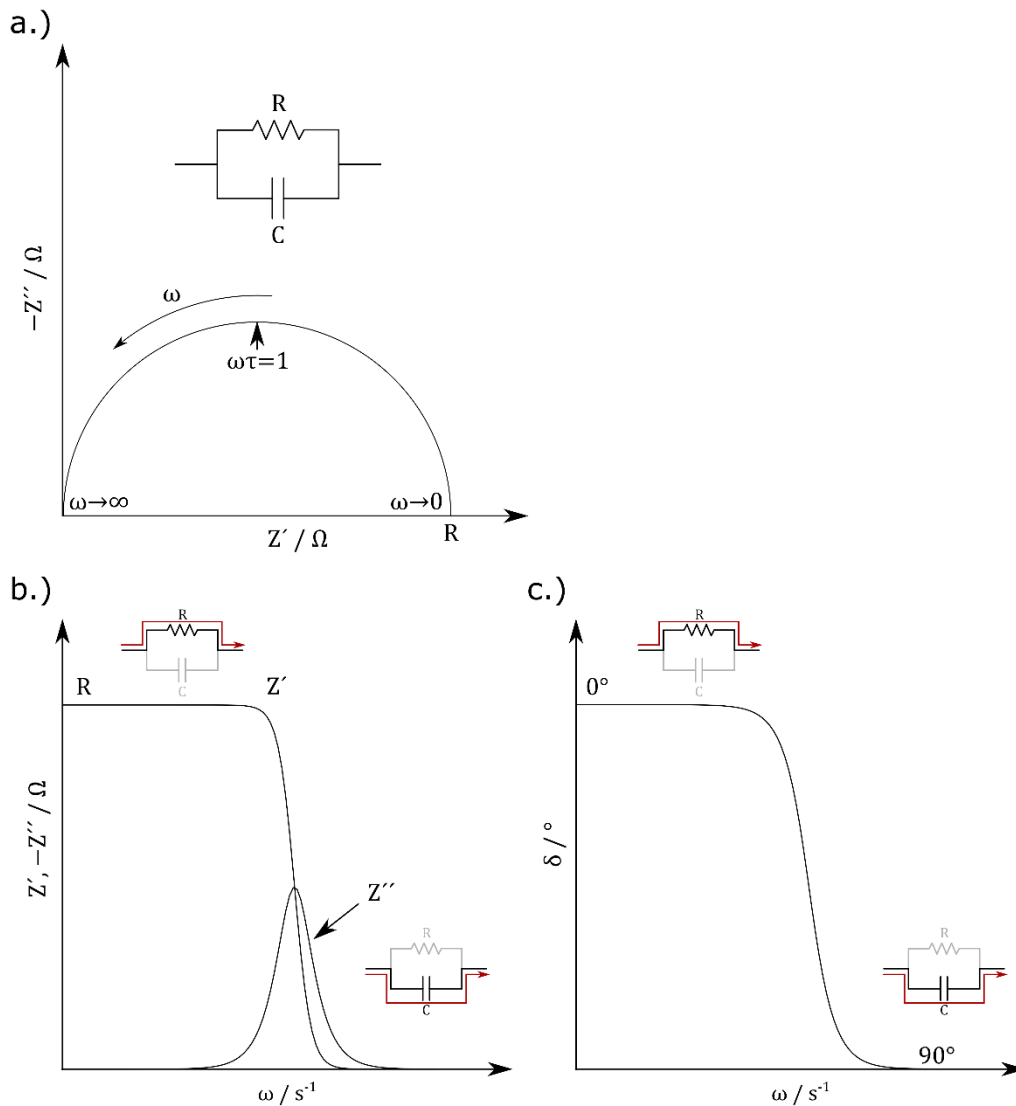


Figure 18: Illustration of the ideal RC response to an applied voltage of variable frequency. a.) Nyquist plot visualizing the response in the complex plane, b.) Bode plots showing the response as function of frequency, highlighting the resonance character, c.) Change of the phase shift with frequency. Insets in b.) and c.) indicate the majority current flow at low and high frequencies.

Using such equivalent circuits is the most common way of quantitatively interpreting impedance data and many systems can be described by using RC-elements in series, see Figure 19. However, as mentioned previously, every circuit element in an equivalent circuit must represent a physical process and/or region of the investigated sample. Equivalent circuits are very powerful tools for interpretation, but at the same time one of the largest disadvantages of impedance spectroscopy is the possible ambiguity associated with this way of interpretation. Certain circuit elements might be introduced arbitrary without good physical reasoning and often more complex equivalent circuits can be rearranged while still yielding the same results. Another drawback is the use of idealized lumped circuit elements itself, which cannot perfectly describe the response of the real system with an independent distribution of microscopic properties.⁹⁵

One consequence of such a distribution of microscopic properties (Non-Debye relaxation) is that there might be no single relaxation time constant τ , but a distribution of τ values around a mean value τ_m . In the Nyquist plot this presents itself as a depressed semi-circle. Such behavior can be modeled with the constant phase element (CPE), a widely applied and important lumped circuit element, see Table 4. The constant phase element allows to model the dispersion of the conductivity at high frequencies that is usually observed in ionic conductors⁹⁴ and the distribution of properties and relaxation time constants⁹⁵. Another non-ideal aspect of many Nyquist plots is that semi-circles can be substantially influenced and distorted by other arcs if the differences in mean relaxation times are smaller than two orders of magnitude.⁹⁵

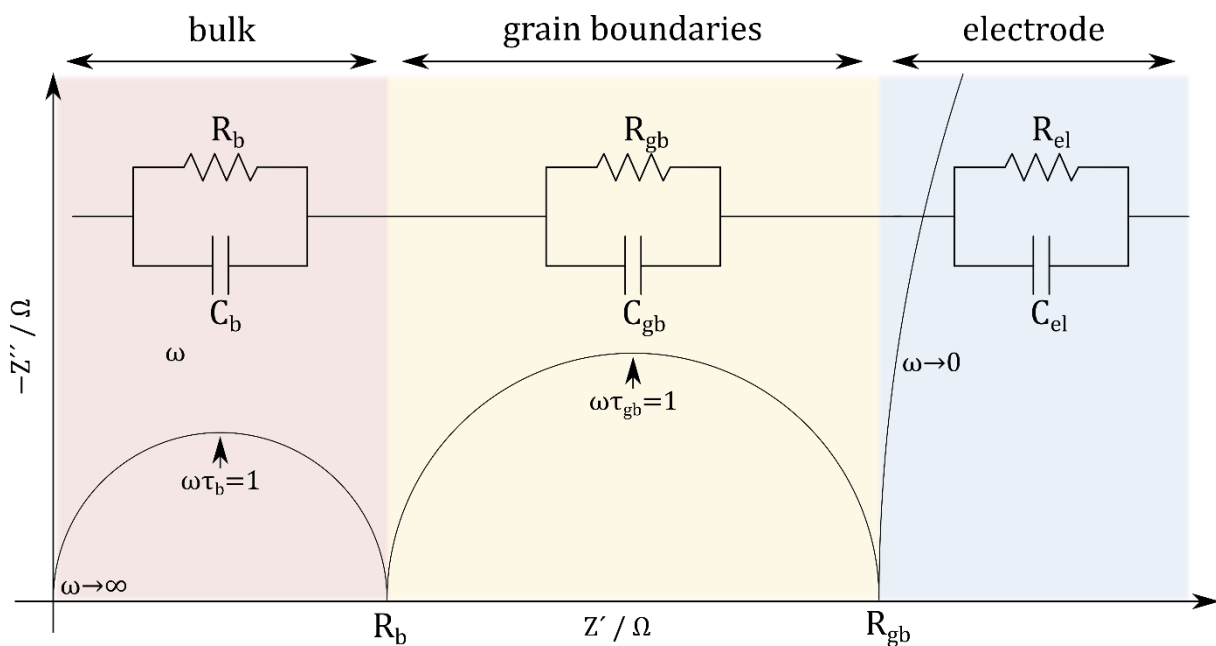


Figure 19: Illustration of the ideal electric response of a polycrystalline material, including bulk, grain boundary and electrode contributions. Inspired by Mehner⁹⁸.

Fitting with equivalent circuits yields the capacitance of each RC element, which is a very important parameter for assigning such elements to distinct contributions from the sample. The reason is that certain contributions have characteristic capacity ranges, see Table 5.⁹⁹

Table 5: Capacitance values and possible responsible phenomena.⁹⁹

Capacitance / F	Phenomenon responsible
10^{-12}	bulk
10^{-11}	minor, secondary phase
$10^{-11} - 10^{-8}$	grain boundaries
$10^{-10} - 10^{-9}$	bulk ferroelectric
$10^{-9} - 10^{-7}$	surface layer
$10^{-7} - 10^{-5}$	sample-electrode interface
10^{-4}	electrochemical reactions

Another important way of interpreting the experimental data is plotting the real part of the complex conductivity, σ' , against the frequency ν with double logarithmic scale, obtaining a so-called conductivity spectrum, showing the evolution of conductivity with frequency, see Figure 20. The distinct regions (bulk and grain boundaries) of the sample are visible as plateaus in the conductivity spectrum and the conductivity values at these plateaus can be interpreted as the dc conductivity of these regions. When such lines, acquired at different temperatures, are plotted in a single graph, each line is called a conductivity isotherm. It is also common to refer to this technique as conductivity spectroscopy instead of impedance spectroscopy.^{29,98}

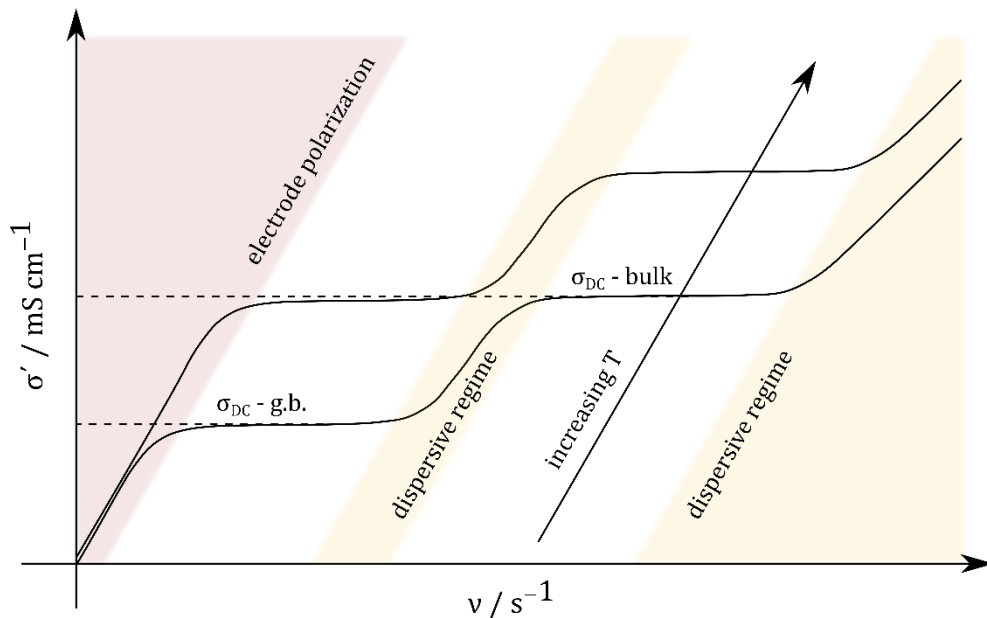


Figure 20: Illustration of isotherms in a plot of conductivity against frequency with double logarithmic scaling.

It is common to perform impedance measurements at different temperatures. The conductivity in many solids shows Arrhenius behavior according to the relation $\sigma_{DC}T \sim \exp(-E_a/k_bT)$. Consequently, by plotting the measured conductivity at different temperatures in an Arrhenius plot the activation energy of the conduction process can be obtained.^{29,98}

Another reason is that by altering the temperature the characteristic rates of thermally activated process in the sample change. This enables the shift of the characteristic relaxation rates into the frequency range observable by the impedance equipment. Like this, otherwise too fast process can be probed at low temperatures and too slow processes at elevated temperatures.⁹⁴

The dc conductivity obtained by impedance spectroscopy can be used to calculate the charge diffusion coefficient using the Nernst-Einstein equation:⁹⁸

$$D_{\sigma} = \frac{k_b T}{Nq^2} \sigma_{DC} \quad (25)$$

With N being the number density of charge carriers, q the charge of a single charge carrier, σ_{DC} the dc conductivity obtained by impedance spectroscopy, k_b the Boltzmann constant and T the temperature. Calculation of the charge diffusion coefficient allows a more quantitative comparison of the results for ion dynamics from impedance spectroscopy and NMR (spin-lattice relaxometry).

2.3 Nuclear magnetic resonance (NMR) spectroscopy

Considering the amount and detail of information on structure and dynamics of materials, NMR is unmatched by any other characterization method for condensed matter. Compared with the conventional liquid-phase NMR, solid-state NMR is more complex, with more interactions involved, many of which are neglectable for liquid-phase NMR.¹⁰⁰

2.3.1 Theory

NMR is based on the magnetic moment of atoms with a nucleus with non-zero spin. Almost every element in the periodic Table has an isotope with non-zero nuclear spin, however an additional requirement for applicability is sufficient abundance.⁹⁴ Such nuclei have a spin angular momentum I and followingly a magnetic moment $\vec{\mu}$:¹⁰⁰

$$\vec{\mu} = \gamma \cdot \vec{I} \quad (26)$$

With γ being the nucleus specific gyromagnetic ratio. Since the spin angular momentum and the magnetization are properties of a single particle, they are subjected to orientational quantization (typically assumed for the z-component, as external magnetic fields are conventionally assumed to be in z-direction):¹⁰⁰

$$|I_z| = m \cdot \hbar \quad (27)$$

$$\mu_z = \gamma \cdot m \cdot \hbar \quad (28)$$

With m being the magnetization quantum number. By applying an external magnetic field with the magnetic flux density B_0 these states become energetically inequivalent and consequently observable, see Figure 21 a.). This is due to the Zeemann interaction described by the equation:¹⁰⁰

$$E_m = -\mu_z \cdot B_0 = -\gamma \cdot m \cdot \hbar \cdot B_0 \quad (29)$$

This results in $(2I + 1)$ energetically inequivalent states, i.e., in the case a nucleus with $I = 1/2$ two states with energies of $E_m = -\frac{1}{2}\gamma \cdot \hbar \cdot B_0$ and $E_m = +\frac{1}{2}\gamma \cdot \hbar \cdot B_0$ and followingly with a total energy difference of $\Delta E = \gamma \cdot \hbar \cdot B_0$, see Figure 21 b.) Since the magnetic moment is directly coupled to the spin angular momentum and angular momentum conservation must be valid, the individual atomic magnetic moments precess about an axis parallel to the magnetic field B_0 .⁹⁷ This precession occurs with the Larmor frequency given by:⁹⁴

$$\omega_L = \gamma \cdot B_0 \quad (30)$$

To summarize and continuing with the example of a nucleus with $I = 1/2$, the Zeeman interaction results in the magnetic moments (and the spins) being aligned either parallel or antiparallel to the magnetic field with the majority being in parallel orientation since it is energetically more favorable. Furthermore, all these spins precess with the Larmor frequency $\omega_L \sim B_0$ about an axis parallel to the magnetic field. This is illustrated in Figure 21 c.) This alignment results in a macroscopic equilibrium magnetization M along the z-axis called the longitudinal magnetization, see Figure 21 c.).¹⁰⁰

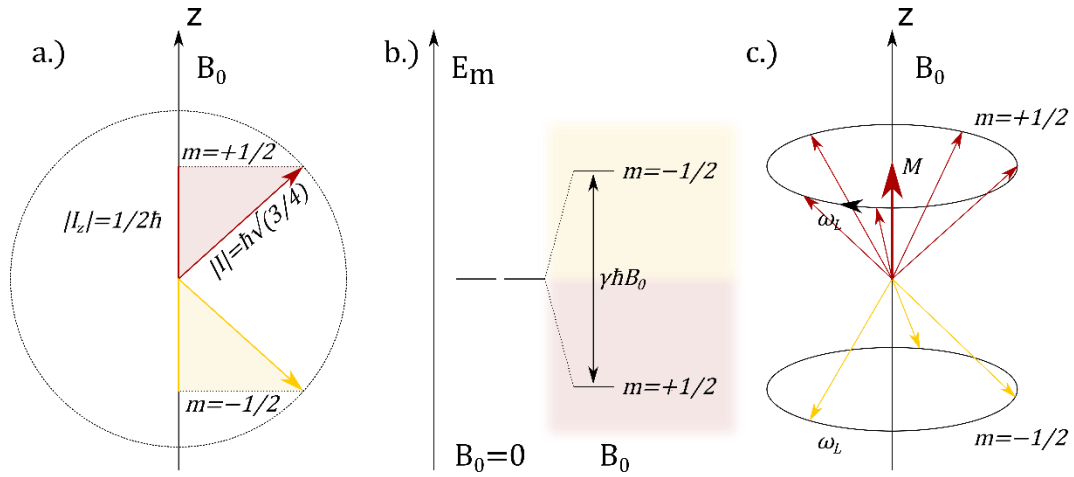


Figure 21: a.) Alignment of spins relative to an external magnetic field providing a quantization axis, b.) energetic splitting of the two spin orientations due to the Zeeman interaction, c.) Alignment and precession of magnetic moments in a magnetic field (Figure assumes $\gamma > 0$).^{100,101}

Because the Zeeman interaction is weak, the energetic splitting of the states, which are occupied according to Boltzmann statistics, is relatively small. Followingly, the occupancy of the parallel and antiparallel states is close to 1:1. To increase the energetic difference, strong magnetic fields with a magnetic flux density B_0 of several Tesla are used for NMR experiments.¹⁰⁰

Important for the use of NMR as a characterization method is that the environment of nuclei influence the resonance behavior by various interactions. For solid-state NMR, all the interaction can be described by the following Hamiltonian:¹⁰⁰

$$H_{\text{total}} = H_z + H_{\text{rf}} + H_{\text{ms}} + H_D + H_J + H_Q \quad (31)$$

With H_z being the Zeeman interaction itself, H_{rf} the interaction with the radio pulse applied during measurements, H_{ms} the magnetic interaction with the surrounding electrons (magnetic or chemical shielding), H_D and H_J the direct and indirect magnetic dipole-dipole interactions, H_Q the interactions between electric quadrupole moments in $I > 1/2$ systems (quadrupolar interaction).¹⁰⁰

During NMR experiments the equilibrium distribution of magnetic moments is disturbed by an external stimulus, namely a linearly polarized radio frequency (rf) pulse. Depending on the pulse strength and duration the individual magnetic moments, and consequently the macroscopic magnetization, can be altered. One of the standard pulses is the $\pi/2$ or 90° pulse, see Figure 22. If the rf pulse has a frequency equal or close to the Larmor frequency, resonance occurs, and the electromagnetic wave is absorbed by the spin system of the sample. Consequently, transitions, in the case of $I = 1/2$, from parallel to antiparallel occur, increasing the magnetic energy of the system. Additionally, after the pulse, there exists a phase correlation in the precession motion around the magnetic field, resulting in a transverse magnetization in the xy plane. This transverse magnetization results in no additional magnetic energy of the system. If the pulse length and power is adjusted in the right way, both parallel and anti-parallel states are equally occupied (vanishing longitudinal magnetization M_z) and the magnetization is completely tipped into the xy plane. When only considering the macroscopic magnetization M , this corresponds so a simple 90° rotation of M about the axis along which the sample was irradiated.⁹⁴

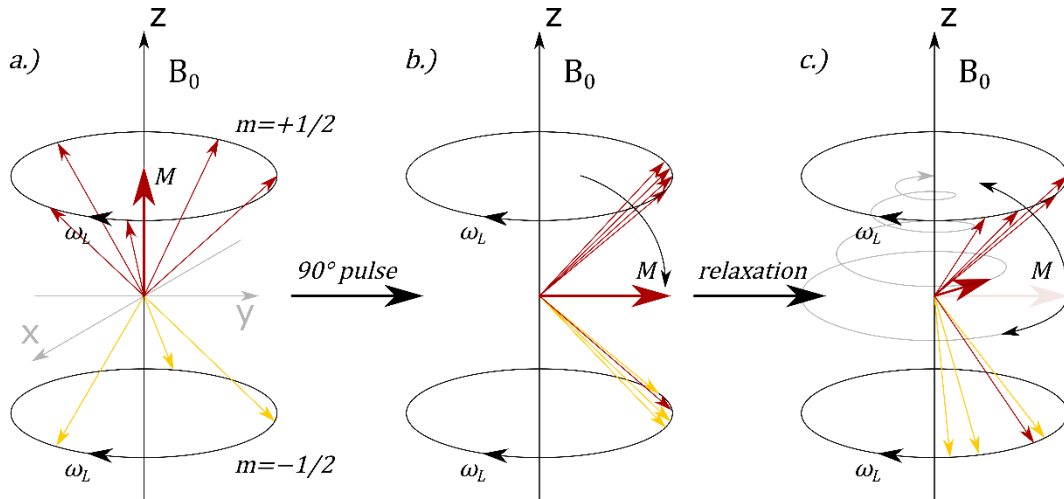


Figure 22: Illustration of a.) magnetic moments and macroscopic magnetization in equilibrium, b.) tilting of the magnetization in the xy plane (redistribution of magnetic moments and phase correlation) by 90° pulse, c.) spin-lattice (recovery of M_z) and spin-spin (dephasing) relaxation process of the magnetic moments.

Summing up, rf pulses with frequency ω_L result in the redistribution of magnetic moments and phase correlation of the precession, both of which decay with characteristic time constants T_1 and T_2 . These processes are called spin-lattice and spin-spin relaxation and determining these relaxation time constants is the main interest of (nuclear magnetic) relaxometry.⁹⁴

2.3.2 ^7Li NMR Spin-lattice relaxation

Spin-lattice relaxometry (SLR) allows probing the ion dynamics of materials. The difference between impedance and NMR techniques is that, generally speaking, impedance yields macroscopic and NMR microscopic information.⁹⁴

After application of a 90° pulse the sample is in an excited, non-equilibrium state and the system wants to re-establish thermal equilibrium of the spin system with the “thermal bath” of the lattice.⁹⁴ Followingly, the transverse magnetization decays and the longitudinal magnetization recovers. As already indicated by mentioning the thermal bath of the lattice, this process is related to energy exchange between the spin system and the lattice and is therefore called the spin-lattice relaxation.⁹⁸ The recovery of the equilibrium longitudinal magnetization M_z can be described as a function of time:⁹⁴

$$M_z(t) = M_0 \cdot \left(1 - e^{-\frac{t}{T_1}}\right) \quad (32)$$

With M_z being the longitudinal magnetization in z direction, M_0 the modulus of the magnetization, T_1 a time constant describing the relaxation and t the time. The quantity of interest in spin-lattice relaxometry is this spin-lattice relaxation time T_1 , which is a measure of the transition probability of the spins between distinct Zeeman levels. This time constant is accessible by means of certain pulse sequences, see Figure 23. In a first step closely spaced 90° pulses (saturation comb) are applied to reduce the longitudinal magnetization to zero. This pulse sequence does not result in any phase correlation of individual spins. During the relaxation delay t_{var} the sample recovers its longitudinal magnetization to achieve thermal equilibrium with the lattice. After this delay a single 90° pulse is applied, tipping the longitudinal magnetization in the xy plane and the FID (free induced decay) is recorded. The resulting signal is directly proportional to the recovered longitudinal magnetization. By varying t_{var} the recovery of M_z with time can be recorded and fitted using an exponential function, thereby obtaining T_1 .⁹⁴

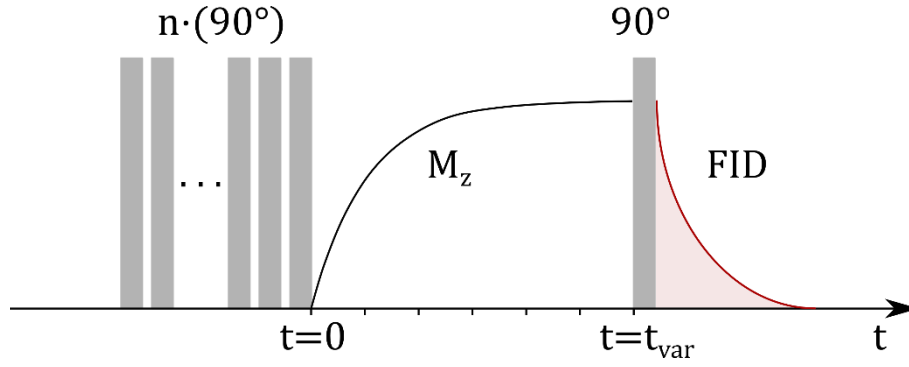


Figure 23: Pulse sequence of an T_1 NMR-SLR experiment. Inspired by Habasaki et al.⁹⁴.

Of great interest is the temperature-dependency of T_1 . Transitions between Zeeman levels can be induced by ionic jump processes in the crystal. Therefore, the temperature dependent ion dynamics of a sample directly influence T_1 . The transition probability ($1/T_1$) is highest when the correlation time of the atomic jump processes (equivalent to the residence time on a site), τ_c , equals the inverse of the Larmor frequency ω_L (or alternatively when the hopping rate $\tau_c^{-1} = \omega_L$). For useful signal-to-noise ratios in NMR, strong magnets (several Tesla) are needed and the Larmor frequency is direct proportional to the magnetic flux B_0 and therefore:⁹⁴

$$\tau_c^{-1} = \omega_L = \gamma \cdot B_0 \quad (33)$$

Consequently, since B_0 (ω_L) is on the orders of several Tesla (hundred MHz) in NMR, only very fast ionic motions on the order of 10^{-9} s can be characterized using T_1 .⁹⁴ Not that equation 33 is only valid if a maximum in the transition probability ($1/T_1$) is observed, see Figure 25.

To characterize slower ionic motional processes a second method, the spin-locking technique, illustrated in Figure 24, is available. In this technique a 90° pulse is applied, followed by a locking magnetic field, holding the transverse magnetization in the xy plane. This magnetic field B_1 is much smaller than B_0 . The magnetization along the y' ($'$ indicates a rotating coordinate system) axis relaxes towards equilibrium with a characteristic time constant $T_{1\rho}$. By varying the locking time t_{lock} and probing the residual magnetization along the y' -axis, the exponential relaxation can be determined and fitted, yielding the spin-locking relaxation time $T_{1\rho}$. Considering equation 33 and substituting the far weaker magnetic field B_1 for B_0 shows that, using this technique, much slower jump processes on the order of 10^{-5} s can be investigated.⁹⁴ Note that for spin-locking SLR in equation 33 an additional factor of 2 has to be included on the right side, see also Figure 25.

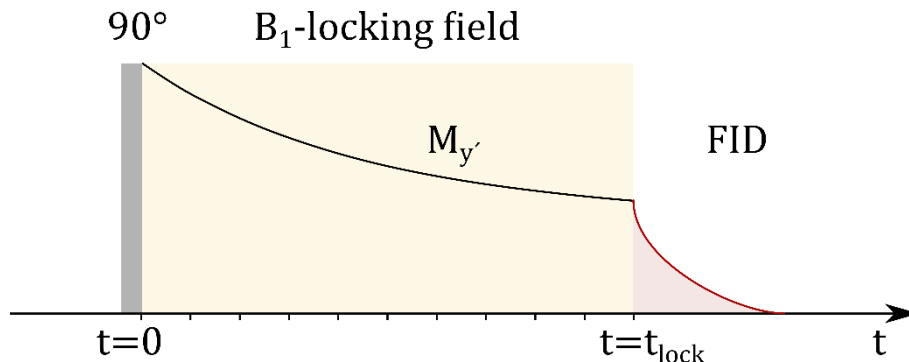


Figure 24: Pulse sequence of an $T_{1\rho}$ NMR-SLR experiment. Inspired by Habasaki et al.⁹⁴.

Atomic jump processes are thermally activated and the associated correlation time τ_c can be described using an Arrhenius equation:⁹⁴

$$\tau_c = \tau_{c,0} \cdot \exp\left(-\frac{E_a}{k_b T}\right) \quad (34)$$

With the preexponential factor $\tau_{c,0}$ being the attempt frequency, E_a the activation energy, k_b the Boltzmann constant and T the temperature. As τ_c changes, also T_1^{-1} and $T_{1\rho}^{-1}$ as probed by NMR-SLR do and the results can be plotted as a function of temperature in an Arrhenius plot, see Figure 25, yielding peaks at which $\tau_c^{-1} = \omega_L$. This allows the determination of the correlation time of atomic jump processes (i.e., the residence time) at the temperature of the peak. From the slopes at the sides of the peaks the activation energies of the atomic hopping processes can be calculated.⁹⁴

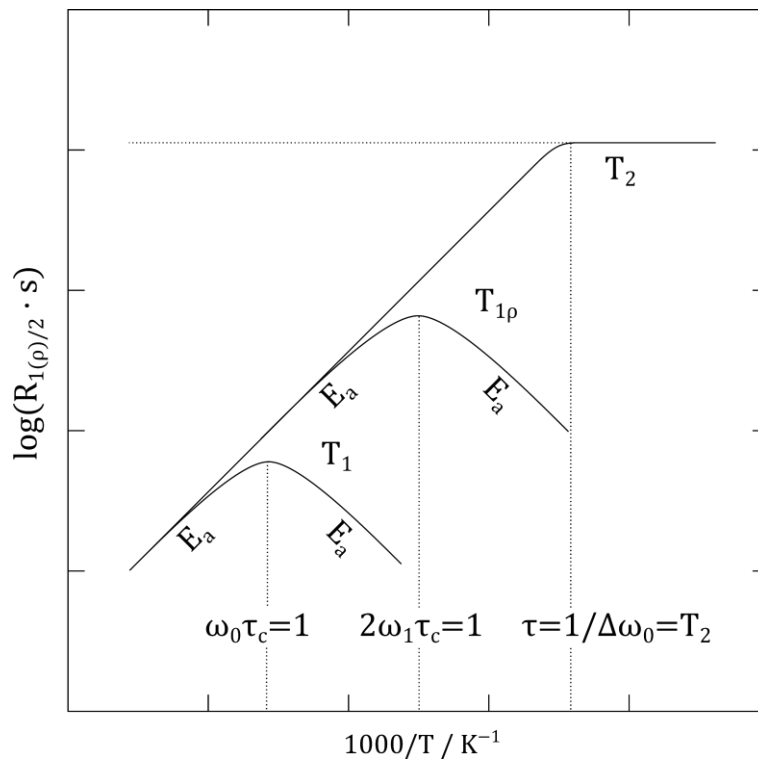


Figure 25: Illustration of an Arrhenius plot obtained by plotting the logarithm of the relaxation rate $\log(T_1^{-1}) = \log(R_1)$ against the inverse temperature. Inspired by Habasaki et al.⁹⁴

For the sake of completeness another relaxation phenomenon to note is the spin-spin relaxation. It describes the dephasing of the individual spins precessing with the Larmor frequency about the magnetic field. This dephasing originates from the local magnetic field differences between inequivalent sites occupied by nuclei, leading to slight variations in the precession frequencies and consequently dephasing.⁹⁸

From the correlation times obtained from spin-lattice and spin-spin relaxation the uncorrelated diffusion coefficient D_{uc} (3D diffusion) can be calculated using the Einstein-Smoluchowski relation:⁹⁸

$$D_{uc} = \frac{d^2}{6 \tau_c} \quad (35)$$

With τ_c being the correlation time obtained by NMR and d the length of the atomic jump.

2.3.3 Magic angle spinning (MAS) NMR

As described above, there are many different interactions of a spin with its environment, see equation 31.¹⁰⁰

Many of these interactions are anisotropic, i.e., dependent on the crystallite orientation relative to the external magnetic field. Since samples in solid-state NMR are commonly powders and consequently many different crystallite orientations are present, the resulting spectra contain broad lines which might overlap. Therefore, techniques to increase the resolution of solid-state NMR are necessary. One of the most prominent technique for solid-state NMR is magic-angle spinning.¹⁰²

The shift in frequency of the signal can be described by the following equation:¹⁰⁰

$$\omega(\theta, \varphi) - \omega_L = \omega_{\text{iso}} + \varepsilon \frac{1}{2} (3 \cos^2(\theta) - 1 - \eta \sin^2(\theta) \cos(2\varphi)) \quad (36)$$

With θ and φ describing the orientation of the crystallite in the magnetic field B_z , ε describing the strength of the anisotropic interaction and η the axial asymmetry.¹⁰⁰ The parameters ε and η are derived from a shielding tensor, describing the various shielding interactions in a principal axis system, see Figure 26 a.).^{100,103} The actual strength of the interaction is a function of the orientation of this shielding tensor in the external magnetic field B_z .¹⁰³

Neglecting the axial asymmetry term ($-\eta \sin^2(\theta) \cos(2\varphi)$) in equation 36, the only relevant term for the anisotropic interaction is $(3 \cos^2(\theta) - 1)$.

The geometry of a sample in an MAS NMR experiment is illustrated in Figure 26 c.). θ is the angle of the individual crystallite, and with it the shielding tensor, with the external magnetic field B_z . The sample in MAS is inclined at a certain angle θ_R to B_z and rotated round this axis. β is the angle between this inclined rotation axis and the crystallite orientation. Reverting to equation 36, the mean of the relevant term for the anisotropic interaction, $3 \cos^2(\theta) - 1$, can be given as a function of θ_R and β :¹⁰²

$$(3 \cos^2(\theta) - 1) = \frac{1}{2} (3 \cos^2(\theta_R) - 1)(3 \cos^2(\beta) - 1) \quad (37)$$

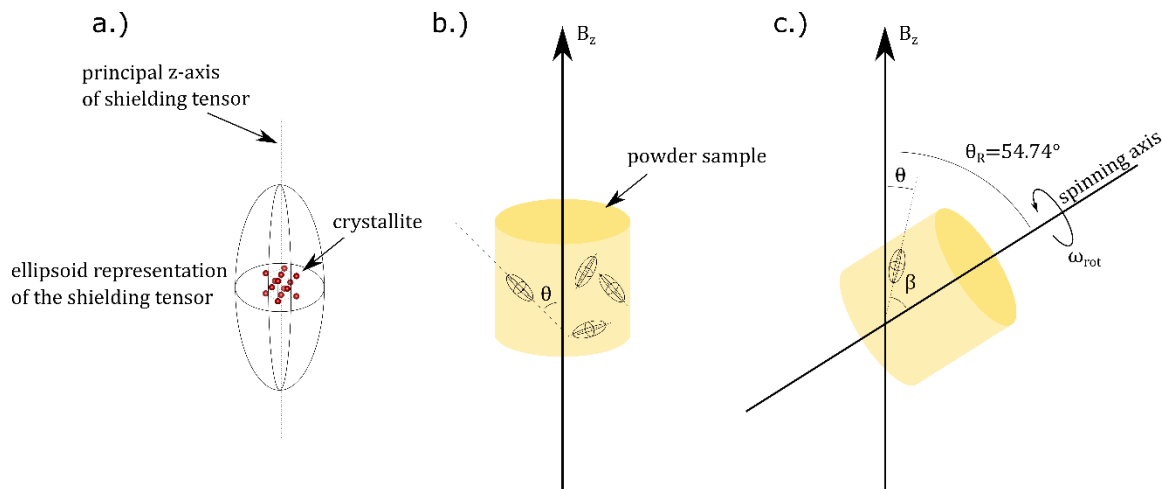


Figure 26: a.) Graphical representation of the shielding tensor, b.) powder sample with the shielding tensor of crystallites orientated in different directions and c.) averaging of the shielding tensor by magic angle spinning. Inspired by Duer¹⁰².

The crystallite orientation is fixed since the crystallite does not change orientation during the measurement and followingly θ and β are fixed too. Since most samples are a powder, the crystallites are orientated randomly in all directions and θ and β take all possible values. However, the angle θ_R can be controlled as it is related to the axis about which the sample is rotated. If θ_R is set to 54.74° the quantity $(3 \cos^2(\theta_R) - 1)$ and consequently $\langle 3 \cos^2(\theta) - 1 \rangle$ equals zero and according to equation 36 the anisotropic contribution to the line shift disappears. It is important to note that equation 37 is only valid if the sample rotates with high enough frequency so θ is averaged rapidly compared to the anisotropy of the interaction.¹⁰²

This is the case if the frequency of rotation is large compared to the frequency describing the spectral dispersion due to anisotropic interactions.¹⁰⁰

2.4 Raman spectroscopy

Raman spectroscopy is a method for probing most commonly vibrational states (rotational and electronic states are also possible however) of a sample. Followingly, together with IR spectroscopy it belongs to the vibrational spectroscopic methods.¹⁰⁴

Physical basis for Raman spectroscopy is the so-called Raman scattering. As a photon is scattered, the system under consideration is excited to a virtual energy level. During an elastic scattering event the energy associated with this virtual level is released in the form of a photon having the same energy as the incident photon. This is the conventional Rayleigh scattering. However, there is a small probability that the vibrational state of the system changes while it is in an excited state. Therefore, when the energy previously absorbed is released, the system will be in a higher (or lower) energetic state compared to the original ground state. This is associated with a smaller (or higher) energy quantum released as a photon. Consequently, the overall process is inelastic, and the outgoing photon will be shifted to lower (or higher) frequencies. This frequency shift is known as the Stokes (if to lower frequencies) or Anti-Stokes (if to higher frequencies) shift.¹⁰⁴

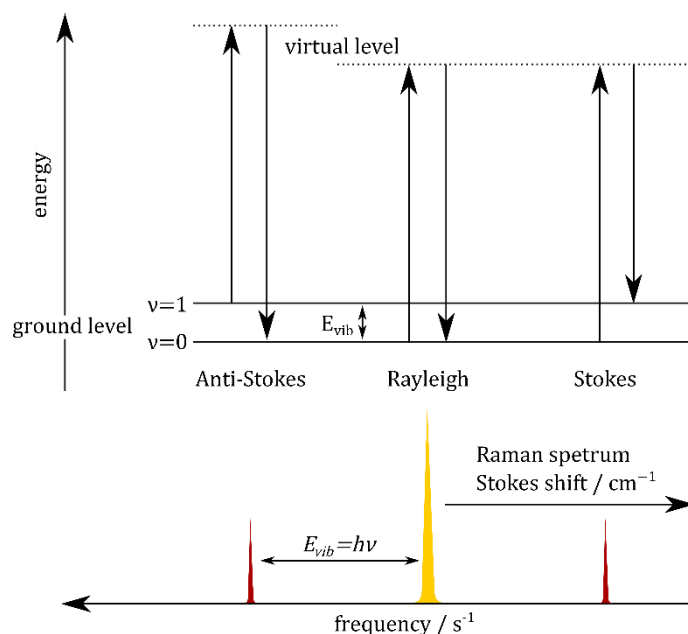


Figure 27: (top) Energy diagram of the vibrational and virtual states involved in Raman spectroscopy and (bottom) the corresponding peak in a spectrum. Inspired by Yang⁸⁸.

Since the shift corresponds to the energy of the vibrational levels, Raman spectroscopy, like IR spectroscopy, can be used as a method for probing the vibrational states of a sample. However, there is a distinct difference in the selection rules for Raman and IR spectroscopy. The selection rule for Raman spectroscopy is that only vibrational states leading to a change in polarizability are observable, while for IR a change in dipole moment is necessary.⁸⁸

Since the probability for Raman scattering is very low compared to Rayleigh scattering, the incident radiation must be very intense, resulting in the use of Lasers as light sources. The scattered light is then collected at a 90° angle relative to the incident Laser and Raman spectra conventionally plot intensity against the Stokes shift, not the absolute frequency, in cm^{-1} .¹⁰⁴ It should also be noted that normally only the Stokes shift is measured in Raman spectroscopy, since the Stokes shift is much more probable than the Anti-Stokes shift.⁸⁸

3 Experimental

3.1 Synthesis

$\text{Li}_{10}\text{GeP}_2\text{S}_{12}$ was synthesized using the conventional solid-state synthesis route that was originally reported by Kamaya et al. in 2011 and $\text{Li}_{10}\text{GeP}_2\text{S}_{12-x}\text{O}_x$ by a very similar solid-state route reported by Sun et al. in 2016.^{13,46} Stoichiometric amounts of the starting materials, Li_2S (Alfa Aesar 99.9 %), P_2S_5 (Sigma-Aldrich 99 %) and GeS_2 (abcr 99.99 %) for $\text{Li}_{10}\text{GeP}_2\text{S}_{12}$, and additionally Li_2O (Aldrich 97 %) for the oxygen substituted $\text{Li}_{10}\text{GeP}_2\text{S}_{12-x}\text{O}_x$, were weighted in (3 g total) and put into a ZrO_2 milling beaker (45 ml) together with 180 ZrO_2 balls ($\text{Ø}=5$ mm) for mechanical milling using a planetary ball mill (Fritsch Pulverisette 7 Premium line). Consequently, the powder was milled for 40 h at 380 rounds per minute (rpm) with alternating cycles of 15 min milling and 15 min pause to avoid extensive heating, summing up to a net milling time of 20 h. After the milling the compacted powder was scratched from the milling beaker using a ceramic Al_2O_3 rod. The obtained powder was compacted into pellets ($\text{Ø}=5$ mm, $t\approx 2$ mm) at loads of 0.5 t (62 MPa) using a Specac laboratory pellet press. The pellets were put into a quartz tube, which was followingly sealed by applying vacuum (≈ 0.01 MPa) and melting the quartz with a natural gas/ O_2 torch. Before the quartz tubes were filled and used, thorough cleaning with acetone, ethanol, and isopropanol in the ultrasonic bath for 10 min each was done, followed by drying for 24 h at 300 °C under dynamic vacuum. The quartz tubes before and after sealing are depicted in Figure 28. The sealed samples were annealed in a furnace (muffle furnace, Nabertherm) for 8 h or 24 h at 550 °C using a heating and cooling rate of 1 °C/min. The annealed pellets were grinded using mortar and pestle. The obtained powder was either directly used for analysis (XRD, Raman, NMR) or pressed again to pellets (impedance spectroscopy). All steps were performed in an Ar-filled glove box with H_2O and $\text{O}_2 < 0.1$ ppm.

For nanostructuring 0.8 g of LGPS powder were used and put into a ZrO_2 milling beaker together with 60 ZrO_2 balls ($\text{Ø}=5$ mm). After milling the powder was scratched from the milling beaker using a ceramic Al_2O_3 rod. The obtained powder was grinded using mortar and pestle and was either directly used for analysis (XRD, NMR) or pressed again to pellets (impedance spectroscopy). Again, all steps were performed in an Ar-filled glove box with H_2O and $\text{O}_2 < 0.1$ ppm.



Figure 28: Quartz tubes filled with pressed sample pellets a.) before sealing and b.) after sealing and annealing at 550 °C for 8 h.

3.2 X-ray powder diffraction

X-ray powder diffraction (XRD) was performed on the Rigaku MiniFlex with a 600 W Cu X-ray tube and a D/teX Ultra silicon strip detector. The samples were measured as powders in an air sensitive sample holder under the exclusion of air (loading of sample holder in Ar-filled glove box). The diffractometer was operated using the provided SmartLab Studio-II software. Additional XRD measurements were performed on a Rigaku SmartLab with a 3 kW sealed X-ray tube, CBO optics and a D/teX Ultra 250 silicon strip detector. For this equipment, the powder was filled in a glass capillary which was sealed using grease and parafilm. Only just before the measurement the seal was removed, and the capillary was put into the according sample holder (sealing the capillary again) in the diffractometer. The XRD data was evaluated using the X'Pert HighScore Plus software. Background fitting was performed, peaks were identified and compared with a personal crystallographic database containing LGPS, all educts, possible side phases (various Li-P-S and Li-Ge-S compounds) and possible oxidation products. The most relevant crystallographic (.cif) files were ICSD_188887 (Single-crystal X-ray structure analysis of the superionic conductor $\text{Li}_{10}\text{GeP}_2\text{S}_{12}$)⁴⁷ and ICSD_180319 (Crystal structure and phase transitions of the lithium ionic conductor Li_3PS_4)⁴¹.

The best candidates were further used for the structural evaluation using Rietveld refinement. In a first step zero shift and specimen displacement were refined for the patterns obtained by the Rigaku MiniFlex. For the Rigaku SmartLab this step was not necessary. Followingly, the scale factors, the unit cell parameters and the profile variables, U, V and W, (only two at a time) were separately refined using a semi-automatic mode. For the oxygen substituted variant the occupancy was altered based on literature values (sulfur replaced by oxygen) so that the calculated chemical formula agreed with the nominal chemical formula. The automatically calculated agreement index “Goodness of Fit” was used as an indicator for the fit quality.

XRD patterns were simulated based on reported crystallographic data using the software program VESTA.

3.3 Impedance spectroscopy

For the impedance measurements the powder was pressed into pellets ($\varnothing=5$ mm, $t\approx 1$ mm) at loads of 0.5 t (62 MPa) using a Specac laboratory pellet press in an Ar-filled glove box. Au electrodes of a thickness of 50 nm or 100 nm were applied using a Leica sputter coater also situated in an Ar-filled glove box. Impedance measurements in a frequency range of 10^{-2} Hz to 10 MHz were performed using a Novocontrol concept 80 broadband impedance spectrometer. The sputtered pellets were removed from the inert gas environment as short as possible (max. 5 min) while the specimen was mounted in the measurement cell, see Figure 29. The measurement cell was then lifted into the cryostat. Before the actual measurement, the temperature was increased to 373 K (100 °C) for at least 5 min to remove moisture from the sample surface. Additionally, a single sweep was performed before the measurement and temperature program was started to check if the sample was contacted right or if the sample had some critical defect. During the main measurement, the temperature was varied from min. 138 K (−135 °C) to max. 453 K (180 °C) by a constant flow of either heated or cooled nitrogen.

Some measurements were performed using air-tight sample holders (Brandstätter cell). In this case the sample was mounted into the air-tight sample holder inside the Ar-filled glove box and the whole sample holder was then mounted into the measurement cell in Figure 29. However, inductances at high frequencies hindered useful analysis of the data. Consequently, most measurements were done without the air-tight sample holder.

Equivalent circuit fitting was performed with the ZView® software package.

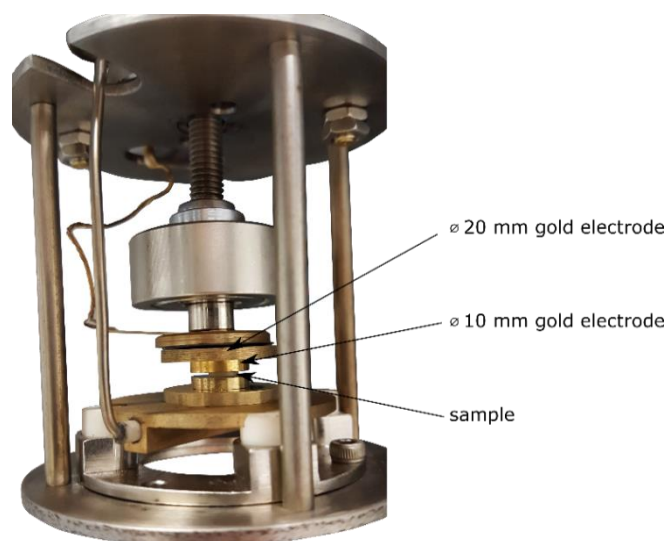


Figure 29: Measuring cell used for impedances spectroscopy with sample and Au electrodes.

3.4 Nuclear magnetic resonance

For the MAS NMR the specimen powder, thoroughly grinded, was filled into a 2.5 mm diameter ZrO₂ probe, which was closed off with a simple cap on one side and the rotor cap on the other. All steps were performed in an Ar-filled glove box with H₂O and O₂ < 0.1 ppm and after assembly the tube containing the sample was airtight. The MAS measurements were performed on the Bruker Avance III 500 MHz spectrometer. The spinning rate was 25 kHz. ³¹P, ⁶Li and ⁷Li measurements were performed and referenced to CaHPO₄ (Fluka, >97 %) and H₃COOLi·2H₂O (Sigma-Aldrich, ≥ 97 %) as a standard for ³¹P and ^{6,7}Li, respectively. For each measurement the pulse length, pulse power, reference phase and the O1 rf frequency shift were adjusted to obtain an optimal (FID) signal.

For the spin-lattice relaxation measurements the sample powder, thoroughly grinded, was filled into a Duran glass tube. Remaining space in the tube was filled with heat resistant wool. All steps were performed in an Ar-filled glove box with H₂O and O₂ < 0.1 ppm. Followingly, the tube was sealed by evacuating and melting off using a conventional burner. The measurements were performed on the Bruker Avance III 300 MHz spektrometer. Both T_1 and spin-lock $T_{1\rho}$ measurements were done for ⁷Li and ³¹P. For the former a standard saturation recovery sequence was used: $10 \times \pi/2 - t_{\text{var}} - \pi/2 - \text{acquisition}$. For each measurement the pulse length, pulse power, reference phase and the O1 rf frequency shift were adjusted. These parameters were adjusted for the T_1 measurement and adopted for $T_{1\rho}$. The recycle delay for the later was always set to $5 \cdot T_1$. For the spin-locking experiment a $\pi/2 - p_{\text{lock}} - \text{acquisition}$ sequence was used. The locking pulse length was set to 25 μ s, corresponding to a 20 kHz locking field in the xy plane, and only the locking pulse power was adjusted. If necessary, the list containing the t_{var} and t_{lock} values was changed to get a more complete picture of the magnetization transient. For construction of the magnetization transient the area under the modulus of the FID was utilized. The obtained magnetization transients were fitted and parameterized with stretched single and double exponential functions:

$$f(t) = A + B * \exp\left(-\left(\frac{t}{T}\right)^\gamma\right) \quad (38)$$

$$f(t) = A + \left(B_1 * \exp\left(-\left(\frac{t}{T_1}\right)^{\gamma_1}\right) + B_2\right) * \exp\left(-\left(\frac{t}{T_2}\right)^{\gamma_2}\right) \quad (39)$$

With A, B, B_1 and B_2 being fit parameters determining the height of the exponential function. γ, γ_1 and γ_2 are fit parameters and result in the stretching of the exponential function. T, T_1 and T_2 are the relaxation time constants important for further analysis and interpretation. t is time.

3.5 Raman

For Raman spectroscopy the sample powder was thoroughly grinded and filled into a glass capillary, which was then sealed using grease and parafilm. The same samples were used for the XRD at the Rigaku SmartLab and Raman spectroscopy. The measurement was performed on a Thermo Scientific™ DXR™ 2 Raman Microscope using a 532 nm Laser source and an Olympus objective (10 × magnification). The Laser spot size was set to 2.1 μ m, the Laser power to 5 mW and the exposure time to 2 s. 60 spectra were recorded for each measurement spot and summed up. The estimated resolution was between 5.5 cm⁻¹ and 8.3 cm⁻¹. Measurements at (at least) two spots on the sample were acquired. Each spectrum was taken in a range of 200 - 3500 cm⁻¹.

4 Results and discussion

4.1 $\text{Li}_{10}\text{GeP}_2\text{S}_{12}$

4.1.1 Powder X-ray diffraction

$\text{Li}_{10}\text{GeP}_2\text{S}_{12}$ was synthesized using the solid-state synthesis route similar to the originally reported one by Kamaya et al. in 2011.¹³ An XRD pattern measured after the starting materials were milled for 40 h at 380 rpm (20 h net milling time) showed only minor amounts of the starting material Li_2S , see Figure 30. No crystalline LGPS-related phase could be detected, indicating that the material at hand is amorphous. Therefore, it is assumed that either all the educts have become amorphous or have reacted and formed an amorphous precursor-LGPS phase. Such an amorphous precursor phase after mechanical milling was also reported in literature, with the milled powder containing small quantities of Li_2S detectable in XRD and TEM electron diffraction showing a halo pattern characteristic of amorphous materials.⁵⁰ However, the pronounced background in the XRD as seen in Figure 30 did not allow to observe broad bands that could possibly be associated with this amorphous phase.

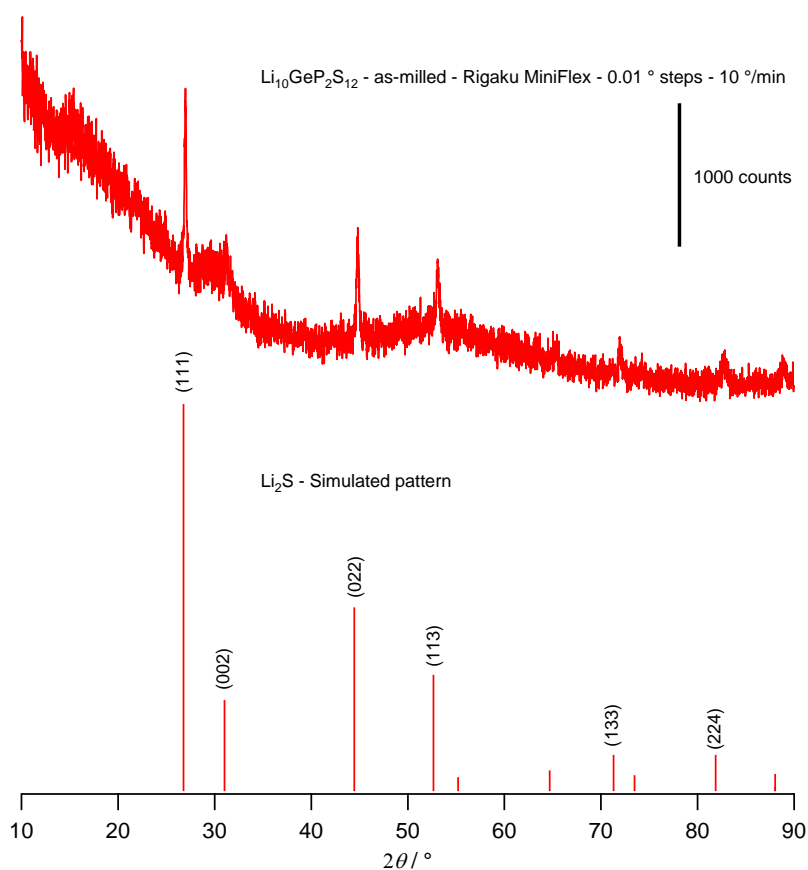


Figure 30: (top) XRD pattern of the powder obtained after ball milling for 40 h at 380 rpm recorded at the Rigaku MiniFlex with a step size of 0.01° and an acquisition speed of 10 °/min. (bottom) Simulated XRD pattern of Li_2S using the Vesta software package.

After milling the precursor powder was sealed in a quartz tube under vacuum and annealed at 550 °C for 8 h or 24 h. The resulting powders were characterized by XRD and the patterns could be clearly attributed to the tetragonal $\text{Li}_{10}\text{GeP}_2\text{S}_{12}$ phase with a space group of $P4_2/nmc$, see Figure 31.⁴⁷ No difference was observable between the samples annealed for 8 h and 24 h and both agreed very well with the simulated reference pattern for LGPS based on the single crystal data reported by Kuhn et al.⁴⁷. To allow for a more quantitative interpretation Rietveld refinement was performed and, using the mentioned single crystal data as the initial structural model⁴⁷, the 8 h and 24 h samples yielded a GOF of 2.90 and 2.98, respectively, see Appendix A. Minor peaks associated with the orthorhombic side phase were identified for both annealing times with about the same relative intensity. Consequently, since no improvement of crystallinity or side-phase content with increasing annealing time was observable, the annealing time for all further synthesis was fixed to 8 h.

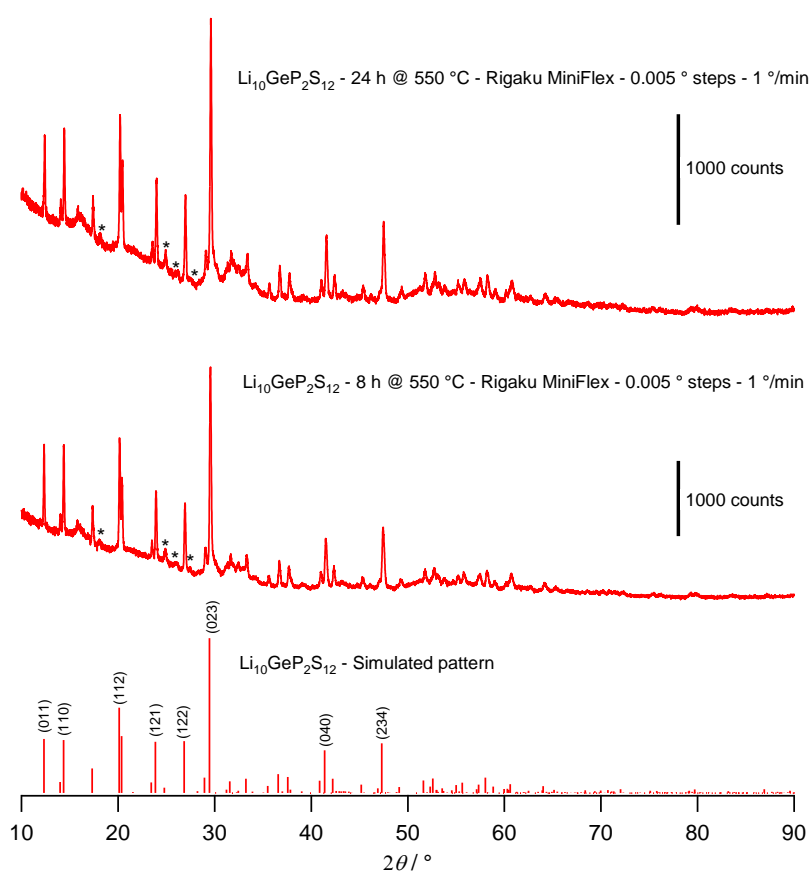


Figure 31: XRD pattern of the as-synthesized powder annealed for (top) 24 h and (middle) 8 h recorded at the Rigaku MiniFlex with a step size of 0.005° and an acquisition speed of 1 °/min. (bottom) XRD pattern of $\text{Li}_{10}\text{GeP}_2\text{S}_{12}$ simulated using the Vesta software package.

The XRD pattern of the LGPS specimen annealed for 8 h recorded at the Rigaku SmartLab showed improved background and allowed better and quantitative identification of the orthorhombic side phase $\beta\text{-Li}_3\text{PS}_4$, which was hardly identifiable in the patterns recorded with the Rigaku MiniFlex. This pattern was used for multi-phase Rietveld refinement in order to ascertain the presence of LGPS and to quantify the amount of orthorhombic side phase present in the sample. The Rietveld refinement yielded a Goodness of Fit value of 4.53 and the amount of $\beta\text{-Li}_3\text{PS}_4$ was found to be 10.5 %. A broad peak at around 15.8° could not be assigned to a specific phase, although it partially overlapped with a peak of the orthorhombic side phase. This peak was also present in a pattern of the oxygen substituted variant $\text{Li}_{10}\text{GeP}_2\text{S}_{11.7}\text{O}_{0.6}$ in literature, but was not assigned there either.⁴⁶

The GOF of this multi-phase refinement of the pattern recorded at the Rigaku SmartLab is worse compared to the single-phase refinements done for the patterns recorded with the Rigaku MiniFlex. However, the GOF value is not an absolute measure of fit quality and close inspection of the patterns in Figure 32 reveals that the multi-phase refinement of the SmartLab pattern shows good agreement with all major and minor reflexes of the pattern. All agreement indices for the Rietveld refinements performed are listed in Table 6.

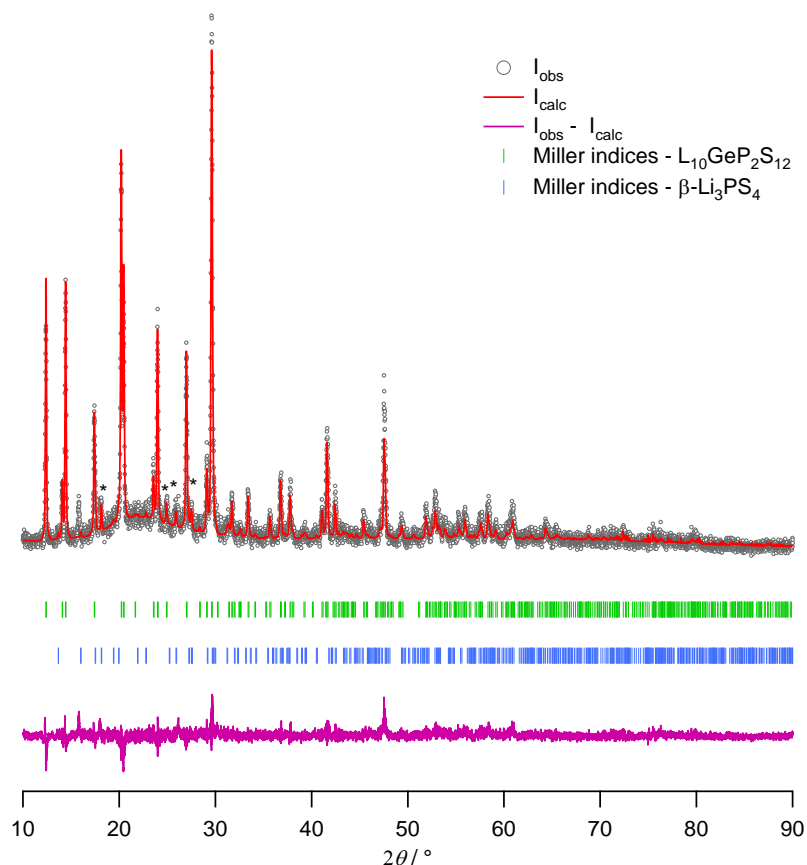


Figure 32: Rietveld refinement of the as-synthesized powder annealed for 8 h recorded at the Rigaku SmartLab with a step size of 0.01° and an acquisition speed of $2^\circ/\text{min}$. (top) Experimental and simulated pattern. (middle) Peak positions associated with $\text{Li}_{10}\text{GeP}_2\text{S}_{12}$ and $\beta\text{-Li}_3\text{PS}_4$. (bottom) Difference plot indicating error.

Table 6: Acquisition parameters and agreement indices obtained by Rietveld refinements.

Equipment - sample	Step size / $^\circ$	Speed / $^\circ \text{min}^{-1}$	R_{exp}	R_{wp}	GOF / χ^2
MiniFlex - 8 h @ 550 $^\circ\text{C}$	0.005	1	4.73	8.05	2.90
MiniFlex - 24 h @ 550 $^\circ\text{C}$	0.005	1	4.58	7.91	2.98
SmartLab - 8 h @ 550 $^\circ\text{C}$	0.01	2	9.28	19.74	4.52

Consequently, although the GOF indicates that further improvement of the structural model used for the refinement is possible, the presence of tetragonal $\text{Li}_{10}\text{GeP}_2\text{S}_{12}$ could be confirmed with high certainty, as could be the presence of about 10% of the orthorhombic side phase $\beta\text{-Li}_3\text{PS}_4$. More precise quantification of the side phase content was achieved by (^{31}P) MAS NMR.

4.1.2 MAS NMR

Further structural characterization was done by ^{31}P , ^6Li and ^7Li MAS NMR. The ^{31}P spectra showed three main lines at 94 ppm (19,021 MHz), 87 ppm (17,778 MHz) and 74 ppm (15,035 MHz), see Figure 33. Additionally, less intense lines were visible at 69 ppm (13,808 MHz) and 36 ppm (7,408 MHz). The peaks at 94 ppm and 74 ppm could be attributed to the tetragonal LGPS phase. The peak at 94 ppm corresponded to the $4d$ site occupied by both Ge and P in an 1:1 atomic ratio ($[(\text{Ge}_1\text{P}_1)\text{S}_4]^{3-}$), see Figure 33 inset left, and the peak at 74 ppm to the $2b$ site solely occupied by P ($[\text{PS}_4]^{3-}$), see Figure 33, inset right.^{55,59} The peak at 87 ppm can be attributed to $[\text{PS}_4]^{3-}$ units of the crystalline, orthorhombic phase $\beta\text{-Li}_3\text{PS}_4$ ^{59,105}. Additionally, self-synthesized $\beta\text{-Li}_3\text{PS}_4$ was characterized, the single line obtained coincided with the line at 87 ppm for the LGPS sample and the peak shape matched with literature, see Figure 34 a).¹⁰⁶ According to the occupancies of the $4d$ and $2b$ sites, the areas under the peaks at 94 ppm and 74 ppm must be equal⁵⁹, which matched the observed peak intensities, although the peak at 94 ppm tended to have a higher intensity in some of the samples. Followingly, the results matched very well the with above interpretation. The smaller peaks matched with oxygen-substituted $[\text{PS}_4]^{3-}$ units reported in literature, with 65 ppm being reported for $[\text{PS}_2\text{O}_2]^{3-}$, 34 ppm for $[\text{PO}_3\text{S}]^{3-}$ and 8 ppm for $[\text{PO}_4]^{3-}$, but with the last peak not observable in the experimental data.^{107,108} It should be noted that these values are reported for oxysulfide glasses ($60(0.6\text{Li}_2\text{S} \cdot 0.4\text{SiS}_2) \cdot 40\text{Li}_3\text{PO}_4$) and glass-ceramics ($70\text{Li}_2\text{S} \cdot (30-x)\text{P}_2\text{S}_5 \cdot x\text{P}_2\text{O}_5$) respectively.^{107,108} But similar peak positions have also been reported for the Si- and O-substituted LGPS variant $\text{Li}_{10}\text{SiP}_2\text{S}_{12-x}\text{O}_x$ with peaks at 67 ppm, 36 ppm and 9 ppm, assigned to $[\text{PS}_2\text{O}_2]^{3-}$, $[\text{PO}_3\text{S}]^{3-}$ and $[\text{PO}_4]^{3-}$ units, respectively.⁶¹ The Si-substitution should have no significant effect on peak positions. It is interesting to note that also some oxygen, possibly originating from impurities in the starting materials or from the environment during synthesis (ball milling), seemed to be present in LGPS without any intentional oxygen substitution.

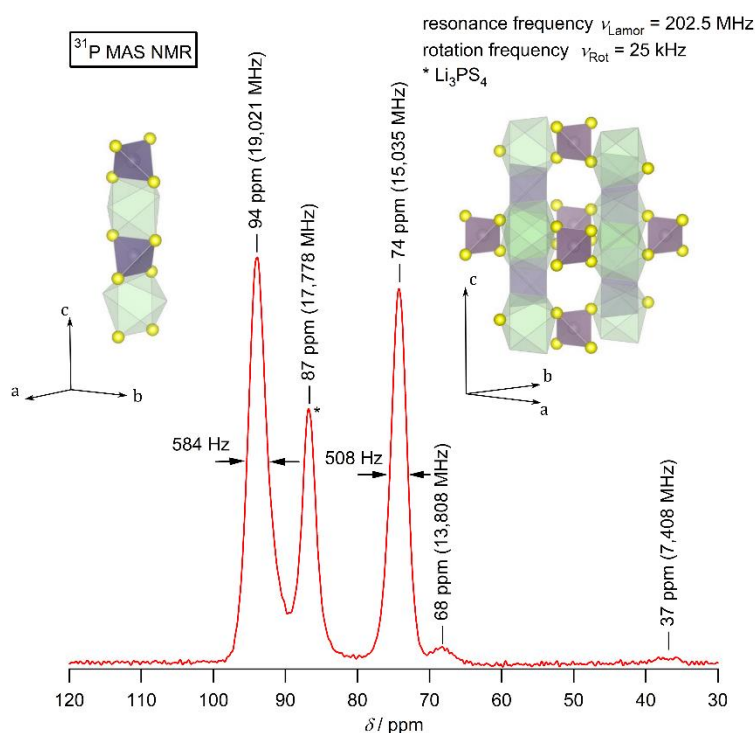


Figure 33: ^{31}P MAS NMR spectrum of a sample annealed 8 h @ 550 °C. Insets show the sites and associated coordination polyhedra associated with the peaks at 94 ppm (left inset) and 74 ppm (right inset). Other polyhedra are indicated, empty and slightly transparent.

The peaks in the ^{31}P MAS NMR spectrum were fitted with Voigt functions and the peak area was determined. Comparing the peak areas, considering the different P-contents of the tetragonal and orthorhombic phase, allowed the determination of the phase fractions in weight percent, $wt\%$, using the formula:

$$wt\%_a = \left(\frac{A_a}{A_{\text{tot}}} \cdot \frac{1}{x} \cdot MW_a \right) \cdot \left(\frac{1}{\sum_{i=1}^j \frac{A_i}{A_{\text{tot}}} \cdot \frac{1}{x} \cdot MW_i} \right) \quad (40)$$

With A_a being the summed-up area of all peaks associated with a certain phase a , A_{tot} the total area of all peaks (neglecting the smaller peaks at 67 ppm and 36 ppm), MW_a the molecular weight of the respective phase a , x a correction factor for including the different P-contents of the phases (equals P in the chemical formula of that phase, i.e., one for $\beta\text{-Li}_3\text{PS}_4$ and two for LGPS) and the right term is the same as the left term, but summing up over all phases j (being two in this case).

The phase fractions were determined and were 83.7(1) % for LGPS and 16.5(1) % for $\beta\text{-Li}_3\text{PS}_4$. The fraction of the orthorhombic side phase is about 57 % larger compared to the fraction obtained by Rietveld refinement. This could be because quantitative phase analysis by XRD is less precise, especially when considering the quantification of minor phases and if applied to a pattern with a high noise level and background, like in this case. It must also be noted that the content of orthorhombic phase calculated using above formula is the lower limit, since the P-content in $\beta\text{-Li}_3\text{PS}_4$ can be lower since P is partially substituted by Ge in $\beta\text{-Li}_3\text{PS}_4$, forming a solid solution, see Figure 5. Assuming the highest Ge-substitution possible at room temperature according to the phase diagram, roughly 10 %, and considering the reduced P-content of $\beta\text{-Li}_3\text{PS}_4$ in the calculation yielded phase fractions of 82.0(1) % and 18.0(1) %. This value could be regarded as an upper limit. Due to the above-mentioned shortcomings of XRD and the general superiority of NMR techniques with regard to quantitative analysis¹⁰⁰, the MAS NMR values will be considered more precise.

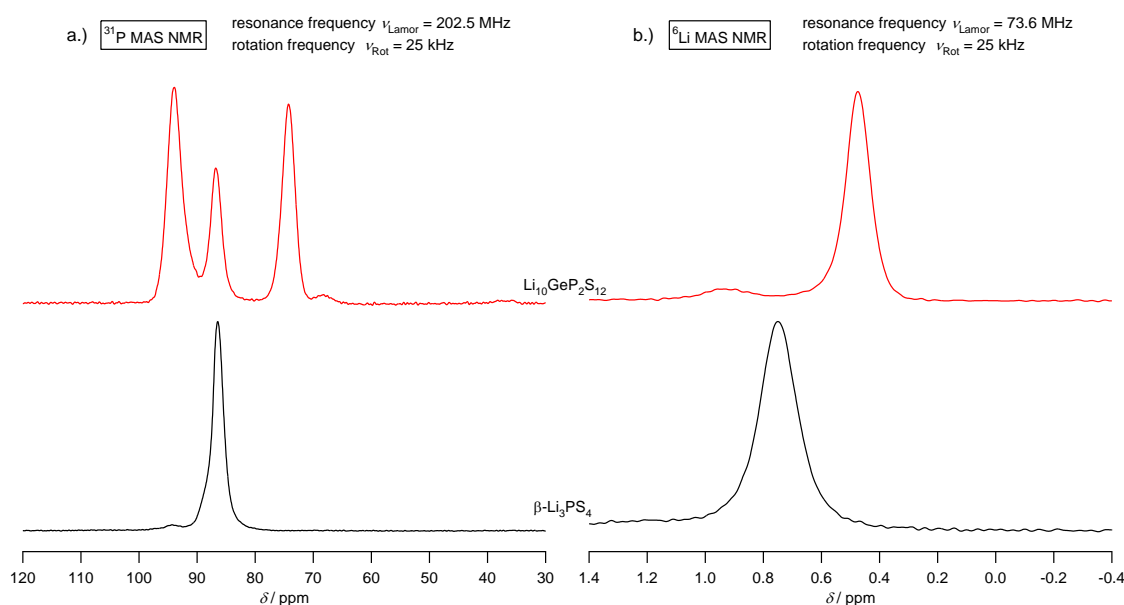


Figure 34: a.) ^{31}P and b.) ^6Li MAS NMR spectra. The upper spectra were recorded from an LGPS sample annealed 8 h @ 550 °C, the lower spectra from self-synthesized $\beta\text{-Li}_3\text{PS}_4$.

The ${}^6\text{Li}$ spectrum acquired for LGPS, see Figure 35, contained two peaks at 0.93 ppm (68.6 MHz) and 0.47 ppm (34.9 MHz). Fitting the peaks with Voigt functions yielded that the peaks contained 88 % and 12 % of the total peak area. The main peak at 0.47 ppm matched well with the literature data, but correction was necessary since different standards were used. In literature the peak was at 1.76 ppm and referenced against solid LiCl.¹⁰⁹ Here, solid LiCl was measured with ${}^6\text{Li}$ MAS NMR and referenced against $\text{H}_3\text{COOLi}\cdot 2\text{H}_2\text{O}$ (same as LGPS). A single peak at -1.24 ppm was obtained. Followingly, the peak was referenced indirectly to solid LiCl and was situated at 1.71 ppm, matching well with the literature data.¹⁰⁹

Striking is the extremely low fwhm of the line at 0.47 ppm of only 7.15 Hz. This already indicated very fast Li-ion motional processes in the sample at room temperature as would be expected by an electrolyte as conductive as LGPS.¹¹⁰ The peak at 0.93 ppm could not be attributed to the orthorhombic side phase, since the measured ${}^6\text{Li}$ MAS NMR spectrum of $\beta\text{-Li}_3\text{PS}_4$ did not coincide with the peak at 0.93 ppm, see Figure 34 b.). Other possibilities would be that the peak corresponded to another side phase not detected yet or to certain Li sites that do not take part in rapid Li-ion diffusion at room temperature. Comparing the peak areas with the current crystallographic models, the most likely site would be Li4 site (Wyckoff site: $4c$), containing about 12 % to 16 % (depending on the exact crystallographic model) of the Li ions. It should be noted that it is still not completely known if the Li2, the Li4, or both sites take part in the conduction process in the ab plane and different interpretations and suggestions exist in literature, see 1.3.4 Ionic conduction mechanism. Additionally, regarding the individual Li sites and their occupancies, the structural model for LGPS is not mature yet. Two-dimensional NMR experiments would be required to be evaluated if the peak at 0.93 ppm originates from the same phase as the peak at 0.47 ppm.

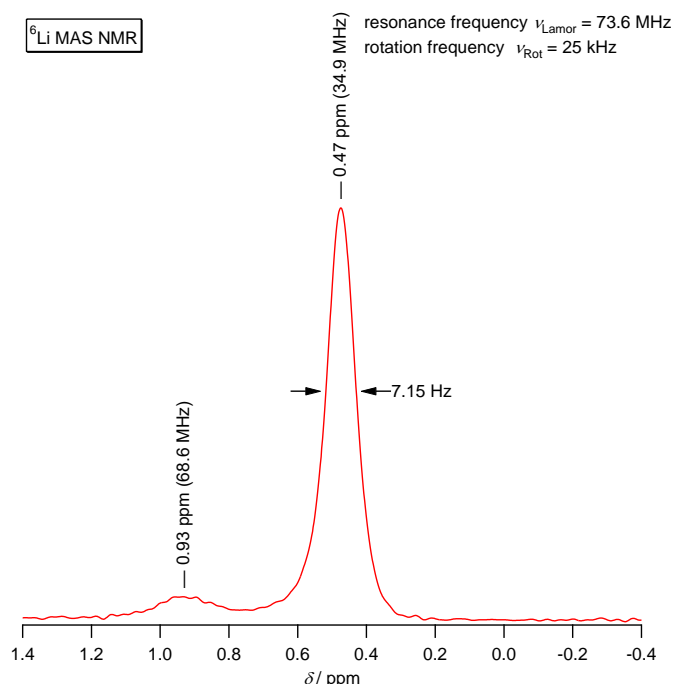


Figure 35: ${}^6\text{Li}$ MAS NMR spectrum of a sample annealed 8 h @ 550 °C. Referenced against $\text{H}_3\text{COOLi}\cdot 2\text{H}_2\text{O}$.

${}^7\text{Li}$ MAS NMR spectra contained two sharp peaks on top of a very broad peak, see appendix. The peaks were fitted, and the peak areas were compared. However, fitting of the broad peak was linked to large uncertainties and no useful interpretation could be found. Consequently, the ${}^7\text{Li}$ MAS NMR spectra were discarded.

4.1.3 Ionic conductivity and ion dynamics

The conductivity of LGPS was measured using impedance spectroscopy. A temperature program with a maximum temperature of 180 °C and a minimum temperature of –135 °C was used and the measurements were performed in 20 °C steps, see Figure 36.

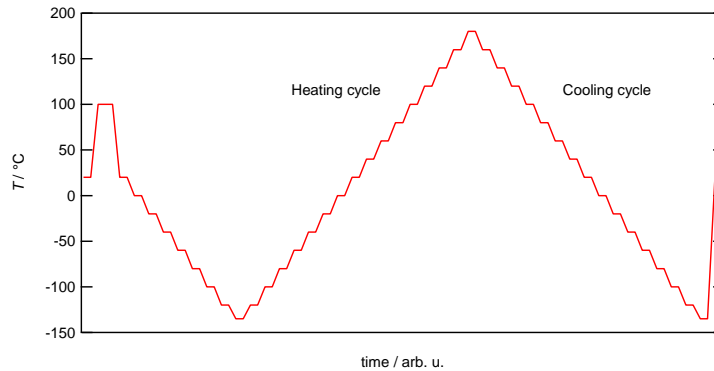


Figure 36: Temperature program run for the impedance measurements with a maximum temperature of 180 °C and a minimum temperature of –100 °C or –135 °C.

The conductivity spectrum of LGPS annealed 8 h at 550 °C is seen in Figure 37 a.). Each color represents a series of measurements at a specific temperature (isotherm). In the low frequency region of the isotherms the electrode polarization is clearly visible, with the monotonic decline in conductivity with decreasing frequency starting at a certain onset frequency, which shifts to higher frequencies as temperature is increased.¹¹¹ At intermediate to high frequencies, there are two distinct plateaus, with the one at high frequencies only observable at low temperatures. The different regions in the plot are highlighted in the in Figure 37 b.), with the electrode polarization at low frequencies being marked yellow, the plateau at intermediate frequencies red and the plateau at high frequencies and low temperatures blue. From these plateaus, the dc ionic conductivity could be directly read off. However, in a first step, the plateaus must be assigned to distinct regions of the sample, which all contribute to the total macroscopic response of the sample.

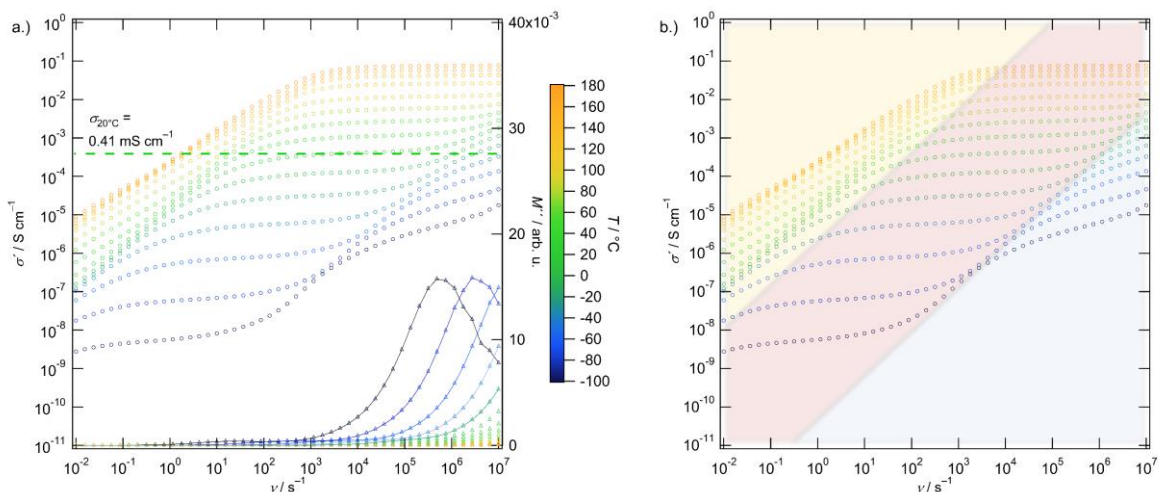


Figure 37: a.) Conductivity spectrum of $\text{Li}_{10}\text{GeP}_2\text{S}_{12}$ in a frequency range of 10^{-2} to 10^7 Hz and a temperature range of -100 °C to 180 °C. The imaginary part of the electric modulus M'' as a function of frequency is also plotted (linear scale). The horizontal line indicates the room temperature dc conductivity of the sample. b.) Same conductivity spectrum highlighting the electrode polarization regime (yellow) and the two observable plateaus (red, blue).

To assign the individual plateaus to distinct processes in the sample the electric modulus formalism was used. As previously described in the methods section the electric modulus is defined as:⁹⁴

$$M^* = i\omega C_0 Z \quad (21)$$

Due to this definition the imaginary part of the electric modulus M'' is equal to $\varepsilon_0/2C$ at its maximum value.⁹⁹ Followingly, the electric modulus is particularly sensitive to processes associated with a small capacitance, i.e., bulk processes.⁹⁹ Plotting additionally to the isotherms the imaginary part of the modulus M'' , see Figure 37 a.), resulted in a single peak at the position of the higher frequency plateau. This indicated that the plateau at higher frequencies is associated with the bulk response of the sample. Consequently, the plateau at higher frequencies (blue in Figure 37 b.) was attributed to the bulk and the plateau at lower frequencies (preliminary) to the grain boundaries (red in Figure 37 b.).

The results plotted in Figure 37 were obtained from a sample with comparable poor conductivity ($\sigma_{20^\circ\text{C}} = 0.41 \text{ mS cm}^{-1}$), associated mainly with the (presumed) grain boundary contribution (low conductivity at the g.b. plateau/ plateau at intermediate frequencies). This facilitated the discrimination of the g.b. and the bulk plateaus in the conductivity spectrum in Figure 37 since they could be distinguished better. The conductivity spectrum of a pristine sample with a relatively high conductivity of 3.89 mS cm^{-1} is depicted in Figure 38, showing about an order of magnitude better room temperature conductivity. The room temperature ionic conductivity matched well with literature as cold-pressed samples typically exhibit conductivities on the order of mS cm^{-1} (as in this case) and sintered samples on the order of 10 mS cm^{-1} .^{45,49} The isotherms of this sample exhibited less obvious individual plateaus since the respective conductivities were very similar. However, the imaginary modulus M'' again clearly indicated the bulk plateau at high frequencies.

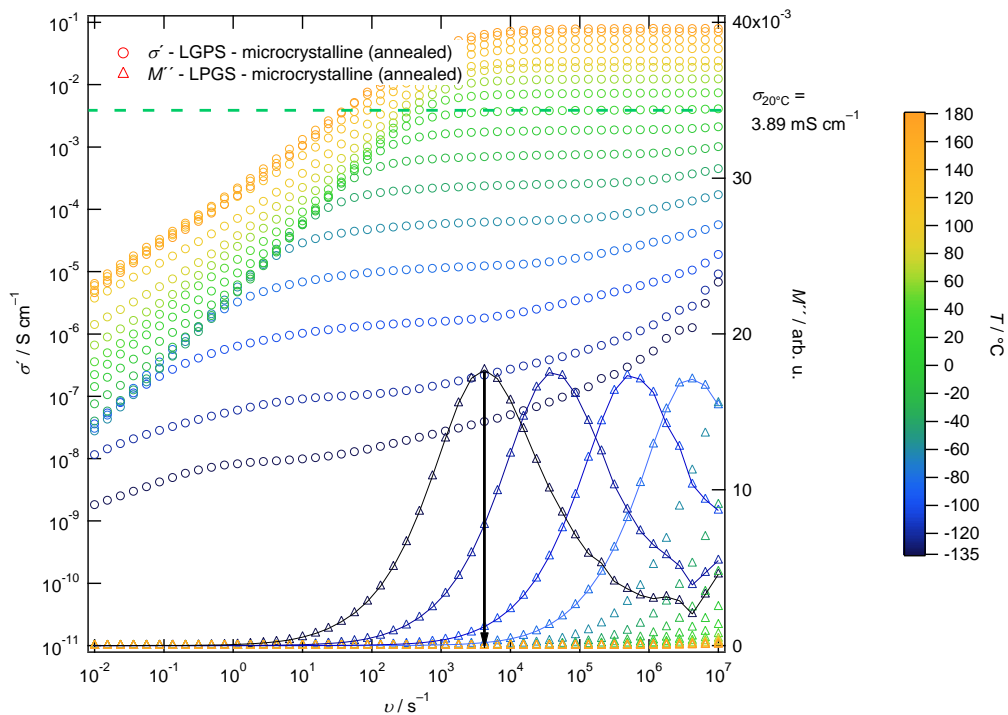


Figure 38: Conductivity spectrum of the best performing (pristine) $\text{Li}_{10}\text{GeP}_2\text{S}_{12}$ sample in a frequency range of 10^{-2} to 10^7 Hz and a temperature range of -135 °C to 180 °C. Additionally to the conductivity isotherms the imaginary modulus M'' is plotted (linear scale) as a function of frequency. The position of the peak maximum at -135 °C is highlighted with a black arrow.

The experimental data of this pristine sample at a temperature of $-135\text{ }^{\circ}\text{C}$ was plotted as a Nyquist plot, see Figure 39. Two semicircles were visible, although not completely resolved, followed by a monotonic and steep rise in Z'' , indicating the electrode polarization at low frequencies. The impedance was fitted using the equivalent circuit depicted in Figure 39. Table 7 summarizes the values assigned to the individual circuit elements during fitting. The capacitances of the individual RC elements, $1.8 \times 10^{-11}\text{ F}$, $4.1 \times 10^{-10}\text{ F}$ and $2.2 \times 10^{-8}\text{ F}$ were in line with the expected magnitudes for bulk (10^{-12} F), grain boundary ($10^{-11} - 10^{-8}\text{ F}$) and electrode ($10^{-7} - 10^{-5}\text{ F}$) contributions (see also Table 5). Therefore the respective semicircles were assigned to the bulk and g.b. regions of the sample, with the capacitance of the bulk process being however relatively high.⁹⁹ This interpretation matched with the assignment of the plateaus in the conductivity spectra. The capacitances for bulk and grain boundaries reported in literature for LGPS and related materials are in the range of $35\text{-}50\text{ pF cm}^{-2}$ and $0.1\text{-}10\text{ nF cm}^{-2}$, respectively.³⁸ The values obtained for this fit were 92 pF cm^{-2} and 2.1 nF cm^{-2} . While the value for grain boundaries was in line with the expected value, the capacitance associated with the bulk is double the value expected. One reason for this could be that there is considerable amount of secondary phase ($\approx 16\%$ $\beta\text{-Li}_3\text{PS}_4$) present and associated with such side phases are normally capacitances on the order of 10^{-11} F .⁹⁹ No distinct response of this minor side phase was observable, but if such a response is overlaid with the bulk response, this could explain a comparable higher capacitance. The $\beta\text{-Li}_3\text{PS}_4$ side phase was also reported in literature to be present in LGPS samples, but its influence on the conductivity and the capacitance was not investigated so far. It is not clear if the above-mentioned capacitance values already include the effect a minor secondary phase being present. Nevertheless, an interpretation as bulk contribution is still the best option, with the magnitude of the capacitance been closest to bulk capacitances. Although the two semicircles are strongly indicated, they are not completely resolved in the Nyquist plot. The reason for this is that the difference in the relaxation time constant τ ($\omega\tau = 1$ at semicircle apex) of the bulk and the grain boundary contributions is less than two order of magnitude, resulting in significant distortion of the ideal semicircles.⁹⁵ Lower capacitances of the grain boundary contribution are normally found in poorly sintered samples, having larger intergranular regions and imperfect contacting, as is the case for these samples, prepared solely by cold pressing.^{99,112} The pressed pellets had a weight of roughly 0.035 g , a diameter of 0.5 mm and a thickness of about $1.0\text{-}1.1\text{ mm}$. The resulting relative density is 83% , backing the argument of imperfect compaction.

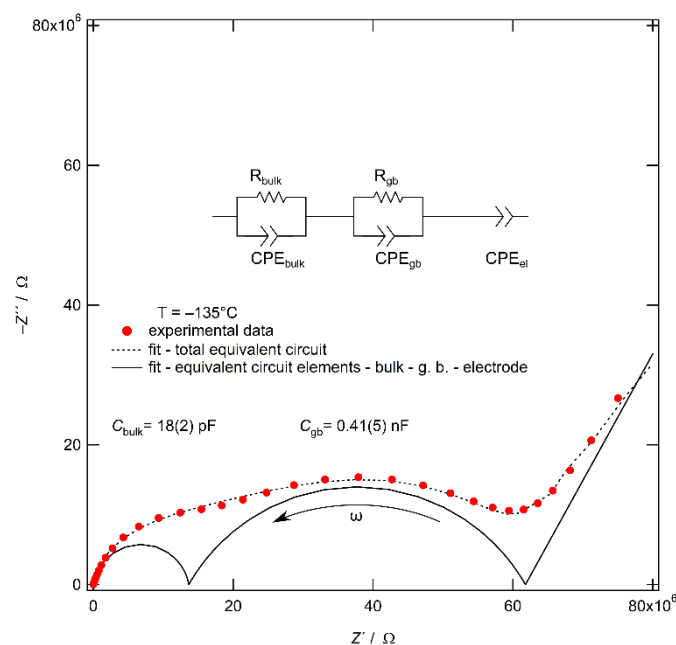


Figure 39: Nyquist plot of the pristine LGPS sample at $-135\text{ }^{\circ}\text{C}$. The experimental data was fitted using the depicted equivalent circuit and the results are plotted for the total circuit and the individual elements.

Table 7: Fit results for the equivalent circuit elements depicted in Figure 39. R is resistance associated with the resistor circuit element, C the capacitance of the constant phase element (CPE), n the exponent of the CPE and τ is the relaxation time constant.

Contribution	R / Ω	CPE - C / F	CPE - $n / \text{unitless}$	τ / s
Bulk	1.4×10^7	1.8×10^{-11}	0.89	2.5×10^{-4}
Grain boundary	4.8×10^7	4.1×10^{-10}	0.67	2.0×10^{-2}
Electrode	-	2.2×10^{-8}	0.68	-

Another argument for the assignment of the lower frequency plateau to the grain boundaries is that the conductivity at the plateau at lower frequencies varied quite strongly between samples of same composition and synthesis route. An explanation for this might be issues regarding the reproducibility of pressing the pellets used for impedance spectroscopy. Although all pellets have the same dimensions (thickness: ± 0.1 mm) and are pressed using the same pressing set and pressure, defects occur quite easily, and the compaction might not always be ideal. Such defects can lead to an increased resistivity in the low frequency regime, but will have little to no impact on the high frequency bulk response.¹¹³ Other explanations would be inhomogeneities in the microstructure leading to various effects influencing the response of the sample.¹¹⁴ Followingly, a spread in conductivity values is to be expected for plateaus associated with non-bulk processes. Because of the pressure applied during the impedance measurement, the elevated temperatures, and the easy deformability of sulfides^{21,63} (low elastic modulus) compaction or potentially sintering (homologous $T_H \approx 0.55$ at 180 °C) could be induced during the heating cycle. Therefore, an improved conductivity during the cooling cycle (see Figure 36) would be expected and was observed, especially for samples showing a high initial resistivity (higher potential for densification and compaction). This behavior is clearly visible in Figure 40, showing the isotherms at -100 °C of the best performing LGPS sample (8h at 550 °C) and a sample heated twice to 180 °C (i.e., two heating and cooling cycles, see Appendix 8.3). While the conductivities at frequencies below 10^3 Hz vary considerably, the isotherms join at higher frequencies to a single line, coinciding with the maximum of the electric modulus.

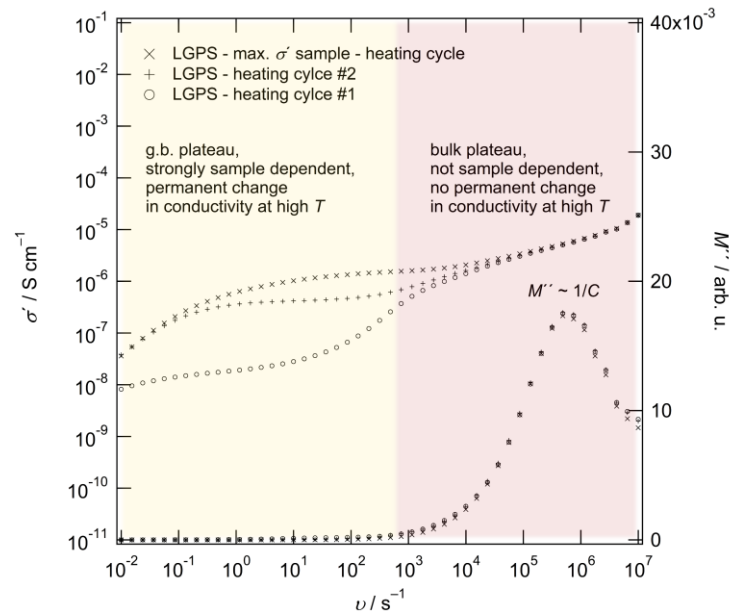


Figure 40: Isotherms (-100 °C) of a pristine (best conductivity) LGPS sample and a LGPS sample heated twice to 180 °C (see Appendix 8.3 for temperature program). The data plotted were taken from the heating cycles. Additionally, the imaginary part of the electric modulus M'' is plotted.

No significant difference between the heating ($-135\text{ }^{\circ}\text{C}$ to $180\text{ }^{\circ}\text{C}$) and the cooling cycle ($180\text{ }^{\circ}\text{C}$ to $-135\text{ }^{\circ}\text{C}$) was observed for the bulk plateau, indicating that there is no irreversible phase change or degradation at elevated temperatures. This could also be confirmed by an impedance measurement with two heating cycles, which showed no signs of irreversible changes (see Appendix 8.3 for corresponding figure). As previously discussed, only the conductivity associated with the grain boundary plateau is enhanced slightly, indicating better conductivity across the grain boundaries either due to densification, sintering or healing of defects accumulated at the grain boundaries. Interestingly, a sample annealed for 5 h at $200\text{ }^{\circ}\text{C}$ showed no significant increase in conductivity compared to the other specimens, indicating that the (small) pressure applied during the impedance measurement is an important factor. Sintering temperatures without pressure application for impedance samples are normally in the range of 500 to $550\text{ }^{\circ}\text{C}$.^{13,53}

The ionic conductivity of the sample made by the synthesis route with the 24 h annealing step at $550\text{ }^{\circ}\text{C}$ (instead of 8 h) was also measured. No significant improvement of the conductivity was observed for the sample annealed for 24h instead of 8 h. The conductivity at room temperature read out from the conductivity spectrum is 0.99 mS cm^{-1} , see Figure 41. Taking into account the spread of the conductivity due to the variation of the grain boundary contribution, this value was not significantly better or worse compared to the samples annealed for 8 h, which showed conductivities of 0.41 mS cm^{-1} and 3.89 mS cm^{-1} . The bulk conductivities of both 8 h and 24 h annealed samples roughly matched too, although there were some slight differences, probably due to a different (air-tight) sample holder being used for the measurement of the 24 h annealed sample.

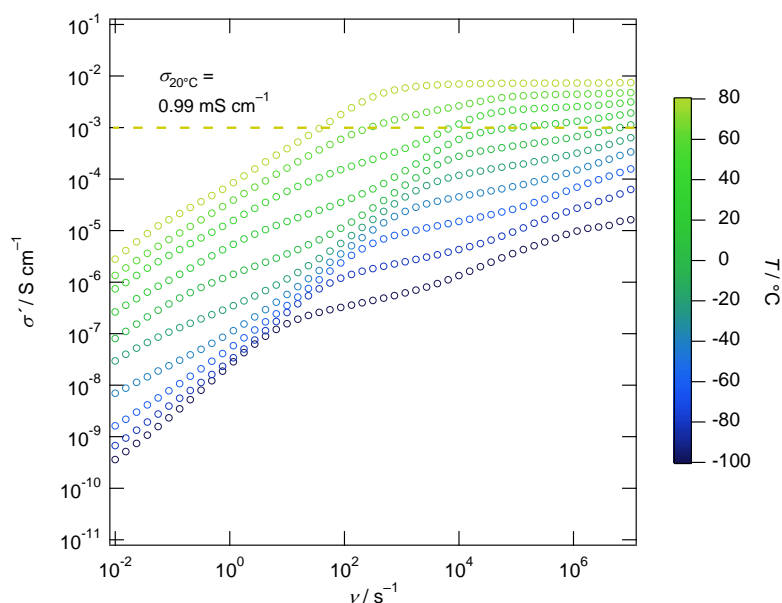


Figure 41: Conductivity spectrum of $\text{Li}_{10}\text{GeP}_2\text{S}_{12}$ annealed for 24 h @ $550\text{ }^{\circ}\text{C}$ in a frequency range of 10^{-2} to 10^7 Hz and a temperature range of $-100\text{ }^{\circ}\text{C}$ to $80\text{ }^{\circ}\text{C}$. Measured with air-tight sample holder.

It is important to note that besides the bulk and g.b. plateaus already identified, there was a third plateau, situated between the grain boundary plateau and the electrode polarization, which was removed by elevated temperatures. All samples that were measured without air-tight sample holder were dried before starting the actual measurement by applying a heating step at $100\text{ }^{\circ}\text{C}$ for 5 min, see Figure 36. This step removed this plateau, and it was only visible either before this drying step or during the heating cycle for samples measured with air-tight sample holders, not requiring any drying step.

Figure 42 plots conductivity data at 20 °C from LGPS synthesized by a.) 8 h and b.) 24 h heat treatment before any annealing of the impedance sample (either due to the drying step or the regular temperature program) in the measurement cell. The plateau is visible as a depression in the red marked frequency range before any heating and vanished completely after heating. In the Nyquist plot insets in Figure 42 no distinct semicircle is visible, but a broad bump that directly crosses over into the slope of the electrode polarization. Since no distinct semicircles were observable, no fitting using an equivalent circuit was attempted, but the capacity was estimated from the capacitance values directly obtained from the impedance equipment. The capacitances obtained were on the order of 10^{-7} Hz for both the 8 h and 24 h annealed samples. Followingly, the associated process could be related to surface layers or the sample-electrode-interface. Origin of this could for instance be that the contact of the as-sputtered Au-layer and the sample is imperfect and heals at elevated temperatures. Nonetheless, this plateau will be treated as an artifact.

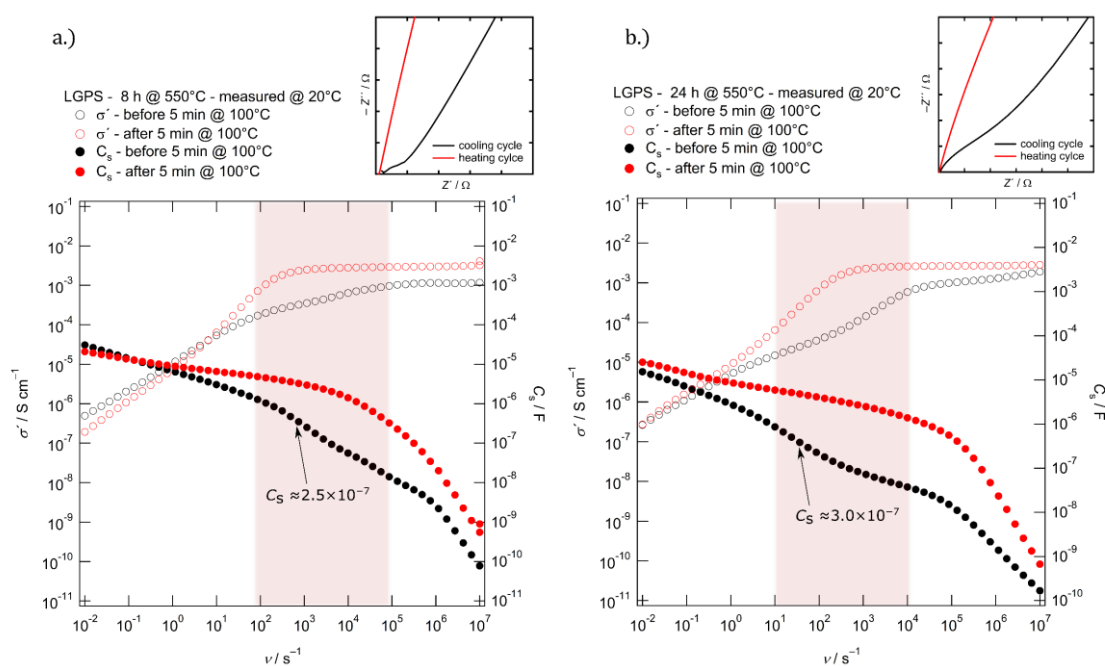


Figure 42: Isotherms at 20 °C for conductivity σ' and capacitance C_s of $\text{Li}_{10}\text{GeP}_2\text{S}_{12}$ annealed for a.) 8 h and b.) 24 h at 550 °C in a frequency range of 10^{-2} to 10^7 Hz before and after heating the sample at elevated temperatures. Inset at the top show the corresponding Nyquist plots.

Using the data of the pristine (highest conductivity) LGPS sample, an Arrhenius plot was constructed, see Figure 44. The conductivity σ_{DC} was directly read off from the plateaus of the isotherms in the conductivity spectrum. The as obtained σ_{DC} values from the isotherms are indicated in the conductivity spectrum in Figure 43, indicating the shift of the plateaus to higher frequencies as temperature increases with the bulk plateaus shifting so frequencies not observable. For lower temperatures Nyquist plots were constructed and fitted using equivalent circuits, for example as depicted in Figure 39. Both the grain boundary and bulk contributions to conductivity showed Arrhenius type behavior, however, the bulk contribution could only be separated from the total response at temperatures ≤ -80 °C. The values and consequently activation energies obtained directly from the isotherms matched very well with the ones obtained from fitting the Nyquist plots. Additionally, above -20 °C the slope of the curve and consequently the activation energy changed. Therefore, the plot was separated into a high ($T > -20$ °C) and a low temperature ($T \leq -20$ °C) regime. Fitting the data in both regimes linearly yielded similar activation energies E_a of 0.31(1) eV for both grain boundaries and bulk at lower temperatures, and a lower activation energy E_a' of 0.25(1) eV for the grain boundary / total response at higher temperatures.

Literature values for conductivities and activation energies are tabulated together with the results in Table 8. For a more complete overview of conductivities and activation energies see Table 2. Generally, the activation energies are in line with the results from literature, albeit being slightly higher. It should be noted here that also the values from literature have some spread, and the measured values are well within the acceptable range. The higher activation energies might be explained by the fact that most results reported in literature are based on pellets pressed and sintered at temperatures of up to 550 °C, with the preparation procedure applied here omitting the sintering step. Consequently, higher activation energies and lower conductivities are expected. However, Bron et al. reported activation energies very similar in the low temperature regime but had a rather extensive preparation procedure including long pressing times and annealing.⁷⁰

The change of the activation energy at higher temperatures was also reported multiple times in literature. Kuhn et al. proposed that at lower temperatures the grain boundary contribution dominates the response of LGPS, and that at higher temperatures the grain boundaries become conducting enough so that the bulk conductivity becomes the limiting factor.⁵⁹ This assumption was based on the lower activation energy found for the bulk.⁵⁹ This could however not be reproduced in this investigation, with both grain boundaries and bulk having very similar activation energies. Additionally, single crystal studies by Iwasaki et al.⁴⁸, although reporting higher activation energies compared to compacted powder samples, indicate the same change in slope in the Arrhenius plot with lower activation energies at elevated temperatures above –20 °C. Since this is reported for high-quality single crystals, it is likely that the change in activation energy is related to a change in the ion dynamics and/or phase transition of the bulk. The exact temperature at which fitting is split up varies in literature, but is most around –20 °C to 20 °C.^{13,45,48,59}

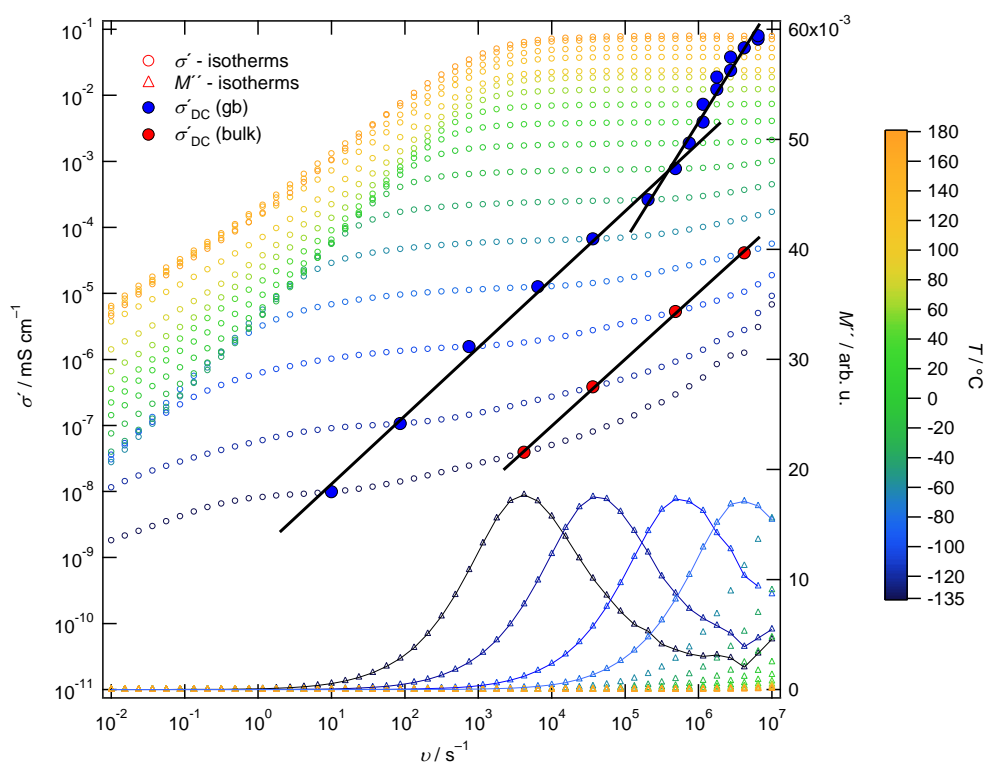


Figure 43: Conductivity spectrum of the best performing $\text{Li}_{10}\text{GeP}_2\text{S}_{12}$ sample in a frequency range of 10^{-2} to 10^7 Hz and a temperature range of -135 °C to 180 °C. Additionally to the conductivity isotherms the imaginary modulus M'' is plotted as a function of frequency. The conductivity values σ'_{DC} used for the Arrhenius plot in Figure 44 are indicated.

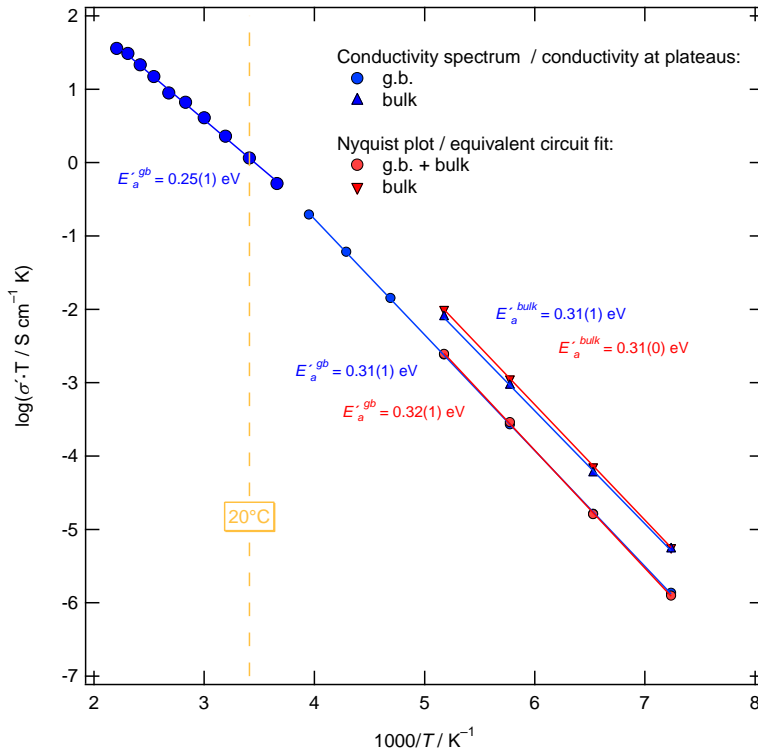


Figure 44: Arrhenius plot of LGPS with the individual conductivity data obtained from σ_{DC} of the isotherm plateaus and from Nyquist plots fitted with equivalent circuits.

Table 8: Results (framed red) and literature values for the conductivity σ' and activation energies E_a .

Reference	Material	Preparation	$\sigma' / \text{mS cm}^{-1}$ (T / K)	E_a / eV (T range / K, details)
Results	$\text{Li}_{10}\text{GeP}_2\text{S}_{12}$	Pellet with $\varnothing = 10$ mm and $t = 1$ mm, Au electrodes (sputtered) with $t = 50$ nm, no sintering	3.89 (298)	0.31(1) (138 - 253) 0.25(1) (253 - 453)
Kamaya et al. ¹³ as stated by Kato et al. ³⁸	-	-	-	0.31 (193 - 298) 0.17 (322 - 673)
Kuhn et al. ⁵⁹	$\text{Li}_{10}\text{GeP}_2\text{S}_{12}$	Annealed pellets with $\varnothing = 12$ mm, $t = 1.5$ -3 mm, Au electrodes (sputtered)	9.0 (298)	0.30 (168 - 250, associated with g.b.) 0.22 (250 - 498, associated with bulk)
Bron et al. ⁷⁰	$\text{Li}_{10}\text{GeP}_2\text{S}_{12}$	Pellet with $\varnothing = 6$ mm, $t = 0.5 - 1.5$ mm, pressed 45 min at 270 MPa, 24 h @ 500 °C, Au electrodes (sputtered)	9 (298)	0.30 (133 - 213 associated with bulk) 0.31 (133 - 213 associated with g.b.)

Spin-lattice relaxometry measurements were performed to further characterize the local ion dynamics in LGPS on a microscopic scale. The results for T_1 and $T_{1\rho}$ of ^7Li and ^{31}P measurements are presented in Figure 45 as an Arrhenius plot.

First, the data from the ^7Li measurements are discussed. Generally, the ^7Li results were in good agreement with the ones reported in literature.⁶⁴ The T_1 magnetization transients were fitted using a stretched exponential function (see Experimental, equation 38). One marked difference to literature was however that the magnetization transients recorded during the ^7Li $T_{1\rho}$ measurements indicated a double exponential instead of a simple exponential decay and were therefore fitted with a stretched double exponential function (see Experimental, equation 39). In Figure 45, both the results obtained with a simple stretched exponential and a stretched double exponential function are displayed. By fitting the high temperature slopes in Figure 45 linearly the activation energies of the observed jump processes could be obtained, yielding 0.11(2) eV for T_1 , and 0.14(1) eV and 0.31(1) eV for $T_{1\rho}$, respectively. It is likely, that the activation energies of 0.11(2) eV and 0.14(1) eV describe the same jump process, due to the similar activation energies and the high temperature slopes merging when extrapolated (see Methods, Figure 25). The activation energies obtained fit well with the activation energy of 0.17 eV calculated for migration along the c direction in the LGPS structure.⁵¹ Liang et al. reported activation energies of 0.18 eV and 0.16 eV derived from the high temperature slopes of ^7Li spin-lattice relaxation measurements, which were also interpreted as jumps along the c direction.⁶⁴ It should be noted that especially the activation energy derived from the T_1 data was low compared to the values reported experimentally and theoretically in literature. However, it is expected that further measurements at even higher temperatures would yield a steeper slope and consequently a higher activation energy. Such measurements were however not possible due to equipment constraints.

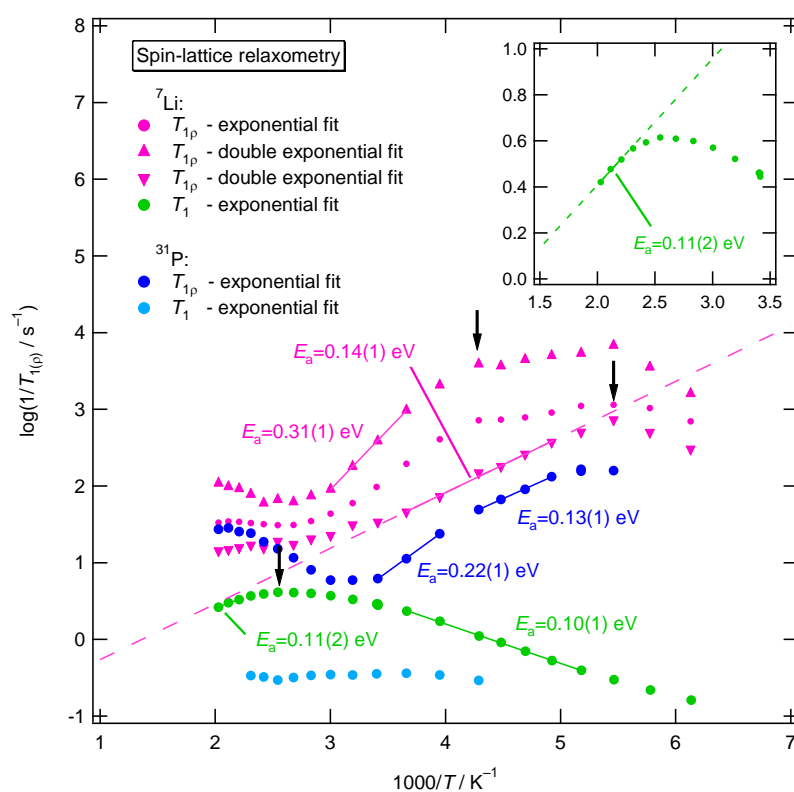


Figure 45: Arrhenius plots of the ^7Li (116 MHz) and ^{31}P (121 MHz) T_1 and $T_{1\rho}$ spin-lattice relaxation rates, the inset enlarges the ^7Li T_1 peak. Black arrow indicated that peak maxima used for calculating the correlation time τ_c .

The second activation energy derived from the $T_{1\rho}$ data is 0.31(1) eV and can be associated with the process of Li-ion migration in the ab plane, since the value fits good with the theoretical predicted activation energy of 0.28 eV.⁵¹ Also this value fits very well with the value obtained from impedance measurements, supporting the model that long-range ionic migration requires diffusion in the ab plane.⁴⁸

Table 9: Correlation times calculated from the maxima in the relaxation rate $1/T_{1(\rho)}$ of ${}^7\text{Li}$.

Experiment	Correlation time τ_c / s	T / K
T_1	1.4×10^{-9}	393.15
$T_{1\rho} - 1$	4.0×10^{-6}	233.15
$T_{1\rho} - 2$	4.0×10^{-6}	183.15

From the maxima in the relaxation rates and the Larmor frequency the correlation times at specific temperatures were calculated by the relations $\tau^{-1} = \omega_{L,0}$ and $\tau^{-1} = 2\omega_{L,1}$ with $\omega_{L,0}$ being the Larmor frequency in the laboratory frame and $\omega_{L,1}$ the Larmor frequency in the spin-lock experiment (in the rotating frame). The results are listed in Table 9.

In a last step, in order to allow comparison of the impedance and NMR data, the charge diffusion coefficients and the uncorrelated diffusion coefficients were calculated according to equations 25 and 35 and plotted in Figure 46. For the uncorrelated diffusion coefficient an average jump length of 3 Å was chosen. The interatomic distances between Li sites along known and assumed diffusion pathways ([Li1S₄]-[L1S₄]-[L3S₄], [Li2S₆]-[L3S₄] and [Li4S₆]-[Li1S₄]-[L1S₄]) were directly read out using the software program Vesta based on the crystallographic data from Kuhn et al..⁴⁷ Generally, the results from impedance/ conductivity spectroscopy and NMR match relatively good and the charge diffusion coefficients were fitted linearly. The uncorrelated diffusion coefficient associated with ab plane diffusion coincided with the extrapolated fit and this, together with the similarity in activation energy mentioned above, could indicate that ab plane diffusion is the limiting step in macroscopic, long-range Li-ion transport, as proposed by Iwasaki et al..⁴⁸

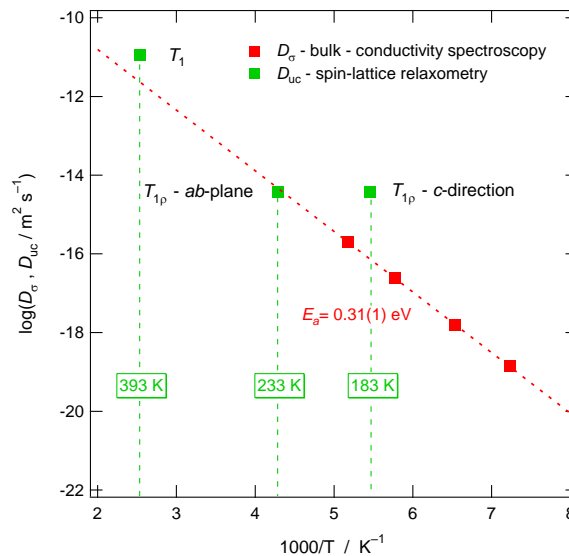


Figure 46: Arrhenius plot of the charge diffusion coefficients D_σ and uncorrelated diffusion coefficients D_{uc} obtained by ${}^7\text{Li}$ spin-lattice relaxometry.

Another interesting point to note is that the curve outlined by the $^{31}\text{P } T_{1\rho}$ values in the Arrhenius plot roughly follows the shape of the ^7Li data. Two activation energies were derived from the ^{31}P data, 0.22(1) eV and 0.13(1) eV, with the later matching very well with the activation energy for Li-ion migration along the c direction as obtained by the $^7\text{Li } T_{1\rho}$ data. At this point it cannot be determined if the values obtained by $^{31}\text{P } T_{1\rho}$ relaxometry originate from the same Li-ion migration processes that were probed with $^7\text{Li } T_{1\rho}$ relaxometry or if other processes are involved (e.g., paddle-wheel mechanism).

The $^{31}\text{P } T_1$ data showed little to no dependence on temperature and yielded therefore no additional information.

4.2 Oxygen substitution - $\text{Li}_{10}\text{GeP}_2\text{S}_{12-x}\text{O}_x$

In $\text{Li}_{10}\text{GeP}_2\text{S}_{12}$ sulfur can be substituted partially by oxygen, yielding $\text{Li}_{10}\text{GeP}_2\text{S}_{12-x}\text{O}_x$. As reported in literature, this can lead to improved stability of LGPS against Li metal anodes, potentially increasing battery life at the expense of reduced ionic conductivity.⁴⁶ $\text{Li}_{10}\text{GeP}_2\text{S}_{12-x}\text{O}_x$ with an $x = 0.3$ was synthesized by the same route as described for LGPS, but with Li_2S being partially replaced by Li_2O in order to achieve the stoichiometric ratio needed for $\text{Li}_{10}\text{GeP}_2\text{S}_{11.7}\text{O}_{0.3}$. The specimens were consequently characterized structurally by XRD, ^{31}P MAS NMR, and Raman spectroscopy.

The obtained powder was characterized by XRD. No significant differences or new phases were detectable in the XRD pattern. Rietveld refinement was performed using the structure reported by Kuhn et al. for conventional (not doped) LGPS as a starting point for refinement.⁴⁷ The occupancy parameters were adjusted in a way to house the additional oxygen as reported in literature.⁴⁶ The agreement indices attained were $R_{\text{exp}} = 9.49$, $R_{\text{wp}} = 15.84$ and $GOF = 5.15$, comparable to the results for $\text{Li}_{10}\text{GeP}_2\text{S}_{12}$.

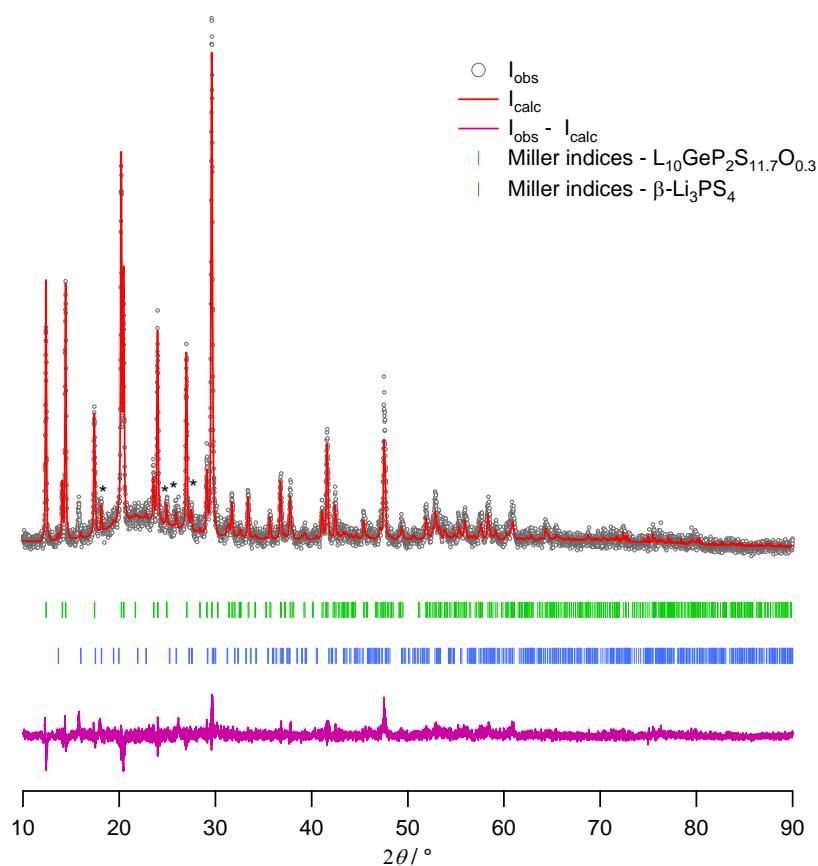


Figure 47: Rietveld refinement of $\text{Li}_{10}\text{GeP}_2\text{S}_{11.7}\text{O}_{0.3}$ at the Rigaku SmartLab with a step size of 0.01° and an acquisition speed of $2^\circ/\text{min}$, (top) Experimental and simulated pattern. (middle) Peak positions associated with $\text{Li}_{10}\text{GeP}_2\text{S}_{11.7}\text{O}_{0.3}$ and $\beta\text{-Li}_3\text{PS}_4$. (bottom) Difference plot indicating error.

Table 10: Lattice parameters of the tetragonal structure obtained by Rietveld refinement of $\text{Li}_{10}\text{GeP}_2\text{S}_{12}$ and $\text{Li}_{10}\text{GeP}_2\text{S}_{11.7}\text{O}_{0.3}$

Chemical formula	$a / \text{\AA}$	$c / \text{\AA}$
$\text{Li}_{10}\text{GeP}_2\text{S}_{12}$	8.6975(3)	12.5940(2)
$\text{Li}_{10}\text{GeP}_2\text{S}_{11.7}\text{O}_{0.3}$	8.6796(3)	12.5778(8)

The refined lattice parameters are listed in Table 10. As expected, and reported in literature, the unit cell of the oxygen substituted LGPS was slightly smaller due to the smaller radius of the oxygen compared to sulfur.^{27,46} The change in lattice parameters were 0.20 % in a / b-direction and 0.13 % in c direction. These changes were comparable small to the values reported in literature, 0.68 % and 0.33 %. It should also be noted that the refined lattice parameters of LGPS itself were already smaller than the values stated by Sun et al., possibly indicating the presents of oxygen impurities in $\text{Li}_{10}\text{GeP}_2\text{S}_{12}$ itself.⁴⁶

Since in $\text{Li}_{10}\text{GeP}_2\text{S}_{11.7}\text{O}_{0.3}$ oxygen replaces sulfur in the crystal structure, and all sulfur species in LGPS neighbor a site fully (2b) or at least partially (4d) occupied by phosphor,⁴⁷ probing phosphor by ^{31}P MAS NMR should reveal the oxygen substitution in $\text{Li}_{10}\text{GeP}_2\text{S}_{11.7}\text{O}_{0.3}$. As mentioned already above, three distinct peaks associated with the oxygen substitution of sulfur at the $[\text{PS}_4]^{3-}$ units are reported in literature, with $[\text{PS}_2\text{O}_2]^{3-}$ at 67 ppm, $[\text{PO}_3\text{S}]^{3-}$ at 36 ppm and $[\text{PO}_4]^{3-}$ at 9 ppm.^{61,107,108} As seen in Figure 48, spectra of both $\text{Li}_{10}\text{GeP}_2\text{S}_{12}$ and $\text{Li}_{10}\text{GeP}_2\text{S}_{11.7}\text{O}_{0.3}$ contained the peaks at 67 ppm and 36 ppm, with the former being clearly, but the later only hardly visible and no peak was observed around 9 ppm. However, no distinct difference between both spectra could be identified. Contradicting, the peaks associated with oxygen-substitution seemed to be marginally more pronounced in the $\text{Li}_{10}\text{GeP}_2\text{S}_{12}$ sample. Nevertheless, oxygen seemed to be present in both $\text{Li}_{10}\text{GeP}_2\text{S}_{12}$ and $\text{Li}_{10}\text{GeP}_2\text{S}_{11.7}\text{O}_{0.3}$ in minor quantities and no quantitative differentiation in oxygen content between the two specimens could be obtained. An additional sample with the composition $\text{Li}_{10}\text{GeP}_2\text{S}_{11.5}\text{O}_{0.5}$, i.e., higher oxygen content ($x = 0.5$), was also synthesized and characterized with ^{31}P MAS NMR, but with again only marginal differences observable.

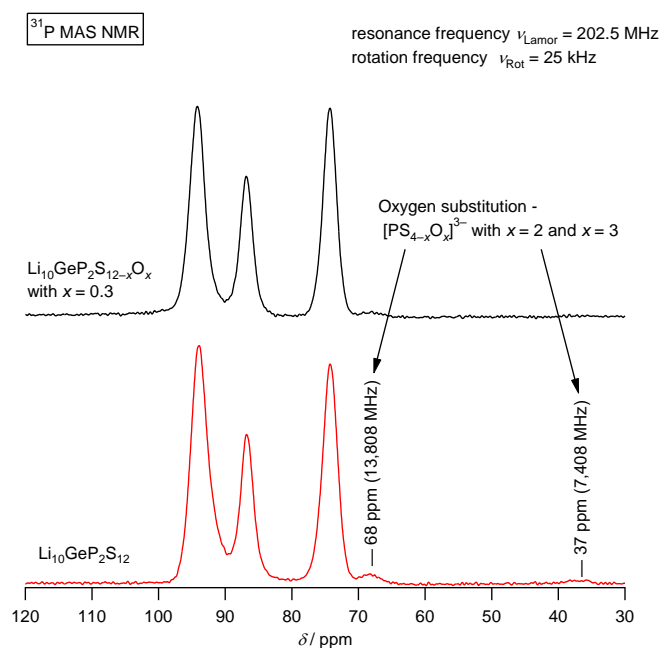


Figure 48: ^{31}P MAS NMR spectra of (top) $\text{Li}_{10}\text{GeP}_2\text{S}_{11.7}\text{O}_{0.3}$ and (bottom) $\text{Li}_{10}\text{GeP}_2\text{S}_{12}$.

Additionally, the specimens were characterized by Raman spectroscopy, as differentiation between conventional and oxygen substituted LGPS was achieved in literature by this method.⁴⁶ The spectra are given in Figure 49 and 50. The spectra agreed well with the ones reported in literature and each band (except one) in the spectra could be attributed to a distinct vibrational mode.^{46,72} Consequently, LGPS could also be unambiguously identified by Raman spectroscopy. However, the supposed unique feature of the spectrum of $\text{Li}_{10}\text{GeP}_2\text{S}_{11.7}\text{O}_{0.3}$, the peak at about 430 cm^{-1} associated with $[\text{PS}_{4-x}\text{O}_x]^{3-}$, was present in both conventional and oxygen-substituted LGPS and was not significantly more pronounced in $\text{Li}_{10}\text{GeP}_2\text{S}_{11.7}\text{O}_{0.3}$.

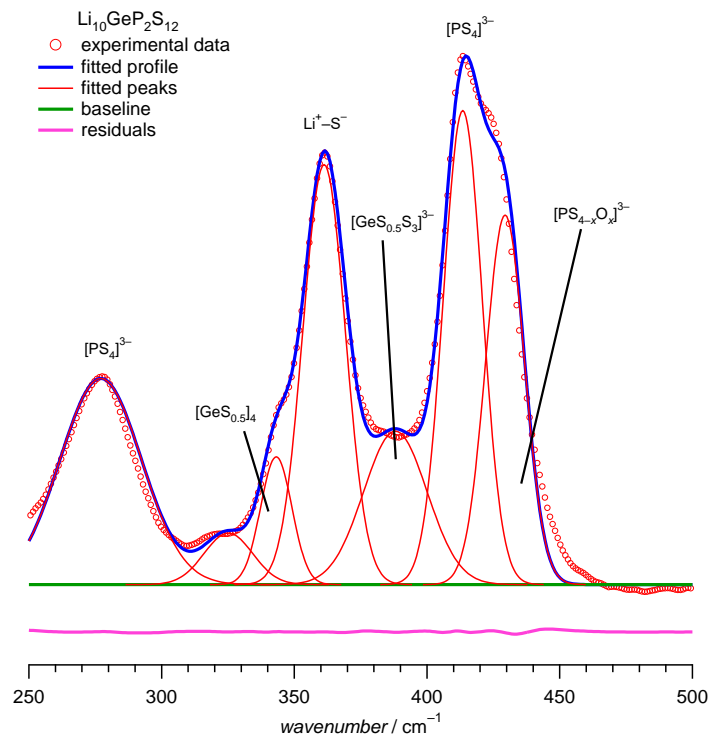


Figure 49: Raman spectrum of $\text{Li}_{10}\text{GeP}_2\text{S}_{12}$ obtained with a 532 nm Laser source (top) Bands are fitted using gaussians, obtaining a fitting profile. (bottom) residuals. The assigned vibrational modes are also indicated for each peak.

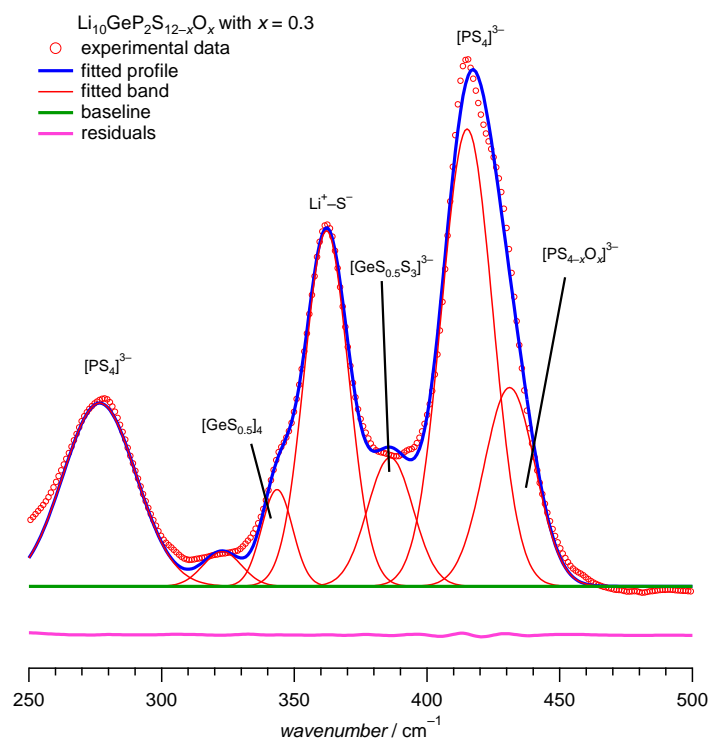


Figure 50: Raman spectrum of $\text{Li}_{10}\text{GeP}_2\text{S}_{11.7}\text{O}_{0.3}$ obtained with a 532 nm Laser source. (top) Bands are fitted using gaussians, obtaining a fitting profile. (bottom) residuals. The assigned vibrational modes are also indicated for each peak.

The ion dynamics of $\text{Li}_{10}\text{GeP}_2\text{S}_{11.7}\text{O}_{0.3}$ were probed by impedance spectroscopy, utilizing the same parameters as for $\text{Li}_{10}\text{GeP}_2\text{S}_{12}$. The conductivity at 20 °C was 2.17 mS cm^{-1} , see Figure 51. This was about half the conductivity of the best LGPS sample measured. As already mentioned, the conductivity of the samples can vary considerably, especially due to differences of the grain boundary contribution, with the best LGPS sample having a room temperature conductivity of 3.89 mS cm^{-1} , and the worst 0.41 mS cm^{-1} . However, when comparing the bulk plateaus in the conductivity spectra, the plateau of $\text{Li}_{10}\text{GeP}_2\text{S}_{11.7}\text{O}_{0.3}$ lies slightly lower than the one associated with of $\text{Li}_{10}\text{GeP}_2\text{S}_{12}$, see Figure 52. This indicated a slightly lower bulk conductivity of the oxygen substituted sample, as would be expected.⁴⁶ Consequently, the bulk conductivity of the oxygen-substituted variant is slightly lower, but due to the strongly variable grain boundary contribution, the total conductivity could not be proven to be significantly lower compared to conventional LGPS. In literature, only total conductivities with no differentiation between bulk and grain boundaries was reported, with a stated room temperature conductivity of 12 mS cm^{-1} for $\text{Li}_{10}\text{GeP}_2\text{S}_{12}$ and 10.3 mS cm^{-1} for $\text{Li}_{10}\text{GeP}_2\text{S}_{11.7}\text{O}_{0.3}$, a reduction of about 14 %.⁴⁶ The bulk conductivities read off from the isotherms in Figure 52 at -135 °C were $3.9 \times 10^{-6} \text{ mS cm}^{-1}$ and $2.7 \times 10^{-6} \text{ mS cm}^{-1}$ for $\text{Li}_{10}\text{GeP}_2\text{S}_{12}$ and $\text{Li}_{10}\text{GeP}_2\text{S}_{11.7}\text{O}_{0.3}$ respectively, indicating a reduction of 31 %.

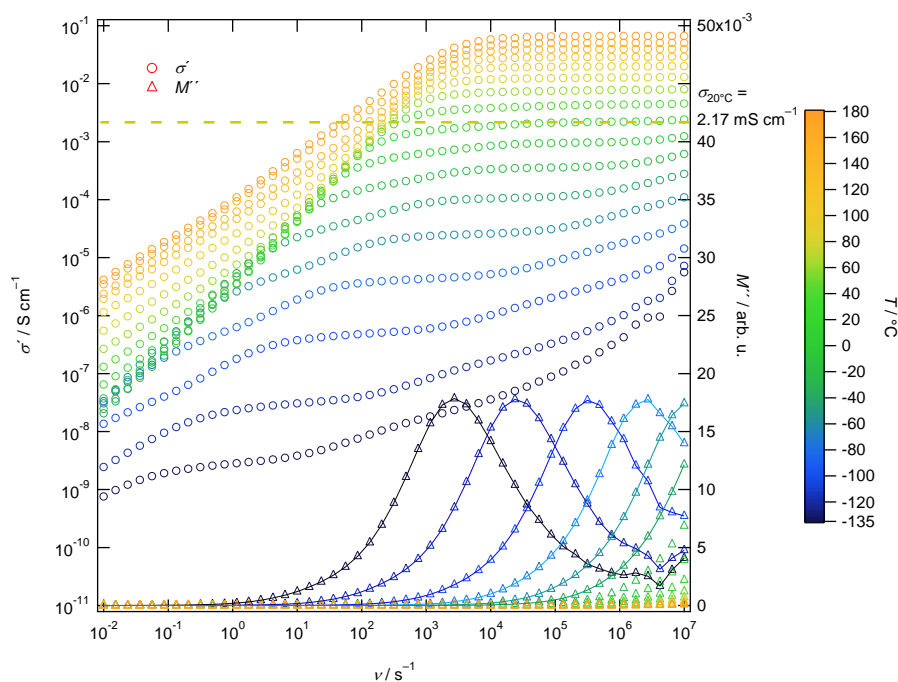


Figure 51: Conductivity spectrum of $\text{Li}_{10}\text{GeP}_2\text{S}_{11.7}\text{O}_{0.3}$ annealed for 8 h @ 550 °C in a frequency range of 10^{-2} to 10^7 Hz and a temperature range of -135 °C to 180 °C . Additionally to the conductivity isotherms the imaginary modulus M'' is plotted (linear scale) as a function of frequency.

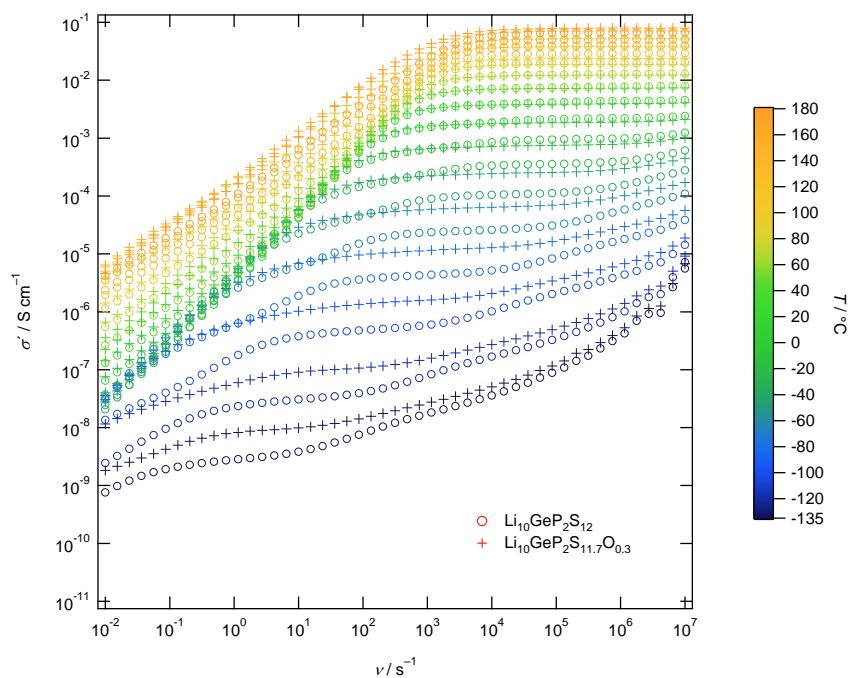


Figure 52: Conductivity spectra of $\text{Li}_{10}\text{GeP}_2\text{S}_{12-x}\text{O}_x$ with $x = 0$ and $x = 0.3$ annealed for 8 h @ 550 °C in a frequency range of 10^{-2} to 10^7 Hz and a temperature range of -135 °C to 180 °C.

To sum up, evidence of oxygen substitution was found in both $\text{Li}_{10}\text{GeP}_2\text{S}_{12}$ and $\text{Li}_{10}\text{GeP}_2\text{S}_{11.7}\text{O}_{0.3}$ using XRD, ^{31}P MAS NMR and Raman spectroscopy. However, structural characterization techniques showed no evidence for a significantly higher oxygen content in the oxygen substituted LGPS variant. One possible explanation would be the introduction of oxygen through the starting materials or during synthesis and handling (ball milling). For example, for some samples it was observed that when opening the milling beakers in the glove box after milling the oxygen level rose by up to 1 ppm. This could hint at a contamination with oxygen during ball milling. Interestingly, Hayashi et al. evaluated the oxygen content present in LGPS synthesized by the conventional (annealing pelletized sample in an evacuated and sealed quartz tube) and a new solid-state synthesis method (annealing of powder under argon flow) using non-dispersive infrared spectroscopy and found some oxygen contamination in both materials, with $x < 0.51$ in $\text{Li}_{10}\text{GeP}_2\text{S}_{12-x}\text{O}_x$, arguing that the contamination might originate from the starting materials.⁶⁰ Consequently, both LGPS variants would contain oxygen and the oxygen substituted sample would only contain marginally more. This would explain the difficulties in finding quantitative differences between the samples with formal compositions $\text{Li}_{10}\text{GeP}_2\text{S}_{12}$ and $\text{Li}_{10}\text{GeP}_2\text{S}_{11.7}\text{O}_{0.3}$. Since no distinct and quantitative difference was found between $\text{Li}_{10}\text{GeP}_2\text{S}_{12}$ and $\text{Li}_{10}\text{GeP}_2\text{S}_{11.7}\text{O}_{0.3}$, the oxygen-substituted variant was not included in the further investigation on nanostructuring.

4.3 Nanostructuring by ball milling

4.3.1 Structural characterization

LGPS was milled using the planetary ball mill for different durations and milling speeds (rpm), with the exact parameters tabulated in Table 11.

Table 11: Samples prepared by nanostructuring.

Milling time / min	Milling intensity / rpm
15	300
15	400
30	400
60	400
120	400

In a first step the specimens were structurally characterized by XRD. The individual peaks broadened as milling time and speed were increased, see Figure 53. This indicated a decrease in crystallite size by mechanical ball milling. At the right side of Figure 53 the most intensive reflex of the pattern at $\approx 29.5^\circ$ is enlarged, making the increase in width better visible. Samples milled 15 min and 30 min display relatively sharp reflexes, typical for a crystalline phase. Nevertheless, an increase in peak width is still observable. Compared to that the specimens milled for 60 min and 120 min show only few, poorly resolved and very broad reflexes, pointing towards little crystalline phase remaining and/or a greatly reduced crystallite size. To quantify these observations the enlarged peak at 29.5° was fitted using a Voigt function and the fwhm was calculated, see Table 12. The fwhm increased with intensified and prolonged milling, with a particularly larger step in fwhm in between 30 and 60 min of milling.

Using the Scherrer equation one can calculate the crystallite size from the fwhm. However, in a first step, the instrumental broadening must be subtracted in order correctly calculate the crystallite size. With the used instrumentation this was however not possible.

Table 12: Fwhm values obtained by fitting the peak at 29.5° , see Figure 53 right, with a Voigt function.

	Microcrystalline (annealed)	15 min @ 300 rpm	15 min @ 400 rpm	30 min @ 400 rpm	60 min @ 400 rpm	120 min @ 400 rpm
fwhm	0.18	0.19	0.23	0.30	0.84	0.96

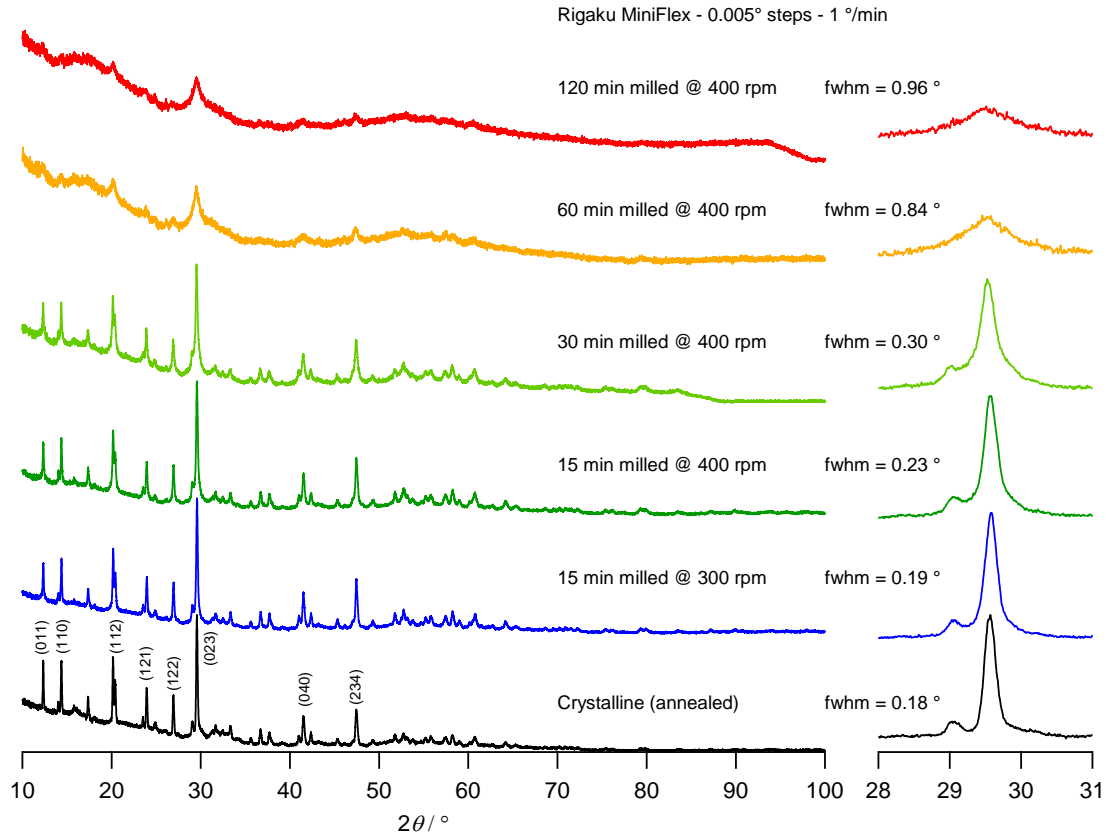


Figure 53: XRD patterns of $\text{Li}_{10}\text{GeP}_2\text{S}_{12}$ for different milling times and speeds recorded at the at the Rigaku SmartLab with a step size of 0.005° and an acquisition speed of $1^\circ/\text{min}$. (right) The peak at 29.5° used for determining the fwhm values in Table 12 is enlarged.

To obtain more detailed information about the crystalline and potentially amorphous phases present after ball milling ^{31}P MAS NMR was performed. For the ball milled samples a new, broad peak appeared at around 83 ppm in the spectrum, see Figure 55. In literature a peak at 83 ppm was reported for chain units analogous to metaphosphate groups in $\text{Li}_2\text{S}-\text{P}_2\text{S}_5$ glasses.¹⁰⁵ This structural unit is also referred to as a $\text{Q}^{(2)}$ species, meaning it is a coordination polyhedron with two P-S-P bridges, see Figure 54.¹⁰⁵ These $\text{Q}^{(2)}$ units then build up polymeric chains in the glass, consisting of edge-sharing $[\text{PS}_4]^{3-}$ tetrahedral units.¹⁰⁵ As milling time and speed increased, this peak grew until it was the dominant peak for specimens milled for 60 and 120 min. Therefore, this peak was attribute to the amorphous phase forming during ball milling. This was inferred also by the fact that the peak is directly related to the milling time and does not coincide with any other known side phase of LGPS. Also, the peak was very broad, indicative of the absence of a regular (crystalline) chemical environment around the ^{31}P sites probed, as can typically be found in amorphous phases. Additionally, the peak was situated in between the two peaks ascribed to LGPS and it would be expected that the chemical environment of ^{31}P in amorphous LGPS should be somewhat an average of the two distinct crystallographic sites of the crystalline form.

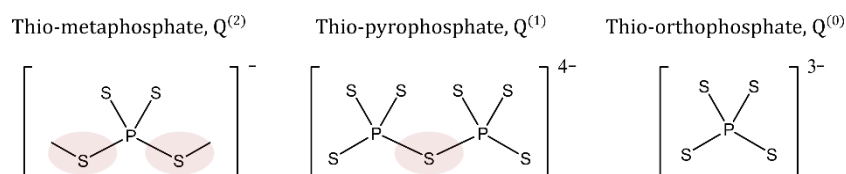


Figure 54: Structural units analogous to meta-, pyro- and orthophosphate. $\text{Q}^{(n)}$ indicates the coordination environment with n being the number of bridging S atoms (red)

The peaks were fitted using Voigt functions and the fractions of amorphous and crystalline phases could be calculated from the fitted peak areas using equation 40. The results are tabulated in Table 13 and visualized in Figure 55. Also, the amount of side phase reduced with increasing milling time, likely also forming an amorphous phase similar to LGPS. It is not known how this amorphous phase, originating from the side phase, is different from the amorphous phase of LGPS, as chemically $\text{Li}_{10}\text{GeP}_2\text{S}_{12}$ and $\beta\text{-Li}_3\text{PS}_4$ (able to form a solid solution with Ge, see Figure 5) are not very different and consequently their respective amorphous forms might be structurally similar. Only a single amorphous form could be identified in the ^{31}P MAS NMR. It should be noted that for the specimens milled for 60 min and 120 min, due to the overlap with the dominant amorphous peak, the peak associated with the orthorhombic side phase could not be quantified anymore and consequently the phase fraction of it was set to zero.

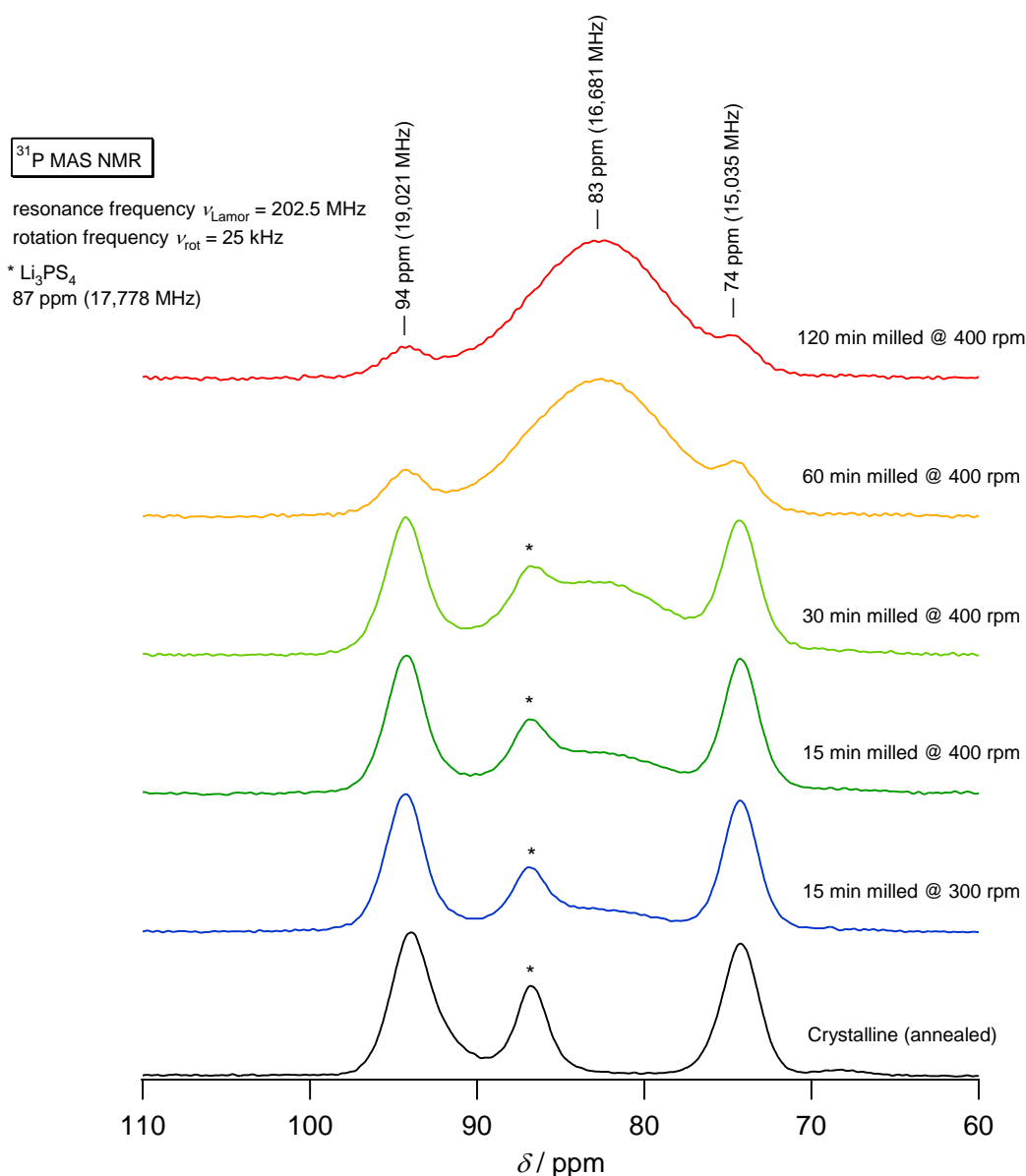


Figure 55: ^{31}P MAS NMR spectrum of $\text{Li}_{10}\text{GeP}_2\text{S}_{12}$ milled for different times and intensities.

Table 13: Phase fractions of $\text{Li}_{10}\text{GeP}_2\text{S}_{12}$ (yellow in Figure 56), $\beta\text{-Li}_3\text{PS}_4$ / orthorhombic side phase (blue) and amorphous (LGPS-related) phase (red) as calculated from the ^{31}P MAS NMR peak areas.

Sample	$\text{Li}_{10}\text{GeP}_2\text{S}_{12}$ / wt%	$\beta\text{-Li}_3\text{PS}_4$ / wt%	Amorphous phase / wt%
Microcrystalline (annealed)	85	15	0
15 min @ 300 rpm	74	11	15
15 min @ 400 rpm	62	11	27
30 min @ 400 rpm	43	7	50
60 min @ 400 rpm	16	0	84
120 min @ 400 rpm	12	0	88

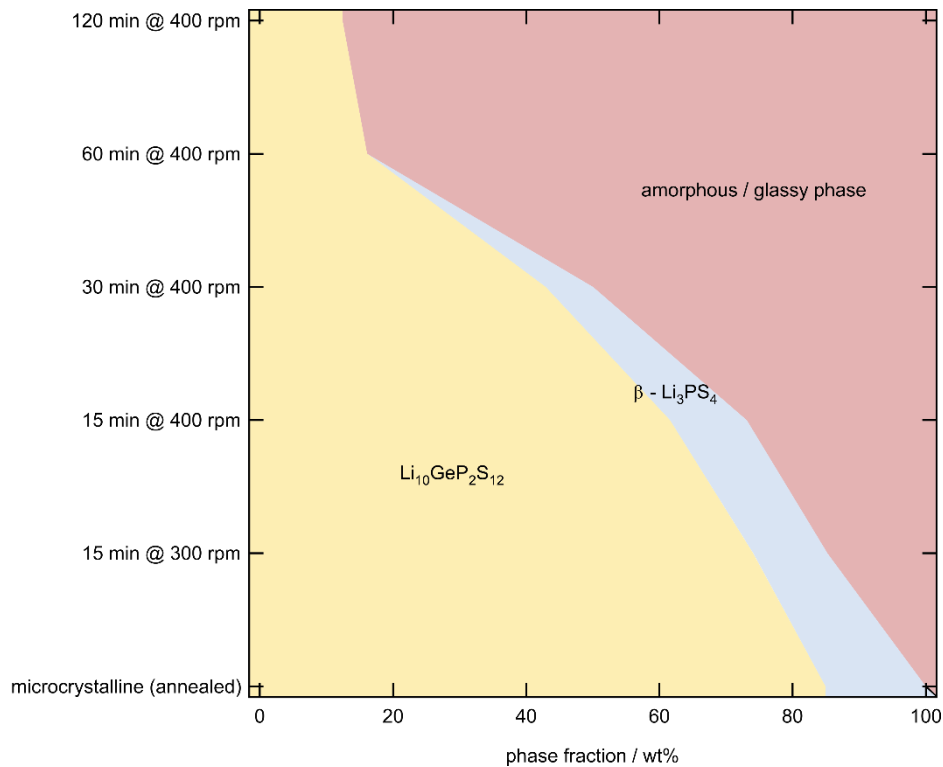


Figure 56: Evolution of phase fractions of $\text{Li}_{10}\text{GeP}_2\text{S}_{12}$ (yellow), $\beta\text{-Li}_3\text{PS}_4$ / orthorhombic side phase (blue) and amorphous (LGPS-related) phase (red) as calculated from ^{31}P MAS NMR.

^6Li MAS NMR showed changes in the samples as milling time and speed increased. The spectra of the microcrystalline sample, see Figure 57, contained a sharp (fwhm = 7.15 Hz) peak at 0.47 ppm, indicative of the rapid Li motion in the material. A second smaller signal was present at 0.93 ppm. For samples milled for short times, a shoulder at higher frequencies arose for the peak at 0.47 ppm. This peak increased in intensity and shifted to higher frequencies with increasing milling time. The peak at 0.93 ppm is hardly visible in the samples milled 15 min (at 300 rpm and 400 rpm) and is not observable anymore in the other milled specimens. For the samples milled 60 min and 120 min, the original peaks at 0.47 ppm and 0.93 ppm completely vanished and a new peak emerges at 0.73 ppm with a fwhm of 9.83 Hz. This indicated a change in the Li coordination environment as the specimens were ball milled.

Based on the results obtained from ^{31}P MAS NMR, a likely option would be that the signal at 0.73 ppm can be associated with an amorphous phase. However, ^6Li MAS NMR literature values of $(\text{Li}_2\text{S})_x \cdot (\text{P}_2\text{S}_5)_{x-1}$ glasses reported lower chemical shifts.¹⁰⁵ Again, the experimentally determined chemical shift had to be referenced indirectly to solid LiCl resulting in a chemical shift of 1.97 ppm instead of 0.73 ppm. Literature values for $(\text{Li}_2\text{S})_x \cdot (\text{P}_2\text{S}_5)_{x-1}$ were between 1.40 ppm ($x = 0.4$, lower Li concentration) to 1.66 ppm ($x = 0.7$, higher Li concentration).¹⁰⁵ One possible interpretation could be that the very high Li concentration in LGPS, and followingly in the amorphous phase, would shift these values even more downfield. It is interesting to note that the peak associated with the amorphous phase did not simply increase in intensity and was otherwise fixed in position, but continuously shifted downfield as milling time increased. A possible interpretation of the continuous shift of the peak would be that the average Li-ion environment in the amorphous phase was further disturbed as milling continued, and consequently the peak position changed. This would suggest that ^{31}P MAS NMR was less sensitive to such minor and continuous changes in the coordination environment. The reason for this could be that the first coordination shell around P did not change as the $[\text{PS}_4]^{3-}$ units tend to be relative rigid and compact (considerable covalent bonding character), while Li has a looser coordination shell that could get more easily disturbed during ball milling. Both peaks at 0.73 ppm (fwhm = 9.83 Hz) and 0.47 ppm (fwhm = 7.15 Hz) were relatively sharp, indicating rapid Li diffusion in both the crystalline and the amorphous phase.

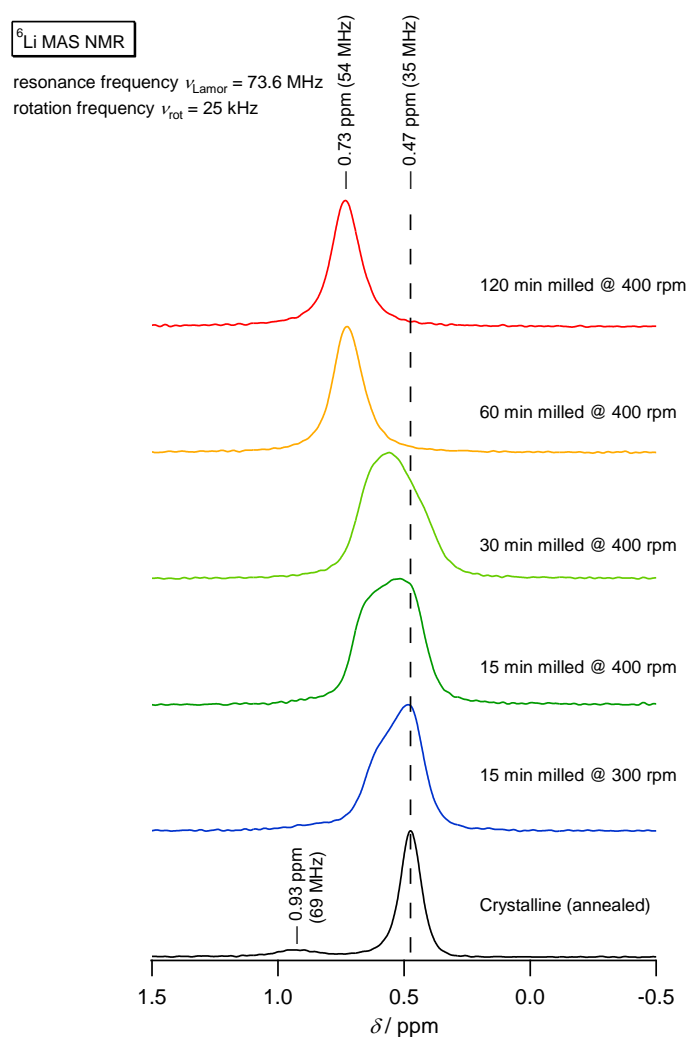


Figure 57: ^6Li MAS NMR spectrum of $\text{Li}_{10}\text{GeP}_2\text{S}_{12}$ milled for different times and intensities. Referenced against $\text{H}_3\text{COOLi} \cdot 2\text{H}_2\text{O}$.

4.3.2 Ionic conductivity and ion dynamics

The ionic conductivity of the nanostructured samples was probed by impedance spectroscopy and the results are summarized in Table 14. The obtained conductivity spectra of all samples are presented in Figure 59. It could be clearly seen that the room temperature conductivity was reduced due to the additional ball milling step and gradually decreased with longer milling times. The electric modulus formalism was again used to separate bulk and grain boundary contributions. However, for the milled specimens a shoulder in the peak of M'' arose and eventually became the dominant peak. Both peaks shifted to lower frequencies with increasing milling time. Since the maximum in M'' equals $\varepsilon/2C^{99}$ (more sensitive to bulk processes) and both peaks have heights of similar magnitude, both peaks were associated with bulk processes. The peak at higher frequencies and followingly the inclined conductivity plateau in that range was ascribed to the bulk crystalline response, as previously discussed for the not milled (microcrystalline) sample. The peak at lower frequencies must be attributed to a second bulk process taking place in the sample. Combining these results with the interpretation of the ^{31}P MAS NMR data, proving the presence of an amorphous phase, the M'' peak and its associated plateau at lower frequencies were assigned to the amorphous phase. No grain boundary plateau or contribution could be identified for the milled samples. The resistivity of the amorphous phase was high compared to the resistivity of the grain boundaries, as can be seen by comparing the plateaus in the conductivity spectra and could be the main reason for the decrease in room temperature conductivity of the milled materials. The evolution of the M'' peaks with increased milling time and speed can be clearly seen in Figure 58, only depicting the measurement results at -135°C .

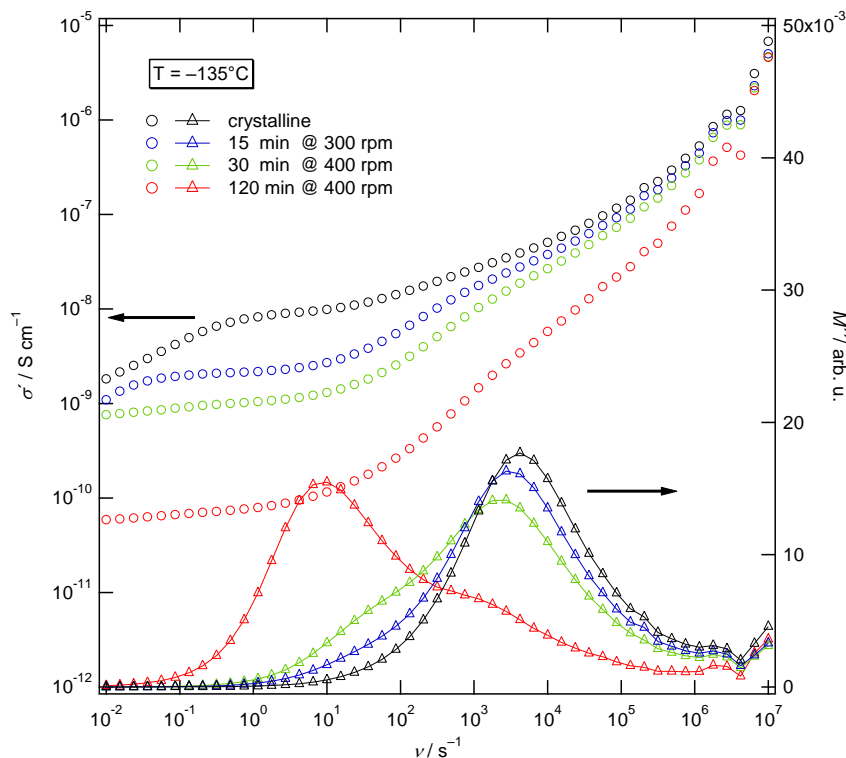


Figure 58: Conductivity spectrum of microcrystalline and milled $\text{Li}_{10}\text{GeP}_2\text{S}_{12}$ in a frequency range of 10^{-2} to 10^7 Hz and a temperature of -135°C . Additionally to the conductivity isotherms the imaginary modulus M'' is plotted (linear scale) as a function of frequency.

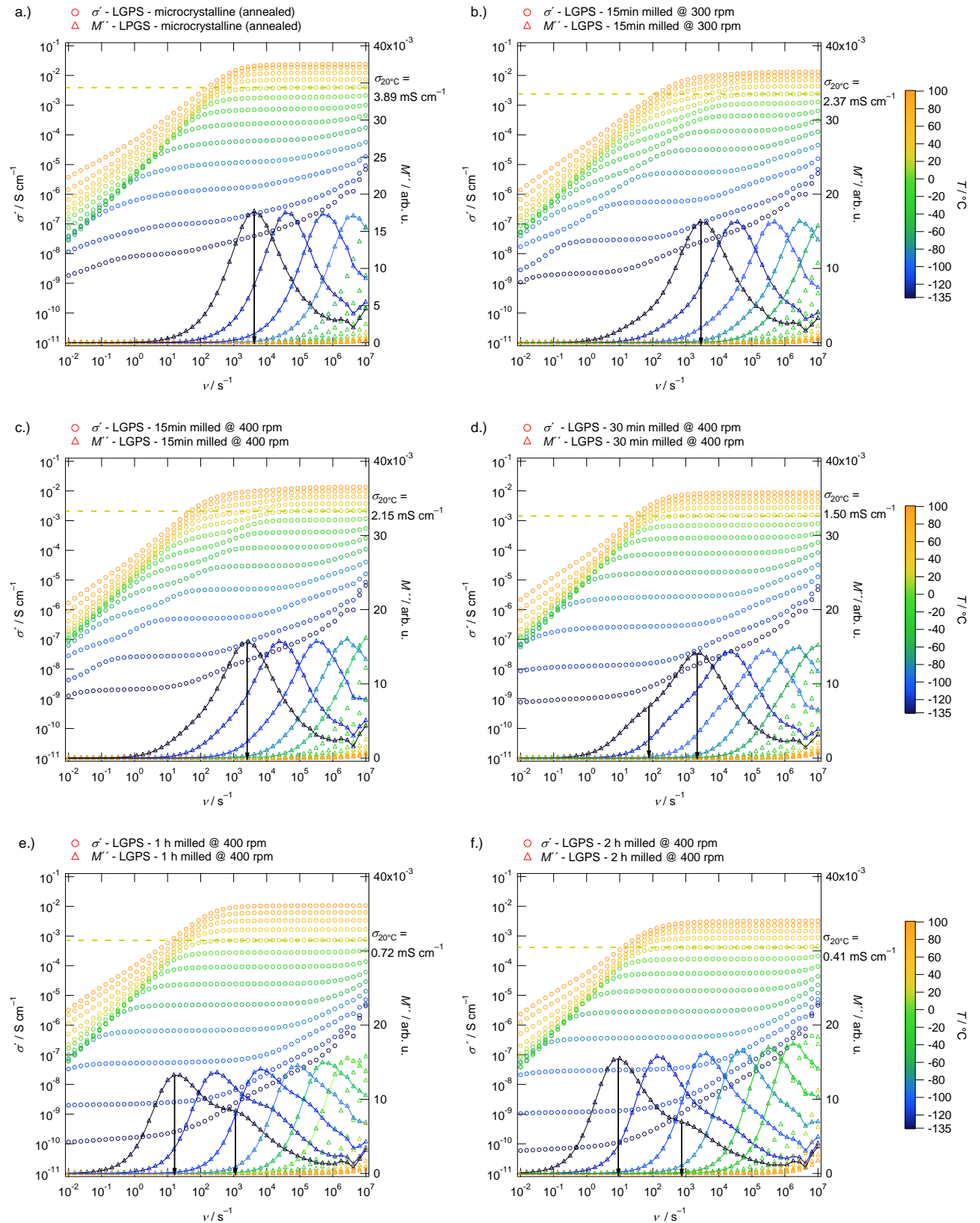


Figure 59: Conductivity spectra of $\text{Li}_{10}\text{GeP}_2\text{S}_{12}$ in the frequency range 10^{-2} to 10^7 Hz and temperature range -135 °C to 100 °C. a.) As-synthesized and annealed (microcrystalline) LGPS. LPS ball milled for b.) 15 min @ 300 rpm, c.) 15 min @ 400 rpm, d.) 30 min @ 400 rpm, e.) 60 min @ 400 rpm, f.) 120 min @ 400 rpm. Additional to the conductivity isotherms the imaginary modulus M'' is plotted (linear scale) as a function of frequency with arrows indicating the (suspected) peak maxima at -135 °C.

For lower temperatures, a reasonable Nyquist plot could be obtained and was fitted using different equivalent circuits, see Figure 61. For the microcrystalline and for 15 min milled samples, the (crystalline) bulk could still be separated from the total response and was therefore considered in the equivalent circuit during fitting. However, for the other samples the resistivity of the supposed amorphous phase was too high compared to the crystalline bulk and the capacitances were too close in order to resolve the bulk contribution.^{95,99} Consequently, a reduced equivalent circuit, only containing a single RC-element describing the amorphous/nanocrystalline material, was used for fitting this data. It is interesting to note that the fitted capacitance for the amorphous contribution decreased steadily as milling time, and consequently amorphous fraction, increased. For the sample milled 15 min at 300 rpm, the capacitance was about 0.14 nF, still relatively close to the original capacitance of 0.41 nF of the grain boundaries. This higher capacitance also matched with the shoulder in M'' , see Figure 59 b.), being relatively weakly pronounced. Therefore, the low frequency plateau in Figure 59, b.), could be either the grain boundary and amorphous contributions overlapping, or it could indicate that the small fraction of amorphous phase in between the crystallite domains has still considerable grain boundary character.

Based on these results and the general theory for the capacitances of the different contributions, a model is proposed, see Figure 60. The capacitance of the individual contributions can be calculated by the simple equation:⁹⁹

$$C = \varepsilon_r \varepsilon_0 \frac{A}{l} \quad (41)$$

With ε_r being the relative permittivity, ε_0 the permittivity of the vacuum, A the area and l the thickness. The relative capacitances, assuming a “Brickwork” model, of bulk and grain boundaries, according to:⁹⁹

$$\frac{C_b}{C_{gb}} = \frac{l_{gb}}{l_b} \quad (42)$$

As milling proceeds, the originally crystalline grains are mechanically destroyed and converted into smaller crystallites and amorphous phase, as determined by ³¹P MAS NMR and XRD. This amorphous phase will be generated mainly at the outer layers of the grains and the grain boundaries.¹¹⁵ Consequently, the grain boundaries become less defined and are replaced by a diffuse amorphous region in between the crystalline grains, like a core-shell structure, with an increased spacing l_a instead of l_{gb} . Simultaneously, the crystallite size, as determined by XRD, and therefore also l_b is reduced during the milling process and consequently the bulk capacity is increased, resulting in a smaller max. value of M'' . This would explain the evolution of M'' vs. ν as milling time and intensity is increased, with the capacitance of the bulk crystalline contribution increasing and the capacitance of the grain boundaries / amorphous matrix decreasing.

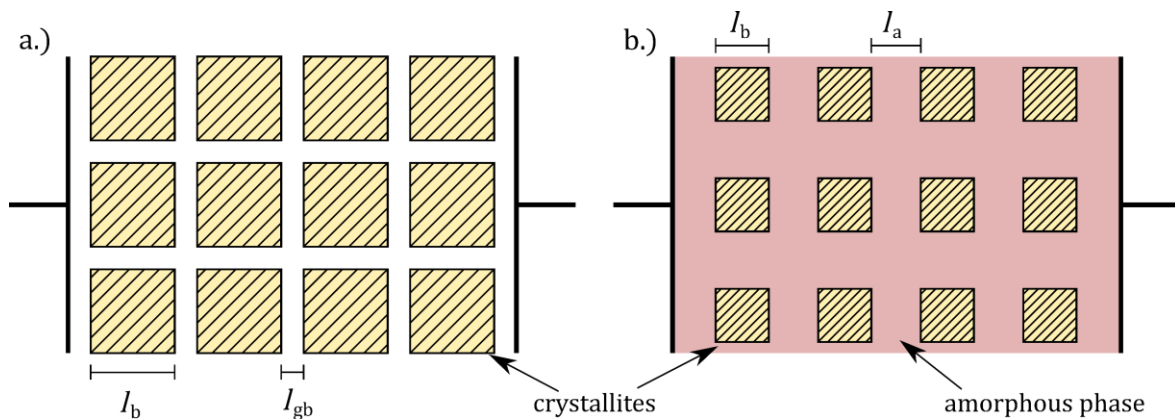


Figure 60: “Brickwork” model a.) as described in literature and, b) as applied to the nano-structuring of LGPS.

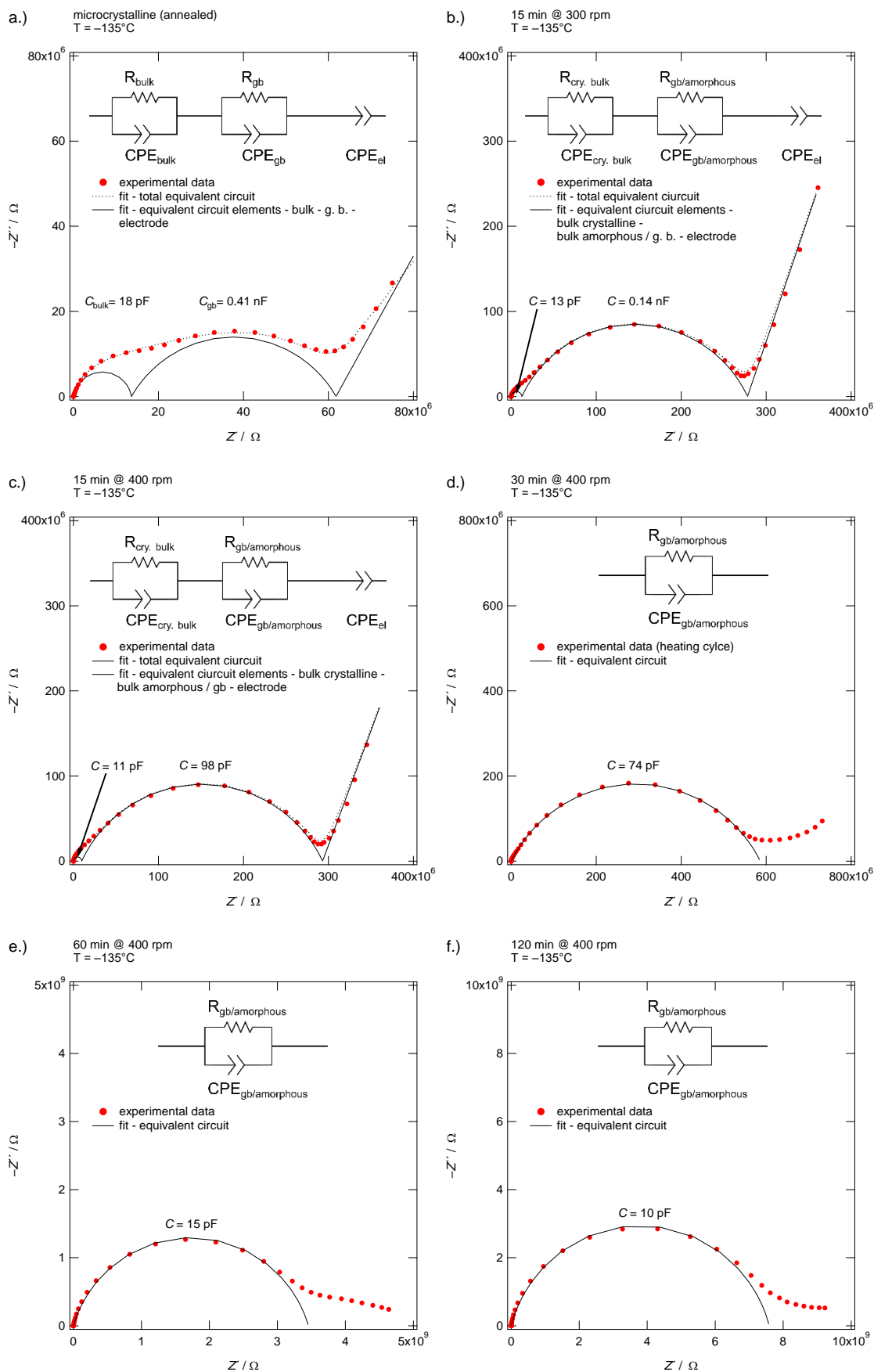


Figure 61: Nyquist plots including equivalent circuits and fit results of $\text{Li}_{10}\text{GeP}_2\text{S}_{12}$ at -135°C a.) as synthesized and annealed (microcrystalline) and ball milled for b.) 15 min @ 300 rpm, c.) 15 min @ 400 rpm, d.) 30 min @ 400 rpm, e.) 60 min @ 400 rpm, f.) 120 min @ 400 rpm.

Crystalline bulk and amorphous components were separated as discussed above. All milled samples showed an Arrhenius behavior similar to the microcrystalline sample, see Figure 62. Generally, the lines shift towards lower conductivities and slightly increased activation energies with longer milling times. The change in slope and therefore activation energy at higher temperatures could still be observed and happened in the same temperature range as for untreated LGPS. The activation energy in the high temperature regime was mostly the same, albeit with slightly higher energies for the milled samples. The sample milled for 60 min showed an unexpected behavior with comparable high activation energy at high temperatures, possibly due to a measurement error. It is interesting that even the sample milled for 120 min @ 400 rpm showed this change in activation energy at elevated temperature since crystalline LGPS only constitutes about 12 % of the sample. This could indicate that the glassy phase also goes through a change in ion dynamics or a phase transition in the same temperature range. If this change is also present in “glassy LGPS”, it is likely that the change in activation energy is not related to the grain boundaries in normal microcrystalline LGPS, but to the bulk itself. However, it should be noted that this interpretation is tentative, since different contributions could overlap in these samples and since the origin of this change in activation energy is not clarified yet. Interestingly, also the conductivity of the crystalline bulk was reduced with increasing milling time and the corresponding reduction in crystallite size, which could be seen clearly as the lines in the Arrhenius plot in Figure 63 shifted to smaller conductivity values and higher activation energies. The same trend is also visible in Figure 58.

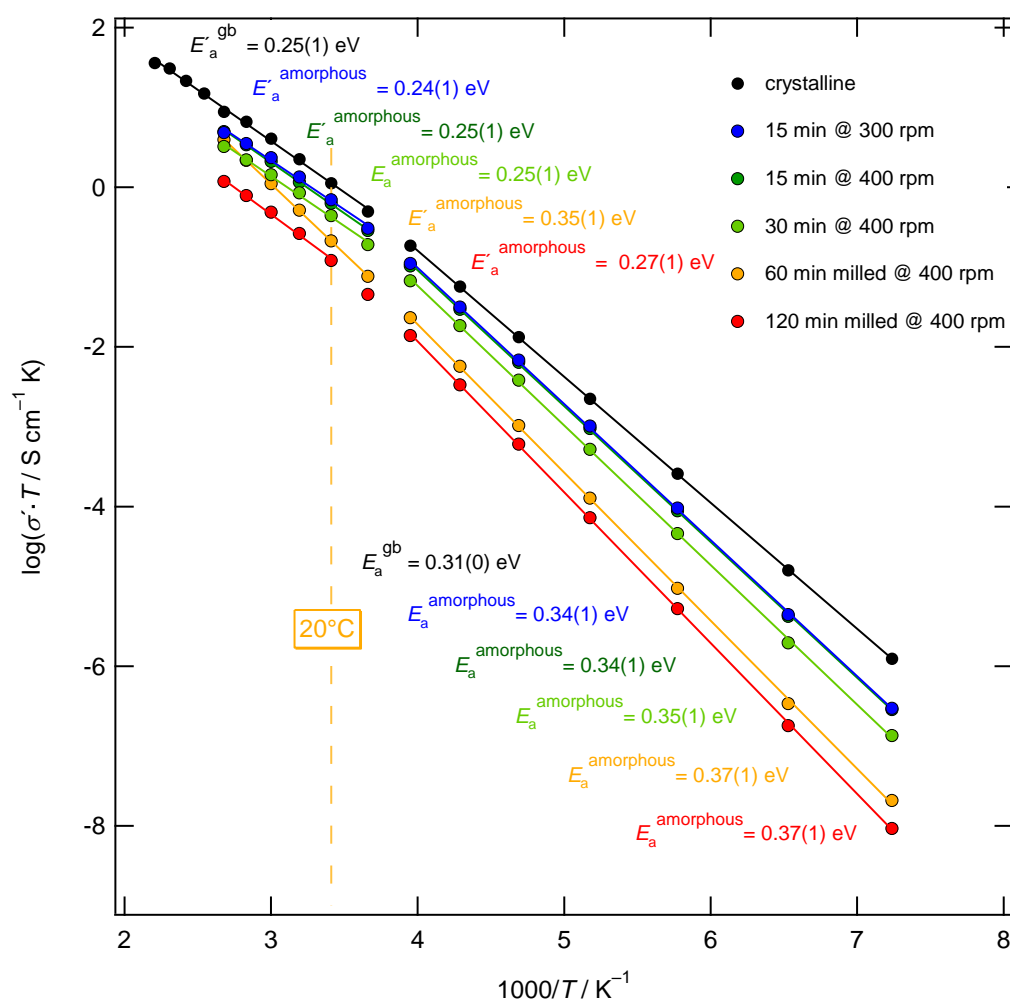


Figure 62: Arrhenius plot of the grain boundary or amorphous components of microcrystalline and ball milled $\text{Li}_{10}\text{GeP}_2\text{S}_{12}$ with the individual conductivity data obtained as σ_{DC}' from the isotherm plateaus.

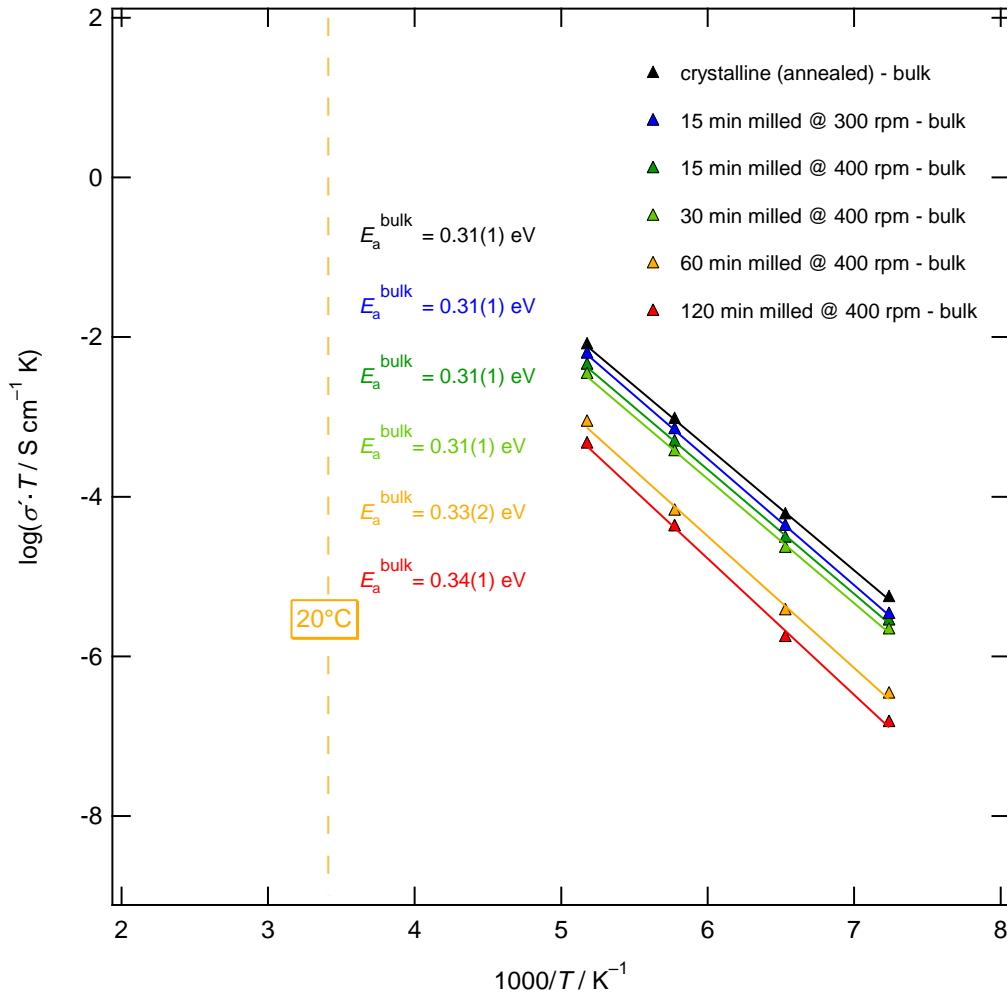


Figure 63: Arrhenius plot of the crystalline bulk components of microcrystalline and ball milled $\text{Li}_{10}\text{GeP}_2\text{S}_{12}$ with the individual conductivity data obtained as σ_{DC} from the isotherm plateaus.

Dawson and Islam originally proposed an improvement of the already remarkably high ionic conductivity of LGPS by reducing the crystallite size, arguing based on molecular dynamic simulations, that a distorted crystallite phase leads to a more isotropic conduction process and that under-coordination at the grain boundaries increases the mobility of Li ions.⁷⁴ The assumed structure consisted of nanosized crystallites, with no impurities and/or amorphous phases present. This idealized structure could not be reproduced by a single step ball milling procedure. Fortunately, by detailed analysis of the conductivity spectra, separation of the bulk and the grain boundary / amorphous contribution was achieved. This allowed validation of the theoretical work without having to reconstruct exactly the assumed idealized microstructure used for molecular dynamics simulations, excluding the degradation of the total conductivity due to the less conductive amorphous phase and considering only the (nano)crystalline bulk response. However, the conductivity of the isolated (nano)crystalline bulk was reduced as milling time and intensity was increased as can be clearly seen in Figure 63, contradicting the originally proposed improvement of the conductivity with reduction in grain size. Consequently, the theoretical work could not be confirmed experimentally. But it must be noted that the crystallite size leading to enhanced conductivity was in the range of 2-10 nm, and since crystallite size determination by XRD was only qualitative, it could not be stated if such small crystallites were obtained. Additionally, it is likely that by ball milling the defect density in the remaining crystallites was drastically increased, possibly impeding Li-ion migration.

Table 14: Results for the samples ball milled with different intensities and times. $\sigma_{20^\circ\text{C}}$ is the dc conductivity obtained from the isotherm plateaus. E_a^{bulk} is the (crystalline) bulk activation energy. The grain boundary / amorphous phase activation energy is divided into a low temperature regime with E_a^{gb} and a high temperature regime with E_a^{gb} . Capacitances obtained by equivalent circuit fitting are given for grain boundary / amorphous phase contributions C_{gb} and (crystalline) bulk contributions C_{bulk} at -135°C .

Samples	$\sigma_{20^\circ\text{C}} / \text{m S cm}^{-1}$	$E_a^{\text{bulk}} / \text{eV}$	$E_a^{\text{gb}} / \text{eV}$	$E_a^{\text{gb}} / \text{eV}$	$C_{\text{bulk}} @ 138 \text{ K} / \text{pF cm}^{-2}$	$C_{\text{gb}} @ 138 \text{ K} / \text{pF cm}^{-2}$
Microcrystalline (annealed)	3.89	0.31	0.31	0.25	18	410
15 min @ 300 rpm	2.37	0.31	0.34	0.24	13	140
15 min @ 400 rpm	2.15	0.31	0.34	0.25	11	98
30 min @ 400 rpm	1.50	0.31	0.35	0.25	-	74
60 min @ 400 rpm	0.72	0.33	0.37	0.35	-	15
120 min @ 400 rpm	0.41	0.34	0.37	0.27	-	10

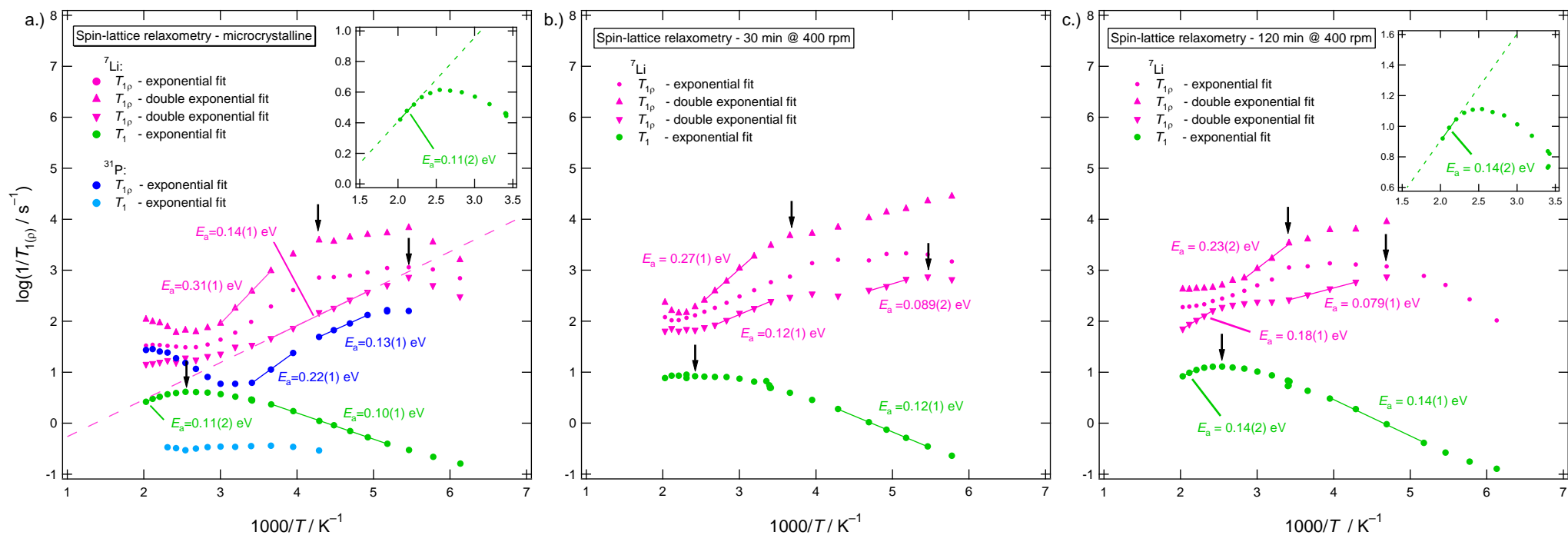


Figure 64: Arrhenius plots of the ${}^7\text{Li}$ (and ${}^{31}\text{P}$ in a.) T_1 and $T_{1\rho}$ spin-lattice relaxation rates of $\text{Li}_{10}\text{GeP}_2\text{S}_{12}$ a.) not milled (microcrystalline, see also Figure 45), b.) milled 30 min @ 400 rpm and c.) milled 120 min @ 400 rpm. Black arrow indicated peak maxima used for calculating the correlation time τ_c . Insets show the high temperature flank fit for ${}^7\text{Li}$ T_1 that would be hardly visible otherwise.

Figure 64 b.) and c.) show the Arrhenius plots obtained from ${}^7\text{Li}$ spin-lattice relaxometry (${}^{31}\text{P}$ relaxometry measurements were not performed) for the sample milled for 30 min @ 400 rpm and 120 min @ 400 rpm. The results for the crystalline LGPS sample were also added for easier comparison, see Figure 64 a.). The results of the milled samples in Figure 64 b.) and c.) had multiple similarities with the Arrhenius plot of crystalline LGPS in a.). The T_1 peak at about 120 °C is present in all three sample (although poorly visible in b.)) and the $T_{1\rho}$ magnetization transients allowed for a stretched double exponential fit in all samples. For the specimen milled 30 min @ 400 rpm, as seen in Figure 64 b.), four activation energies were deduced: 0.12(1) eV from the T_1 data and 0.27(1) eV, 0.12(1) eV and 0.089(2) eV from the $T_{1\rho}$ data. No high temperature slope was obtained from plotting the T_1 data. The activation energies of 0.27(1) eV and 0.12(1) eV fit well with the calculated activation energies for Li-ion migration in the c direction and the ab plane.⁵¹ This interpretation is the same as for not milled crystalline LGPS. The activation energy of 0.089(2) eV is very low and could not be ascribed to a particular migration process.

Similarly, for the sample milled for 120 min @ 400 rpm, $T_{1\rho}$ data yielded activation energies of 0.18(1) eV, 0.23(2) eV and 0.079(1) eV. The high temperature slope of the plotted T_1 data showed an activation energy of 0.14(2) eV. Again, the very low activation energy of 0.079(1) eV could not be ascribed to a particular process. The activation energies of 0.23(2) eV and 0.18(1) eV changed significantly compared to the other samples and are discussed further below. The activation energy obtained by the high temperature flank of the T_1^{-1} peak is very similar to the crystalline sample, albeit slightly higher. It is unknown why the sample milled 30 min did not exhibit a distinct peak, possibly a measurement error occurred.

The black arrows in Figure 64 indicate the estimated positions of the rate maxima which were used for calculating the correlation times listed in Table 15.

Table 15: Correlation times calculated from the maxima of the relaxation rate $1/T_{1(\rho)}$ of ${}^7\text{Li}$.

Sample	Experiment	Correlation time τ_c / s	T / K
	T_1	1.4×10^{-9}	413.15
30 min @ 400 rpm	$T_{1\rho} - 1$	4.0×10^{-6}	273.15
	$T_{1\rho} - 2$	4.0×10^{-6}	183.15
	T_1	1.4×10^{-9}	393.15
120 min @ 400 rpm	$T_{1\rho} - 1$	4.0×10^{-6}	293.15
	$T_{1\rho} - 2$	4.0×10^{-6}	213.15

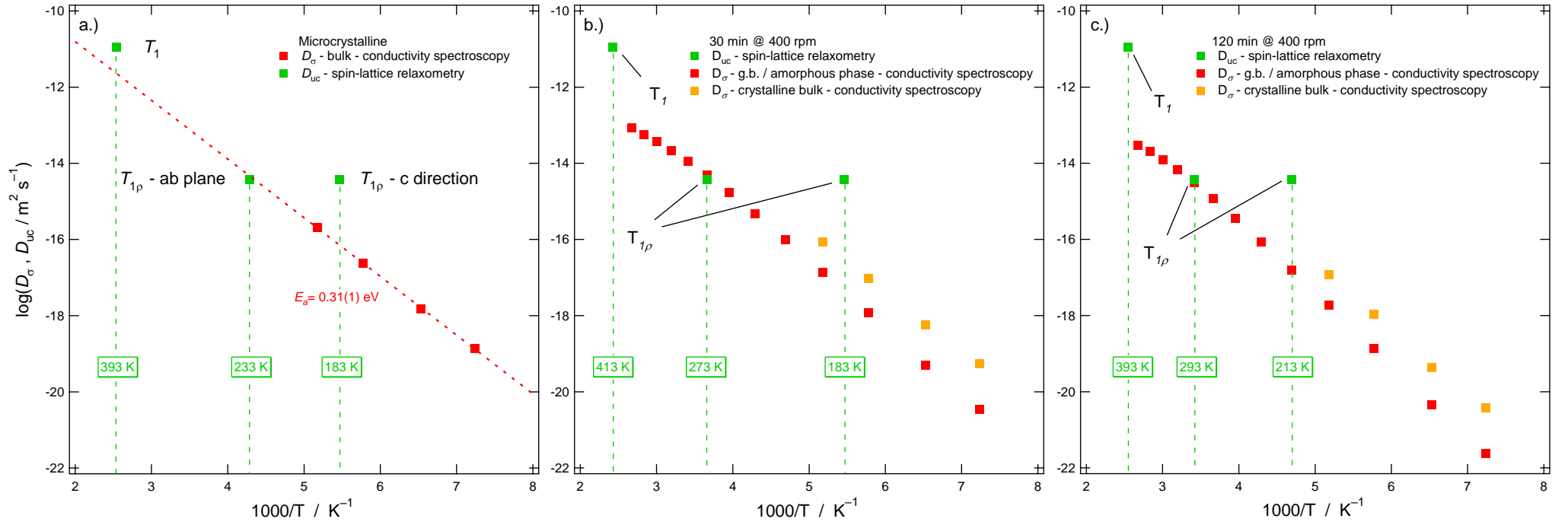


Figure 65: Arrhenius plots of the charge diffusion coefficient D_σ and uncorrelated diffusion coefficients D_{uc} obtained by conductivity and impedance spectroscopy and spin-lattice relaxometry. $Li_{10}GeP_2S_{12}$ a.) not milled (microcrystalline, see also Figure 46), b.) milled 30 min @ 400 rpm and c.) milled 120 min @ 400 rpm.

Insightful were again Arrhenius plots containing the charge diffusion coefficients calculated from conductivity spectroscopy data by equation 25 and the uncorrelated diffusion coefficients calculated from the (spin-lattice) correlation times by equation 35. The results are shown in Figure 65.

The T_1 peak did not shift significantly, and the general appearance of the peak was very similar in all three samples. The high temperature flanks were fitted, but no fit was possible for the sample milled 30 min @ 400 rpm and the flanks of the other samples were not completely resolved (measurements at even higher temperatures would be necessary). Consequently, the high temperature flanks should only be interpreted with care and the low temperature flanks were instead used for further analysis. The low temperature flanks yielded activation energies of 0.10(1) eV, 0.12(1) eV and 0.14(1) eV for the not milled, 30 min and 120 min milled samples, respectively. This indicated that in all three samples the same (or a similar) microscopic jump process is active, but that the activation energy associated with this process increased as milling progressed. This is insofar interesting as the sample milled 120 min @ 400 rpm consisted mainly of an amorphous phase (88 % amorphous /12 % crystalline) and therefore it is likely that the observed process is ascribable to the amorphous phase too. This would mean that crystalline and amorphous LGPS have a common microscopic jump process, however with the process having a higher activation energy in the distorted amorphous structure. Additionally, Figure 65 indicated that this process is either not the rate limiting step and/or does not contribute to long-range Li-ion migration in both crystalline and glassy LGPS.

Compared to T_1 , the Arrhenius plot obtained from the $T_{1\rho}$ data changed more significantly as the samples were ball milled. In crystalline LGPS the uncorrelated diffusion coefficient associated with the $T_{1\rho}$ peak at intermediate temperatures (middle arrow) matched well with the charge diffusion coefficients calculated from the conductivity data of the bulk. Similarly, in the milled samples the uncorrelated diffusion coefficients calculated from the peaks at intermediate temperatures (middle arrows) matched well with the charge diffusion coefficients related to the intergranular amorphous regions. This indicated that the corresponding processes with activation energies of 0.31(1) eV, 0.27(1) eV and 0.23(2) eV were the rate limiting steps responsible for long-range Li-ion migration. Also, the peaks shifted slightly to higher temperatures, indicative of a smaller jump frequency in the milled samples. For crystalline LGPS this process was assigned to the Li-ion migration in the ab plane based on the similarity to the theoretically calculated activation energy of 0.27 eV. As a reminder, the sample milled 30 min @ 400 rpm contained about 50 % amorphous phase and the sample milled 120 min @ 400 rpm about 88 % according to ^{31}P MAS NMR. And since the uncorrelated diffusion coefficient calculated coincide with the charge diffusion coefficients attributed to the (intergranular) amorphous regions, it was inferred that the process observed in NMR should also be attributed to the amorphous phase. The question now is if or how the limiting microscopic processes in the crystalline and glass phases are related. One possible explanation would be that the glassy phase continues to contain some structural features of the crystalline phase (amorphous phase formed by mechanical deformation of the crystalline phase) and the limiting process is equivalent to diffusion in the ab plane of LGPS. The disorder in the amorphous phase could then lower the activation barrier for this comparable unfavorable process, as the activation energy decreases with milling from 0.31(1) eV to 0.27(1) eV to 0.23(2) eV. Together with the increased activation energy of the process observed with T_1 spin-lattice relaxometry this indicated an increased isotropic nature of the Li-ion dynamics of samples milled longer.

Impedance spectroscopy yielded activation energies of 0.25(1) eV, 0.25(1) eV and 0.27(1) eV at elevated temperatures ($T > -20^{\circ}\text{C}$) and 0.31(1) eV, 0.35(1) eV and 0.37(1) eV at low temperatures ($T \leq -20^{\circ}\text{C}$) for the microcrystalline, 30 min and 120 min milled samples, respectively. All these values are listed in Table 16. This indicated an opposite trend (especially at lower temperatures), with increased activation energies with longer milling times, contradicting the previous attempt of explanation. Interesting is also that the $T_{1\rho}$ peak was located at 233 K for the microcrystalline, at 273 K for the 30 min and at 293 K for the 120 min milled sample. The activation energy for the microcrystalline sample at 233 K (-40°C) is 0.31(1) eV and fits well with the value of 0.31(1) eV from impedance spectroscopy. The values of 0.27(1) eV at 273 K (0°C) for the 30 min milled sample and 0.23(2) eV at 293 K (20°C) for the 120 min milled sample fit relatively well with the values of 0.25(1) eV and 0.27(1) eV obtained from impedance spectroscopy at elevated temperatures ($T \geq -20^{\circ}\text{C}$). Therefore, the change in activation energy followed by NMR could also originate from a possible change in Li-ion dynamics at around -20°C , see Figure 62. Consequently, since both effects, the change in Li-ion dynamics and the increased phase fraction of glassy LGPS overlapped and might influence each other, the origin on the change in activation energy cannot be deduced with certainty.

Table 16: Activation energies E_a obtained by $T_{1\rho}$ spin-lattice relaxometry (NMR) from the high temperature flanks of peaks (middle arrows in Figure 64) at temperatures T_{peak} and low (E_a , $T < -20^{\circ}\text{C}$) and high temperature (E_a' , $T \geq -20^{\circ}\text{C}$) activation energies obtained by impedance spectroscopy (IS).

Sample	E_a (NMR) / eV	T_{peak} / K	E_a (IS) / eV	E_a' (IS) / eV
Microcrystalline	0.31(1)	233	0.31(1)	0.25(1)
30 min @ 400 rpm	0.27(1)	273	0.35(1)	0.25(1)
120 min @ 400 rpm	0.23(2)	293	0.37(1)	0.27(1)

In the end it should be noted that this was only a tentative attempt to explain the present data, but further investigations would be needed to obtain a conclusive statement. Especially the results from $T_{1\rho}$ spin-lattice relaxometry were ambiguous as many activation energies could be obtained. Often it could not be clearly stated if a process appeared to shift in temperature or a new process increased in signal intensity with others decreasing. Also, the samples at hand contain amorphous and crystalline components and the individual contribution might overlap and mask each other.

5 Conclusion

$\text{Li}_{10}\text{GeP}_2\text{S}_{12}$ and its derivative $\text{Li}_{10}\text{GeP}_2\text{S}_{12-x}\text{O}_x$ are very promising solid electrolytes with a remarkable high ionic conductivity of up to 12 mS cm^{-1} , rivaling that of organic, liquid electrolytes. Theoretical work suggests the possibility for further enhancement by reducing the crystallite size down to the nanometer scale (2-10 nm).

Both $\text{Li}_{10}\text{GeP}_2\text{S}_{12}$ and $\text{Li}_{10}\text{GeP}_2\text{S}_{11.7}\text{O}_{0.3}$ were synthesized by a solid-state route and structurally characterized by XRD, ^{31}P , ^7Li and ^6Li MAS NMR, and Raman spectroscopy. $\text{Li}_{10}\text{GeP}_2\text{S}_{12}$ could unambiguously be identified and the presence of $\approx 16 \text{ wt\%}$ orthorhombic side phase $\beta\text{-Li}_3\text{PS}_4$ was confirmed. However, no significant structural difference could be found between oxygen substituted $\text{Li}_{10}\text{GeP}_2\text{S}_{11.7}\text{O}_{0.3}$ and $\text{Li}_{10}\text{GeP}_2\text{S}_{12}$. Oxygen seemed to be present also in minor quantities in conventional $\text{Li}_{10}\text{GeP}_2\text{S}_{12}$, indicating impurities either from the starting materials or from the environment during synthesis.

The Li-ion dynamics were probed by impedance and conductivity spectroscopy as well as by ^7Li and ^{31}P NMR spin-lattice relaxometry. The ionic conductivity of $\text{Li}_{10}\text{GeP}_2\text{S}_{12}$ was determined to be 4 mS cm^{-1} with an activation energy of 0.31 eV at low ($\leq -20 \text{ }^\circ\text{C}$) and 0.25 eV at elevated ($> -20 \text{ }^\circ\text{C}$) temperatures. The grain boundary and bulk contributions could be separated at low temperatures using the electric modulus formalism and equivalent circuit fitting and both exhibited an activation energy of about 0.31 eV. Activation energies of 0.14 eV and 0.31 eV obtained by ^7Li spin-lattice relaxometry matched well with the calculated activation energies reported in literature for Li-ion migration along the c direction and the ab plane of 0.17 eV and 0.28 eV. ^{31}P spin-lattice relaxometry agrees well with the results from ^7Li . The microscopic (relaxometry) and macroscopic (impedance) results for ion dynamics are indicative of long-range Li-ion migration involving both atomic jumps in c direction and in the ab plane, with the latter being the rate limiting step.

$\text{Li}_{10}\text{GeP}_2\text{S}_{12}$ was nanostructured by mechanical ball milling. With increasing milling time and speed, a decrease in ionic conductivity and increase in activation energy could be observed. Line broadening observed in XRD revealed that a reduction in crystallite size was achieved, but at the expense of an increasing amount of amorphous phase detected by ^{31}P MAS NMR. After milling for 120 min at 400 rpm, the crystallite size seemed to be reduced significantly, but the amorphous phase fraction amounted to 88 wt%. The ion dynamics were again probed by impedance / conductivity spectroscopy and ^7Li spin-lattice relaxometry. The crystalline and amorphous contributions could still be differentiated by the modulus formalism and a model is proposed in which the crystallites are separated, instead of well-defined grain boundaries, by an amorphous intergranular region, similar to a core-shell structure or a glass-ceramic. It was also revealed that not only the presence of amorphous material led to a decrease in ionic conductivity, but that also the crystallites themselves exhibit worse conductivity. Most interestingly, T_1 relaxometry showed that the same microscopic jump process is active in both crystalline and glassy $\text{Li}_{10}\text{GeP}_2\text{S}_{12}$, but with the corresponding activation energy continuously increasing with prolonged milling. $T_{1\rho}$ data, although suggesting another process with reduced activation energy and a more isotropic Li-ion migration as the samples were ball milled, was not unambiguously conclusive.

Concluding, nanostructured $\text{Li}_{10}\text{GeP}_2\text{S}_{12}$ without amorphous phase, as assumed in the underlying theoretical work, could not be synthesized by means of simple mechanical ball milling. Additionally, it could not be confirmed that crystallites with reduced size exhibit better ionic conductivity in the superionic conductor $\text{Li}_{10}\text{GeP}_2\text{S}_{12}$.

6 Outlook

$\text{Li}_{10}\text{GeP}_2\text{S}_{12}$ is a promising material and since its discovery in 2011 considerable research effort brought new insights into its structure and ion dynamics. Yet, many aspects of the Li-ion dynamics still remain unknown, for example the origin of the change in activation energy at elevated temperatures, the proper connection of long-range ionic transport and microscopic jumps / diffusion pathways and if all Li sites participate in the conduction process. Especially NMR could enable exact elucidation of the mechanisms involved in Li-ion migration in $\text{Li}_{10}\text{GeP}_2\text{S}_{12}$. Understanding these phenomena is an important step and basis for continuous improvement of the ionic conductivity of LGPS-related materials.

Despite no experimental evidence being found for enhanced conductivity by crystallite size reduction, this direction of development still remains an open avenue for the improvement of $\text{Li}_{10}\text{GeP}_2\text{S}_{12}$. Solely mechanical ball milling results in considerable amounts of amorphous phase and will probably not lead to the desired nanostructure. Additionally, significant changes in conductivity were only reported for crystallites smaller than 10 nm, a size regime not easily obtainable. However, combination with annealing steps could result in a highly crystallite material with nanometer sized grains, particularly with the sluggish grain growth reported for $\text{Li}_{10}\text{GeP}_2\text{S}_{12}$. Another alternative might be the direct formation of nanocrystallites by a liquid phase synthesis route. This kind of research is still in its infancy stage but has nevertheless great potential. And certainly, the concept of nanostructuring can be applied not only to $\text{Li}_{10}\text{GeP}_2\text{S}_{12}$, but to all members of the LGPS family. The compositional space for LGPS related phases still poses many opportunities for discovering new materials, which might be more suitable for nanostructuring.

7 References

1. Amine, K., Kanno, R. & Tzeng, Y. Rechargeable lithium batteries and beyond: Progress, challenges, and future directions. *MRS Bull.* **39**, 395–401 (2014).
2. Deng, D. Li-ion batteries: Basics, progress, and challenges. *Energy Sci. Eng.* **3**, 385–418 (2015).
3. Winter, M., Besenhard, J. O., Spahr, M. E. & Novák, P. Electrode materials for rechargeable lithium batteries. *Adv. Mater.* **10**, 725–763 (1998).
4. Manthiram, A. Materials Aspects: An Overview. in *Lithium Batteries Science and Technology* (ed. Nazri, Gholam-Abbas; Pistoia, G.) 3–41 (Springer US, 2003).
5. Goodenough, J. B. & Park, K. S. The Li-ion rechargeable battery: A perspective. *J. Am. Chem. Soc.* **135**, 1167–1176 (2013).
6. Janek, J. & Zeier, W. G. A solid future for battery development. *Nat. Energy* **1**, 16141 (2016).
7. Armand, M. & Tarascon, J. M. Building better batteries. *Nature* vol. 451 652–657 (2008).
8. Jung, K. N., Shin, H. S., Park, M. S. & Lee, J. W. Solid-State Lithium Batteries: Bipolar Design, Fabrication, and Electrochemistry. *ChemElectroChem* **6**, 3842–3859 (2019).
9. Yao, X. et al. All-solid-state lithium batteries with inorganic solid electrolytes: Review of fundamental science. *Chinese Phys. B* **25**, 018802–018815 (2016).
10. Zheng, F., Kotobuki, M., Song, S., Lai, M. O. & Lu, L. Review on solid electrolytes for all-solid-state lithium-ion batteries. *J. Power Sources* **389**, 198–213 (2018).
11. Wu Li, J. R. Dahn, D. S. W. Rechargeable Lithium Batteries with Aqueous Electrolytes. *Science (80-.)*. **264**, 1115–1118 (1994).
12. Thangadurai, V., Narayanan, S. & Pinzaru, D. Garnet-type solid-state fast Li ion conductors for Li batteries: Critical review. *Chem. Soc. Rev.* **43**, 4714–4727 (2014).
13. Kamaya, N. et al. A lithium superionic conductor. *Nat. Mater.* **10**, 682–686 (2011).
14. Richards, W. D., Miara, L. J., Wang, Y., Kim, J. C. & Ceder, G. Interface Stability in Solid-State Batteries. *Chem. Mater.* **28**, 266–273 (2016).
15. Famprakis, T., Canepa, P., Dawson, J. A., Islam, M. S. & Masquelier, C. Fundamentals of inorganic solid-state electrolytes for batteries. *Nat. Mater.* **18**, 1278–1291 (2019).
16. Kasemchainan, J. et al. Critical stripping current leads to dendrite formation on plating in lithium anode solid electrolyte cells. *Nat. Mater.* **18**, 1105–1111 (2019).
17. Zhu, Y., He, X. & Mo, Y. Origin of Outstanding Stability in the Lithium Solid Electrolyte Materials: Insights from Thermodynamic Analyses Based on First-Principles Calculations. *ACS Appl. Mater. Interfaces* **7**, 23685–23693 (2015).
18. Goodenough, J. B. Crystalline solid electrolytes II: Material design. in *Solid State Electrochemistry* (ed. Bruce, P. G.) 360 (Cambridge University Press, 1995).
19. Goodenough, J. B. & Kim, Y. Challenges for rechargeable Li batteries. *Chem. Mater.* **22**, 587–603 (2010).
20. Yu, S. et al. Elastic Properties of the Solid Electrolyte Li₇La₃Zr₂O₁₂ (LLZO). *Chem. Mater.* **28**, 197–206 (2016).
21. Sakuda, A., Hayashi, A. & Tatsumisago, M. Sulfide solid electrolyte with favorable mechanical property for all-solid-state lithium battery. *Sci. Rep.* **3**, 1–5 (2013).

22. Kanno, R. & Murayama, M. Lithium Ionic Conductor Thio-LISICON: The $\text{Li}_2\text{S-GeS}_2\text{-P}_2\text{S}_5$ System. *J. Electrochem. Soc.* **148**, A742–A746 (2001).
23. Fergus, J. W. Ceramic and polymeric solid electrolytes for lithium-ion batteries. *J. Power Sources* **195**, 4554–4569 (2010).
24. Manuel Stephan, A. & Nahm, K. S. Review on composite polymer electrolytes for lithium batteries. *Polymer (Guildf)*. **47**, 5952–5964 (2006).
25. Porz, L. et al. Mechanism of Lithium Metal Penetration through Inorganic Solid Electrolytes. *Adv. Energy Mater.* **7**, 1701003 (2017).
26. Samson, A. J., Hofstetter, K., Bag, S. & Thangadurai, V. A bird's-eye view of Li-stuffed garnet-type $\text{Li}_7\text{La}_3\text{Zr}_2\text{O}_{12}$ ceramic electrolytes for advanced all-solid-state Li batteries. *Energy Environ. Sci.* **12**, 2957–2975 (2019).
27. Shannon, R. D. Revised Effective Ionic Radii and Systematic Studies of Interatomic Distances in Halides and Chalcogenides. *Acta Crystallogr. Sect. A* **32**, 751–767 (1976).
28. Dimitrov, V. & Komatsu, T. Correlation among electronegativity, cation polarizability, optical basicity and single bond strength of simple oxides. *J. Solid State Chem.* **196**, 574–578 (2012).
29. West, A. R. Crystalline solid electrolytes I: General considerations and the major materials. in *Solid State Electrochemistry* (ed. Bruce, P. G.) 360 (Cambridge University Press, 1995).
30. Lau, J. et al. Sulfide Solid Electrolytes for Lithium Battery Applications. *Adv. Energy Mater.* **8**, 1800933 (2018).
31. Dawson, J. A. et al. Toward Understanding the Different Influences of Grain Boundaries on Ion Transport in Sulfide and Oxide Solid Electrolytes. *Chem. Mater.* **31**, 5296–5304 (2019).
32. Han, F., Zhu, Y., He, X., Mo, Y. & Wang, C. Electrochemical Stability of $\text{Li}_{10}\text{GeP}_2\text{S}_{12}$ and $\text{Li}_7\text{La}_3\text{Zr}_2\text{O}_{12}$ Solid Electrolytes. *Adv. Energy Mater.* **6**, 1501590 (2016).
33. Troy, S. et al. Life Cycle Assessment and resource analysis of all-solid-state batteries. *Appl. Energy* **169**, 757–767 (2016).
34. Muramatsu, H., Hayashi, A., Ohtomo, T., Hama, S. & Tatsumisago, M. Structural change of $\text{Li}_2\text{S-P}_2\text{S}_5$ sulfide solid electrolytes in the atmosphere. *Solid State Ionics* **182**, 116–119 (2011).
35. Miura, A. et al. Liquid-phase syntheses of sulfide electrolytes for all-solid-state lithium battery. *Nat. Rev. Chem.* **3**, 189–198 (2019).
36. Kanno, R., Hata, T., Kawamoto, Y. & Irie, M. Synthesis of a new lithium ionic conductor, thio-LISICON-lithium germanium sulfide system. *Solid State Ionics* **130**, 97–104 (2000).
37. Murayama, M. et al. Synthesis of new lithium ionic conductor thio-LISICON - Lithium silicon sulfides system. *J. Solid State Chem.* **168**, 140–148 (2002).
38. Kato, Y., Hori, S. & Kanno, R. $\text{Li}_{10}\text{GeP}_2\text{S}_{12}$ -Type Superionic Conductors: Synthesis, Structure, and Ionic Transportation. *Adv. Energy Mater.* **10**, 2002153 (2020).
39. Murayama, M., Kanno, R., Kawamoto, Y. & Kamiyama, T. Structure of the thio-LISICON, Li_4GeS_4 . *Solid State Ionics* **154–155**, 789–794 (2002).
40. Hori, S. et al. Phase Diagram of the $\text{Li}_4\text{GeS}_4\text{-Li}_3\text{PS}_4$ Quasi-Binary System Containing the Superionic Conductor $\text{Li}_{10}\text{GeP}_2\text{S}_{12}$. *J. Am. Ceram. Soc.* **98**, 3352–3360 (2015).
41. Homma, K. et al. Crystal structure and phase transitions of the lithium ionic conductor Li_3PS_4 . *Solid State Ionics* **182**, 53–58 (2011).
42. Liu, Z. et al. Anomalous high ionic conductivity of nanoporous $\beta\text{-Li}_3\text{PS}_4$. *J. Am. Chem. Soc.* **135**, 975–978 (2013).

43. Tachez, M., Malugani, J. P., Mercier, R. & Robert, G. Ionic conductivity of and phase transition in lithium thiophosphate Li_3PS_4 . *Solid State Ionics* **14**, 181–185 (1984).
44. Liang, X. et al. New $\text{Li}_{10}\text{GeP}_2\text{S}_{12}$ Structure Ordering and Li-Ion Dynamics Unveiled in Li_4GeS_4 - Li_3PS_4 Superionic Conductors: A Solid-State Nuclear Magnetic Resonance Study. *ACS Appl. Mater. Interfaces* **12**, 27029–27036 (2020).
45. Kwon, O. et al. Synthesis, structure, and conduction mechanism of the lithium superionic conductor $\text{Li}_{10+\delta}\text{Ge}_{1+\delta}\text{P}_{2-\delta}\text{S}_{12}$. *J. Mater. Chem. A* **3**, 438–446 (2015).
46. Sun, Y. et al. Oxygen substitution effects in $\text{Li}_{10}\text{GeP}_2\text{S}_{12}$ solid electrolyte. *J. Power Sources* **324**, 798–803 (2016).
47. Kuhn, A., Köhler, J. & Lotsch, B. V. Single-crystal X-ray structure analysis of the superionic conductor $\text{Li}_{10}\text{GeP}_2\text{S}_{12}$. *Phys. Chem. Chem. Phys.* **15**, 11620–11622 (2013).
48. Iwasaki, R. et al. Weak Anisotropic Lithium-Ion Conductivity in Single Crystals of $\text{Li}_{10}\text{GeP}_2\text{S}_{12}$. *Chem. Mater.* **31**, 3694–3699 (2019).
49. Suzuki, K. et al. Precipitation of the Lithium Superionic Conductor $\text{Li}_{10}\text{GeP}_2\text{S}_{12}$ by a Liquid-Phase Process. *Chem. Lett.* **49**, 1379–1381 (2020).
50. Tsukasaki, H., Mori, S., Shiotani, S., Yamamura, H. & Iba, H. Direct observation of a non-isothermal crystallization process in precursor $\text{Li}_{10}\text{GeP}_2\text{S}_{12}$ glass electrolyte. *J. Power Sources* **369**, 57–64 (2017).
51. Mo, Y., Ong, S. P. & Ceder, G. First principles study of the $\text{Li}_{10}\text{GeP}_2\text{S}_{12}$ lithium super ionic conductor material. *Chem. Mater.* **24**, 15–17 (2012).
52. Du, F., Ren, X., Yang, J., Liu, J. & Zhang, W. Structures, thermodynamics, and Li^+ mobility of $\text{Li}_{10}\text{GeP}_2\text{S}_{12}$: A first-principles analysis. *J. Phys. Chem. C* **118**, 10590–10595 (2014).
53. Kwon, O. et al. Synthesis, structure, and conduction mechanism of the lithium superionic conductor $\text{Li}_{10+\delta}\text{Ge}_{1+\delta}\text{P}_{2-\delta}\text{S}_{12}$. *J. Mater. Chem. A* **3**, 438–446 (2015).
54. Ong, S. P. et al. Phase stability, electrochemical stability and ionic conductivity of the $\text{Li}_{10\pm 1}\text{MP}_2\text{X}_{12}$ ($\text{M} = \text{Ge, Si, Sn, Al}$ or P , and $\text{X} = \text{O, S}$ or Se) family of superionic conductors. *Energy Environ. Sci.* **6**, 148–156 (2013).
55. Kuhn, A. et al. A new ultrafast superionic Li-conductor: Ion dynamics in $\text{Li}_{11}\text{Si}_2\text{PS}_{12}$ and comparison with other tetragonal LGPS-type electrolytes. *Phys. Chem. Chem. Phys.* **16**, 14669–14674 (2014).
56. Bron, P. et al. $\text{Li}_{10}\text{SnP}_2\text{S}_{12}$: An affordable lithium superionic conductor. *J. Am. Chem. Soc.* **135**, 15694–15697 (2013).
57. Kato, Y. et al. High-power all-solid-state batteries using sulfide superionic conductors. *Nat. Energy* **1**, 16030 (2016).
58. Wang, Y., Liu, Z., Zhu, X., Tang, Y. & Huang, F. Highly lithium-ion conductive thio-LISICON thin film processed by low-temperature solution method. *J. Power Sources* **224**, 225–229 (2013).
59. Kuhn, A., Duppel, V. & Lotsch, B. V. Tetragonal $\text{Li}_{10}\text{GeP}_2\text{S}_{12}$ and Li_7GePS_8 -exploring the Li ion dynamics in LGPS Li electrolytes. *Energy Environ. Sci.* **6**, 3548–3552 (2013).
60. Hayashi, D. et al. Synthesis of $\text{Li}_{10}\text{GeP}_2\text{S}_{12}$ -type lithium superionic conductors under Ar gas flow. *J. Power Sources* **473**, 228524 (2020).
61. Kim, K. H. & Martin, S. W. Structures and Properties of Oxygen-Substituted $\text{Li}_{10}\text{SiP}_2\text{S}_{12-x}\text{O}_x$ Solid-State Electrolytes. *Chem. Mater.* **31**, 3984–3991 (2019).

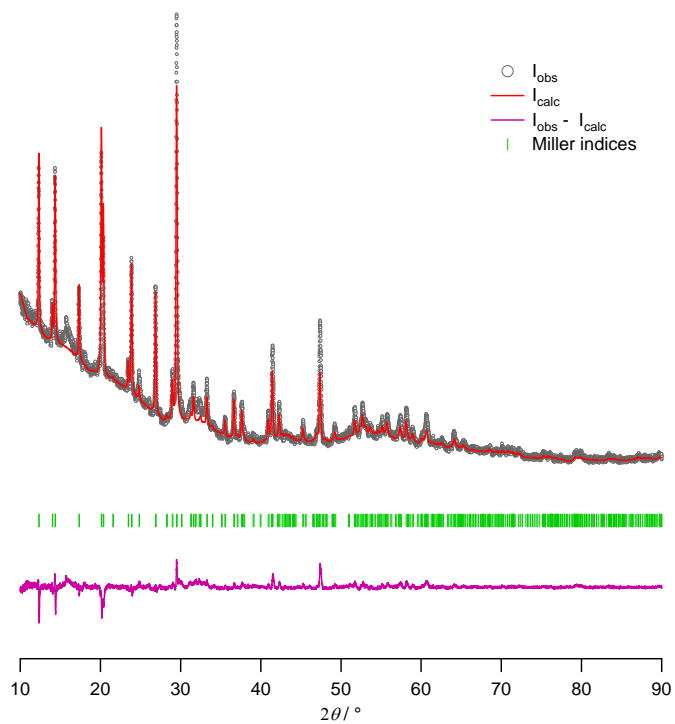
62. Adams, S. & Prasada Rao, R. Structural requirements for fast lithium ion migration in $\text{Li}_{10}\text{GeP}_2\text{S}_{12}$. *J. Mater. Chem.* **22**, 7687–7691 (2012).
63. Weber, D. A. et al. Structural Insights and 3D Diffusion Pathways within the Lithium Superionic Conductor $\text{Li}_{10}\text{GeP}_2\text{S}_{12}$. *Chem. Mater.* **28**, 5905–5915 (2016).
64. Liang, X. et al. In-Channel and In-Plane Li Ion Diffusions in the Superionic Conductor $\text{Li}_{10}\text{GeP}_2\text{S}_{12}$ Probed by Solid-State NMR. *Chem. Mater.* **27**, 5503–5510 (2015).
65. Hu, C. H., Wang, Z. Q., Sun, Z. Y. & Ouyang, C. Y. Insights into structural stability and Li superionic conductivity of $\text{Li}_{10}\text{GeP}_2\text{S}_{12}$ from first-principles calculations. *Chem. Phys. Lett.* **591**, 16–20 (2014).
66. Wang, Y. et al. Design principles for solid-state lithium superionic conductors. *Nat. Mater.* **14**, 1026–1032 (2015).
67. Xu, M., Ding, J. & Ma, E. One-dimensional stringlike cooperative migration of lithium ions in an ultrafast ionic conductor. *Appl. Phys. Lett.* **101**, 031901 (2012).
68. Malik, R., Burch, D., Bazant, M. & Ceder, G. Particle size dependence of the ionic diffusivity. *Nano Lett.* **10**, 4123–4127 (2010).
69. Chadwick, A. V. . High-temperature transport in fluorites. *Solid State Ionics* **8**, 209–220 (1983).
70. Bron, P., Dehnen, S. & Roling, B. $\text{Li}_{10}\text{Si}_{0.3}\text{Sn}_{0.7}\text{P}_2\text{S}_{12}$ – A low-cost and low-grain-boundary-resistance lithium superionic conductor. *J. Power Sources* **329**, 530–535 (2016).
71. Jansen, M. Volume Effect or Paddle-Wheel Mechanism—Fast Alkali-Metal Ionic Conduction in Solids with Rotationally Disordered Complex Anions. *Angew. Chemie Int. Ed. English* **30**, 1547–1558 (1991).
72. Hassoun, J. et al. A structural, spectroscopic and electrochemical study of a lithium ion conducting $\text{Li}_{10}\text{GeP}_2\text{S}_{12}$ solid electrolyte. *J. Power Sources* **229**, 117–122 (2013).
73. Krauskopf, T., Culver, S. P. & Zeier, W. G. Bottleneck of Diffusion and Inductive Effects in $\text{Li}_{10}\text{Ge}_{1-x}\text{Sn}_x\text{P}_2\text{S}_{12}$. *Chem. Mater.* **30**, 1791–1798 (2018).
74. Dawson, J. A. & Islam, M. S. Enhanced Li-Ion Conductivity in Nanosized $\text{Li}_{10}\text{GeP}_2\text{S}_{12}$. *ECS Meet. Abstr.* **MA2020-02**, 871 (2020).
75. Rogers, B., Pennathur, S. & Adams, J. *Nanotechnology: Understanding Small Systems*. (CRC Press Taylor & Francis Group, 2015).
76. Maier, J. Nanoionics: ion transport and electrochemical storage in confined systems. *Nat. Mater.* **4**, 805–815 (2005).
77. Tuller, H. L. Ionic conduction in nanocrystalline materials. *Solid State Ionics* **131**, 143–157 (2000).
78. Brinek, M., Hiebl, C. & Wilkening, H. M. R. Understanding the Origin of Enhanced Li-Ion Transport in Nanocrystalline Argyrodite-Type $\text{Li}_6\text{PS}_5\text{I}$. *Chem. Mater.* **32**, 4754–4766 (2020).
79. Hori, S. et al. Synthesis, structure, and ionic conductivity of solid solution, $\text{Li}_{10+\delta}\text{M}_{1+\delta}\text{P}_{2-\delta}\text{S}_{12}$ (M = Si, Sn). *Faraday Discuss.* **176**, 83–94 (2014).
80. Inagaki, M. et al. Conduction Mechanism of $\text{Li}_{10}\text{GeP}_2\text{S}_{12}$ -type Lithium Superionic Conductors in a Li-Sn-Si-P-S System. *Chem. Mater.* **31**, 3485–3490 (2019).
81. Tsukasaki, H., Mori, S., Morimoto, H., Hayashi, A. & Tatsumisago, M. Direct observation of a non-crystalline state of $\text{Li}_2\text{S-P}_2\text{S}_5$ solid electrolytes. *Sci. Rep.* **7**, 4142 (2017).

82. Sakuma, M., Suzuki, K., Hirayama, M. & Kanno, R. Reactions at the electrode/electrolyte interface of all-solid-state lithium batteries incorporating Li-M (M = Sn, Si) alloy electrodes and sulfide-based solid electrolytes. *Solid State Ionics* **285**, 101–105 (2016).
83. Wenzel, S. et al. Direct Observation of the Interfacial Instability of the Fast Ionic Conductor $\text{Li}_{10}\text{GeP}_2\text{S}_{12}$ at the Lithium Metal Anode. *Chem. Mater.* **28**, 2400–2407 (2016).
84. Smart, L. E. & Moore, E. A. *Solid State Chemistry An Introduction*. (CRC Press Taylor & Francis Group, 2012).
85. West, A. R. *Solid State Chemistry and its Applications*. (John Wiley & Sons, Ltd, 2014).
86. Cullity, B. D. & Stock, S. R. *Elements of X-ray Diffraction*. (Pearson Education Limited Edinburgh, 2014).
87. Callister, W. D. & Rethwisch, D. G. *Materials Science and Engineering An Introduction*. (John Wiley & Sons, Inc., 2010).
88. Yang, L. *Materials Characterization Introduction to Microscopic and Spectroscopic Methods*. (Wiley-VCH Verlag GmbH & Co., 2013).
89. Hammond, C. *The Basics of Crystallography and Diffraction*. (Oxford University Press Inc., 2009).
90. Birkholz, M. *Thin Film Analysis by X-Ray Scattering*. (Wiley-VCH Verlag GmbH & Co. KGaA, 2006).
91. McCusker, L. B., Von Dreele, R. B., Cox, D. E., Louer, D. & Scardi, P. Rietveld refinement guidelines. *J. Appl. Crystallogr.* **32**, 36–50 (1999).
92. Toby, B. H. R factors in Rietveld analysis: How good is good enough? . *Powder Diffr.* **21**, 67–70 (2006).
93. Albert, B. Diffraction Methods: Structure Determination and Phase Analysis of Solids. in *Methods in Physical Chemistry Volume I* (eds. Schäfer, R. & Schmidt, P. C.) 271–296 (Wiley-VCH Verlag GmbH & Co. KGaA., 2012).
94. Habasaki, J., Len, C. & Ngai, K. L. *Dynamics of Glassy, Crystalline and Liquid Ionic Conductors. Experiment, Theories, Simulations*. (Springer Nature, 2017).
95. Macdonald, J. R. & Johnson, W. B. Fundamentals of Impedance Spectroscopy. in *Impedance Spectroscopy Theory, Experiment, and Applications* (eds. Barsoukov, E. & Macdonald, J. R.) 1–21 (John Wiley & Sons, Inc., 2018).
96. Feynman, R. P., Leighton, R. B. & Sands, M. *The Feynman Lectures on Physics Volume I Mainly Mechanics, Radiation, and Heat*. (Basic Books, 2010).
97. Feynman, R. P., Leighton, R. B. & Sands, M. *The Feynman Lectures on Physics Volume II Mainly Electromagnetism and Matter*. (Basic Books, 2010).
98. Mehrer, H. *Diffusion in Solids Fundamentals, Methods, Materials, Diffusion-Controlled Processes*. (Springer-Verlag Berlin Heidelberg, 2007).
99. Irvine, J. T. S., Sinclair, D. C. & West, A. R. Electroceramics: Characterization by Impedance Spectroscopy. *Adv. Mater.* **2**, 132–138 (1990).
100. Brunklaus, G., Spiess, H. W. & Eckert, H. Solid State NMR: a Versatile Tool in Solid State Chemistry and Materials Science. in *Methods in Physical Chemistry Volume I* (eds. Schäfer, R. & Schmidt, P. C.) 87–158 (Wiley-VCH Verlag GmbH & Co. KGaA., 2012).
101. Wedler, G. *Lehrbuch der Physikalischen Chemie*. (WILEY-YCH Verlag GmbH Co. KGaA, 2004).

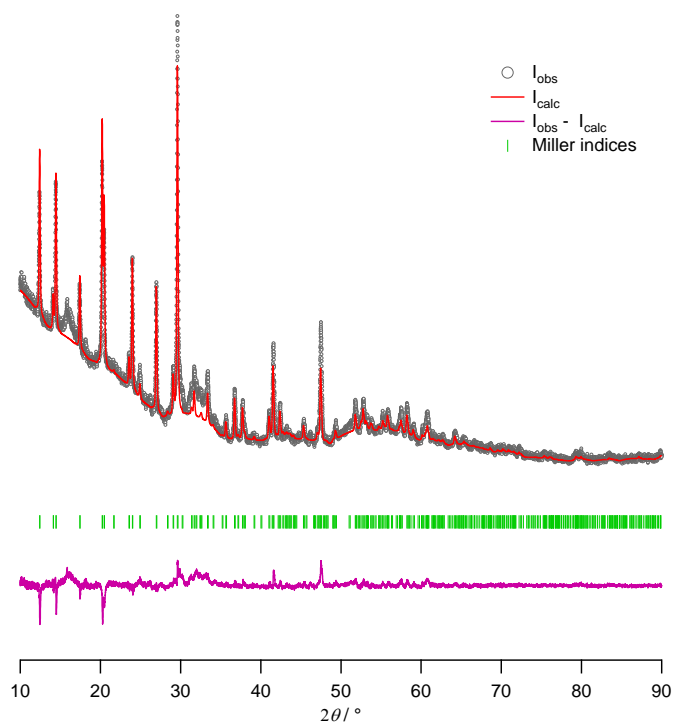
102. Duer, M. J. Essential Techniques for Spin-1/2 Nuclei. in *Solid-State NMR Spectroscopy Principles and Applications* (ed. Duer, M. J.) 73–110 (Blackwell Science Ltd, 2002).
103. Duer, M. J. The Basics of Solid-State NMR. in *Solid-State NMR Spectroscopy Principles and Applications* (ed. Duer, M. J.) 3–72 (Blackwell Science Ltd, 2002).
104. Mariani, M. M. & Deckert, V. Raman Spectroscopy: Principles, Benefits, and Applications. in *Methods in Physical Chemistry Volume II* (eds. Schäfer, R. & Schmidt, P. C.) 421–444 (Wiley-VCH Verlag & Co. KGaA, 2012).
105. Eckert, H., Zhang, Z. & Kennedy, J. H. Structural Transformation of Non-Oxide Chalcogenide Glasses. The Short-Range Order of Li₂S-P₂S₅ Glasses Studied by Quantitative ³¹P and ^{6,7}Li High-Resolution Solid-State NMR. *Chem. Mater.* **2**, 273–279 (1990).
106. Stöffler, H. et al. Amorphous versus Crystalline Li₃PS₄: Local Structural Changes during Synthesis and Li Ion Mobility. *J. Phys. Chem. C* **123**, 10280–10290 (2019).
107. Hayashi, A., Tatsumisago, M. & Minami, T. Crystallization process of lithium oxysulfide glasses. *J. Non. Cryst. Solids* **276**, 27–34 (2000).
108. Minami, K., Mizuno, F., Hayashi, A. & Tatsumisago, M. Structure and properties of the 70Li₂S·(30-x)P₂S₅·x P₂O₅ oxy- sulfide glasses and glass-ceramics. *J. Non. Cryst. Solids* **354**, 370–373 (2008).
109. Zheng, J., Wang, P., Liu, H. & Hu, Y. Y. Interface-Enabled Ion Conduction in Li₁₀GeP₂S₁₂-Poly(ethylene Oxide) Hybrid Electrolytes. *ACS Appl. Energy Mater.* **2**, 1452–1459 (2019).
110. Heitjans, P., Indris, S. & Wilkening, M. Solid-State Diffusion and NMR. *Diffus. Fundam.* **2**, 45.1-45.20 (2005).
111. Serghei, A., Tress, M., Sangoro, J. R. & Kremer, F. Electrode polarization and charge transport at solid interfaces. *Phys. Rev. B - Condens. Matter Mater. Phys.* **80**, 184301 (2009).
112. Bruce, P. G. & West, A. R. The A-C Conductivity of Polycrystalline LISICON, Li_{1+2x}Zn_{1-x}GeO₄, and a Model for Intergranular Constriction Resistances. *J. Electrochem. Soc.* **130**, 662–669 (1983).
113. Tiefenbach, A. & Hoffmann, B. Influence of a crack on the electrical impedance of polycrystalline ceramics. *J. Eur. Ceram. Soc.* **20**, 2079–2094 (2000).
114. Fleig, J. Influence of non-ideal microstructures on the analysis of grain boundary impedances. *Solid State Ionics* **131**, 117–127 (2000).
115. Heitjans, P. & Indris, S. Diffusion and ionic conduction in nanocrystalline ceramics. *J. Phys. Condens. Matter* **15**, R1257–R1289 (2003).

8 Appendix

8.1 Rietveld refinement

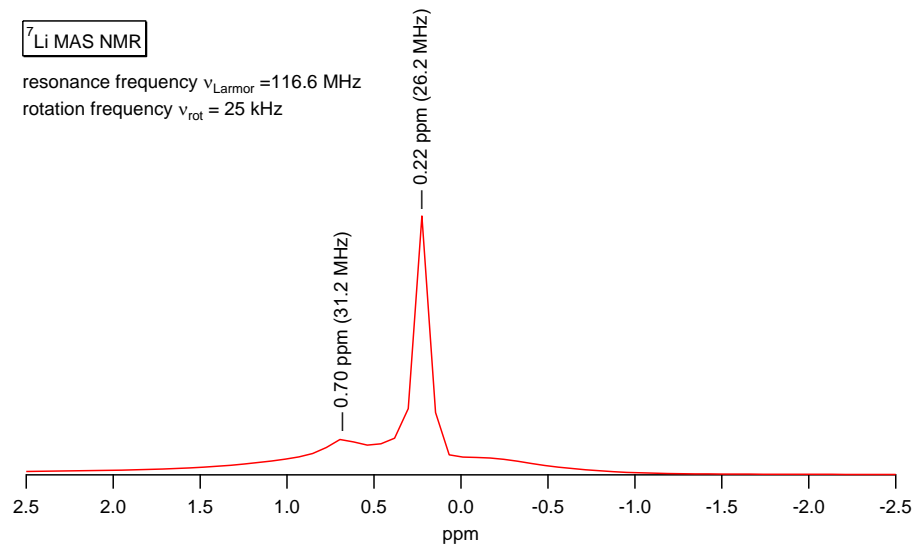


Rietveld refinement for LGPS – annealed 8 h @ 550 °C. GOF = 2.90.



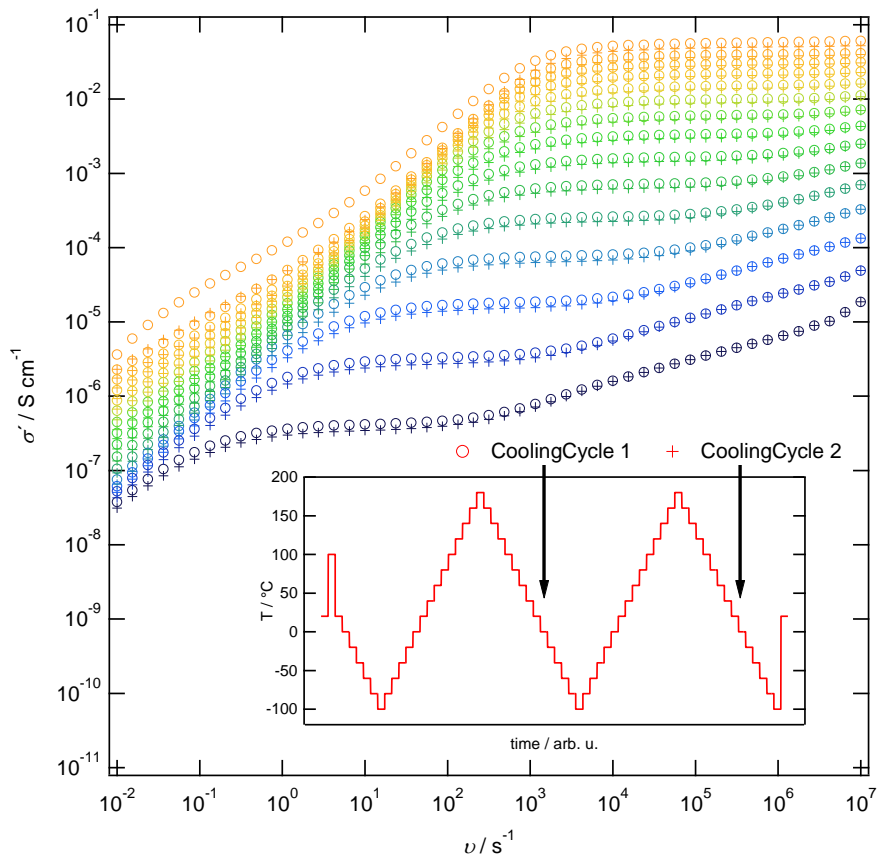
Rietveld refinement for LGPS – annealed 24 h @ 550 °C. GOF = 2.98.

8.2 ^7Li MAS NMR



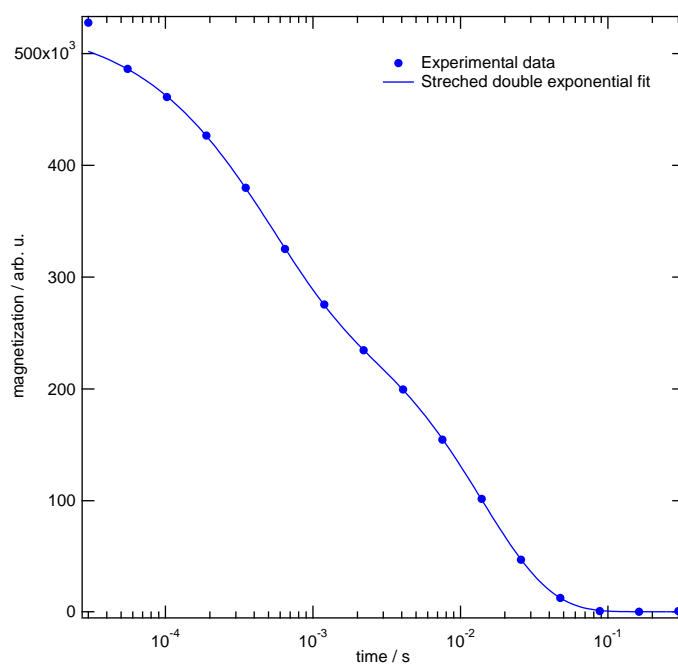
^7Li NMR spectrum on a (microcrystalline) LGPS sample annealed 8 h @ 550 °C.

8.3 Impedance and conductivity spectroscopy



Impedance measurement of a microcrystalline LGPS sample with two heating cycles.

8.4 ^7Li NMR Spin-lattice relaxation



Magnetization transient from $T_{1\rho}$ spin-lattice relaxometry of LGPS at -40°C . The double exponential relaxation is clearly visible.